RADC-TR-65-534, Vol. I
Final Report

INVESTIGATION OF PRECISION ANTENNA PATTERN RECORDING AND DISPLAY TECHNIQUES

PHASE II

J. Searcy Hollis
Samuel F. Hutchins
T. J. Lyon
et al

TECHNICAL REPORT NO. RADC-TR-65-534
February 1966

CLEARINGHOUSE
FOR FEDERAL SCIENTIFIC AND
TECHNICAL INFORMATION

Hardcopy	Microfiche		
$5.00	$1.00	157 pp	as

ARCHIVE COPY

Code 1

Distribution of this document is unlimited

Techniques Branch
Rome Air Development Center
Research and Technology Division
Air Force Systems Command
Griffiss Air Force Base, New York

INVESTIGATION OF PRECISION ANTENNA PATTERN RECORDING AND DISPLAY TECHNIQUES

PHASE II

J. Searcy Hollis
Samuel F. Hutchins
T. J. Lyon
et al

Distribution of this document is unlimited

FOREWORD

This final report (Volume I) was prepared by Scientific-Atlanta, Inc., Atlanta, Georgia 30324 under Contract AF30(602)-3425, Project No. 4506, Task No. 450604. J. Searcy Hollis, Samuel F. Hutchins, T. J. Lyon, Rezin E. Pidgeon, Jr. and C. S. Young were the authors. RADC Project Engineer was Martin Jaeger (EMATA).

This technical report has been reviewed and is approved.

Approved: Martin Jaeger
MARTIN JAEGER
Project Engineer
Antenna & Coherent Optical Section

Approved:
THOMAS S. BOND, JR.
Colonel, USAF
Chief, Surveillance and
Control Division

FOR THE COMMANDER:
IRVING J. GABELMAN
Chief, Advanced Studies Group

ABSTRACT

Volume I of the Final Report of theoretical work accomplished by Scientific-Atlanta, Inc., for Rome Air Development Center under Contract AF 30(602)-3425 is presented. The contract is for development of equipment to enhance the antenna measurement capability of ground-based antenna test ranges, and for continuation of theoretical studies initiated under Contract AF 30(602)-2737. The theoretical studies reported herein include an investigation of environmental effects and an analysis of parallax errors as related to high-accuracy antenna measurements; an investigation of antenna-positioning techniques and angle-measuring equipment; and a determination of optimum techniques for a high-speed precision recording system. Volume II will describe an amplitude- and frequency-stabilized signal source for the frequency range of 2 Gc to 4 Gc and a precision, high data rate receiver with logarithmic readout of data in digital and analog form.

ACKNOWLEDGMENTS

The contributions of Dr. Demetrius T. Paris of the School of Electrical Engineering and Mr. S. P. Lenoir, Jr., of the Rich Electronic Computer Center of the Georgia Institute of Technology in the study of parallax reported herein are gratefully acknowledged. Dr. Paris acted as consultant on the electromagnetic theory aspects of the problem and formulated the logic of the computer program. Mr. Lenoir was responsible for the detailed development of the computer program.

TABLE OF CONTENTS

TABLE OF CONTENTS - Continued

LIST OF ILLUSTRATIONS

LIST OF ILLUSTRATIONS - Continued

LIST OF ILLUSTRATIONS - Continued

LIST OF ILLUSTRATIONS - Continued

LIST OF TABLES

BLANK PAGE

1. INTRODUCTION

Contract AF30(602)-3425 encompasses work by Scientific-Atlanta, Inc., for Rome Air Development Center, continuing work accomplished under Contract AF30(602)-2737. The contract is for development of equipment to enhance the antenna measurement capability of ground-based antenna test ranges, and for continuation of theoretical studies initiated under the prior contract. Figure 1 is a graphical presentation in system-block-diagram form of the technical goals for the overall antenna pattern measurement system. Work accomplished under Contract AF30(602)-2737 was reported in the following reports.*

<u>Investigation of Precision Antenna Pattern Recording and Display Techniques</u>, First Quarterly Report, 1 April 1962 to 30 June 1962, RADC-TDR-62-365.	(QR 1-I)
<u>Investigation of Precision Antenna Pattern Recording and Display Techniques</u>, Second Quarterly Report, 1 July 1962 to 30 September 1962, RADC-TDR-62-560.	(QR 2-I)
<u>Investigation of Precision Antenna Pattern Recording and Display Techniques</u>, Third Quarterly Report, 1 October 1962 to 31 December 1962, RADC-TDR-63-53.	(QR 3-I)
<u>Investigation of Precision Antenna Pattern Recording and Display Techniques</u>, Final Report, 1 April 1962 to 29 March 1963, AD415-912.	(FR-I)

Work to date under Phase II has been reported in the following quarterly reports.

<u>Precision Antenna Pattern Recording Techniques, Phase II, First Quarterly Report, 1 June 1964 to 28 August 1964,</u> RADC-TDR-64-420.	(QR 1-II)
<u>Precision Antenna Pattern Recording Techniques, Phase II,</u> Second Quarterly Report, 31 August 1964 to 6 November 1964, RADC-TR-64-541.	(QR 2-II)
<u>Precision Antenna Pattern Recording Techniques, Phase II,</u> Third Quarterly Report, 9 November 1964 to 29 January 1965, RADC-TR-65-85.	(QR 3-II)

Equipment that is being developed under Phase II includes an amplitude- and frequency-stabilized signal source for the frequency range of 2 Gc to 4 Gc, and a precision, high data rate receiver with logarithmic readout of data in digital and analog form. The receiver incorporates new logarithmic conversion

---

*In this report the current contract (AF30(602)-3425) is referred to as Phase II; work under Contract AF30(602)-2737 is referred to as Phase I. For brevity references to the various reports will be made by the code given in parentheses.

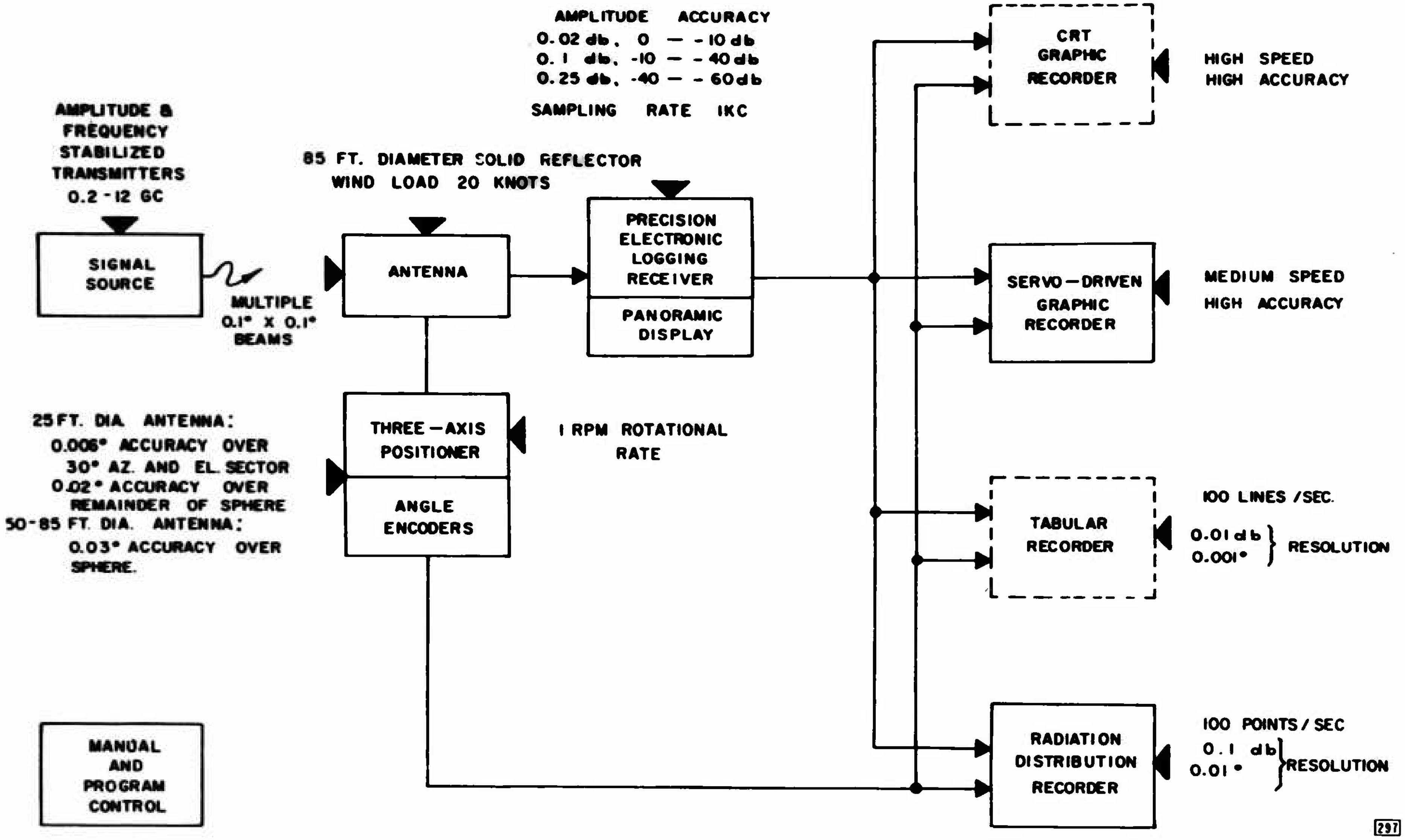

Figure 1

Technical Goals for Precision Antenna Pattern Measurement

NOTE: EQUIPMENT ENCLOSED IN DASHED LINES INCLUDED IN BLOCK DIAGRAM FOR FUTURE CAPABILITIES.

techniques, which were investigated for feasibility under Phase I. The receiver will be designed to cover the frequency range of 2 Gc to 4 Gc, but will be evaluated experimentally over the frequency range of 0.2 Gc to 12 Gc. A block diagram showing the equipment supplied under Phase II and incorporation of this equipment into the antenna measurements system is shown in Figure 2.

The scope of the theoretical studies includes an investigation of environmental effects and an analysis of parallax errors as related to high-accuracy antenna measurements; an investigation of antenna-positioning and angle-measuring equipment; and a determination of optimum techniques for a high-speed precision recording system.

This technical report describes work accomplished under the theoretical studies portion of Phase II. Work accomplished under the equipment development portion of the contract is described in a separate report.

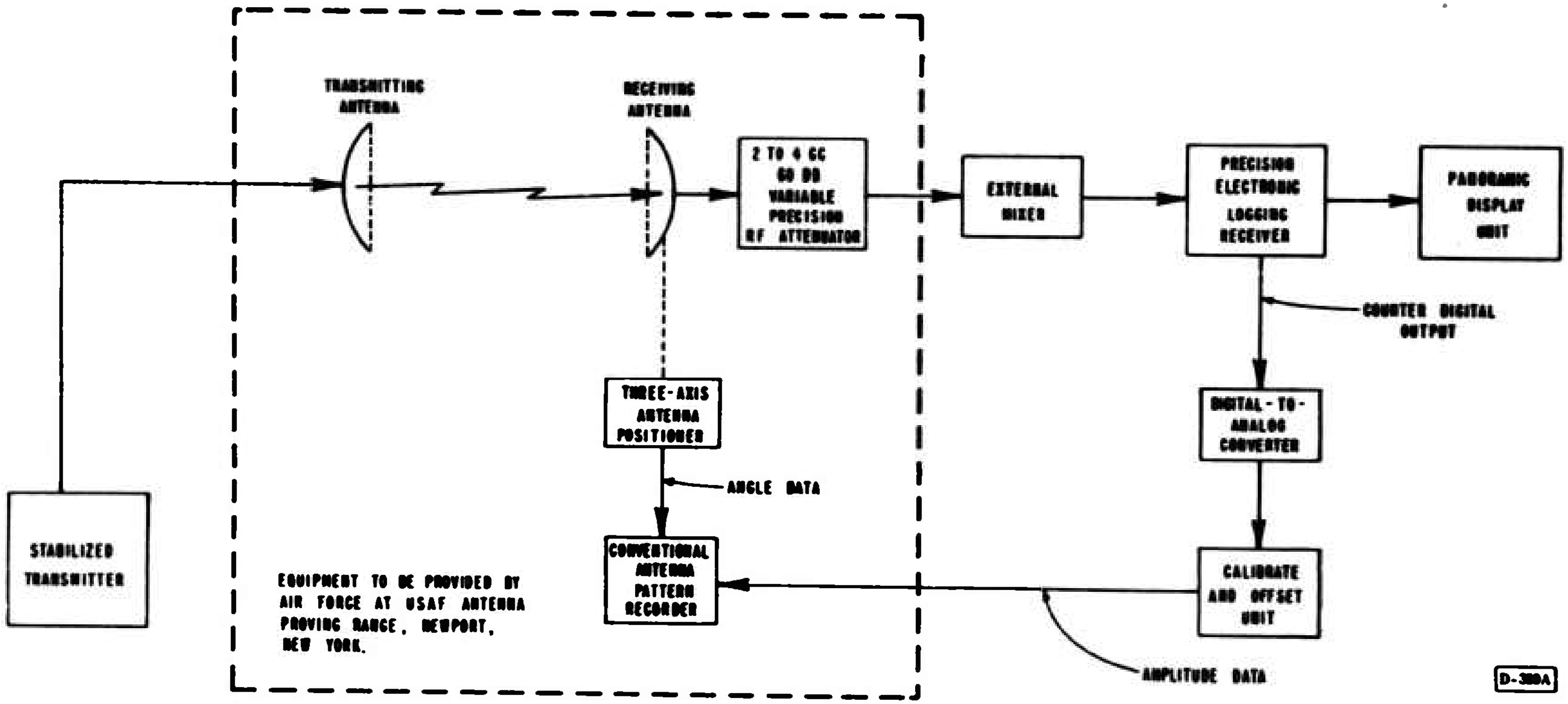

Figure 2

Block Diagram of Phase II of Antenna Pattern Measurement System

2. THREE-DIMENSIONAL ANTENNA PATTERN RECORDER AND DISPLAY SYSTEM

2.1 Introduction

The previous study contract investigated the manner in which antenna pattern data may be presented for observation and analysis. This was one of the most important aspects of the study primarily because of the large quantity of data required to adequately describe the performance of a precision antenna. One form of presentation investigated was the radiation distribution table, an example of which is shown in Figure 3. In this figure signal levels are shown numerically in decibels at angular increments of 0.5 degree in θ and ϕ. The contour effect seen on the graph was obtained by printing the even values of signal level and omitting the odd values. The signal-level resolution is 1 decibel in the example shown; a printed level of 4 decibels indicates a level between 3.5 and 4.5 decibels.

The table shown in Figure 3 was made by a Scientific-Atlanta Model 1801 Radiation Distribution Printer by scanning the antenna in the ϕ coordinate and stepping in θ after each ϕ cut. The graph was typed on frosted Mylar by means of a modified IBM electric typewriter. Signal levels were sensed by an encoder coupled to the servo-driven logarithmic potentiometer in an antenna pattern recorder.

The major advantage of the radiation distribution table is that it provides data on a single page for assessment of the general configuration of the radiation pattern of the antenna. From this type of presentation one can observe the shape of the main beam and side lobes, and read data such as side lobe levels or relative gain for a given θ, ϕ orientation.

An important feature of the radiation distribution table is the contour presentation afforded by printing only the even-valued decibel levels as illustrated in Figure 3. It is this contour presentation that enables one to visualize easily the overall pattern structure. The information content of the table is not materially affected by this presentation in regions of relatively slow signal-level change, since it is evident that the values of the omitted numbers lie between those of the adjacent printed numbers; however, in the regions of the nulls half of the information is lost. This loss of information can be overcome by recording

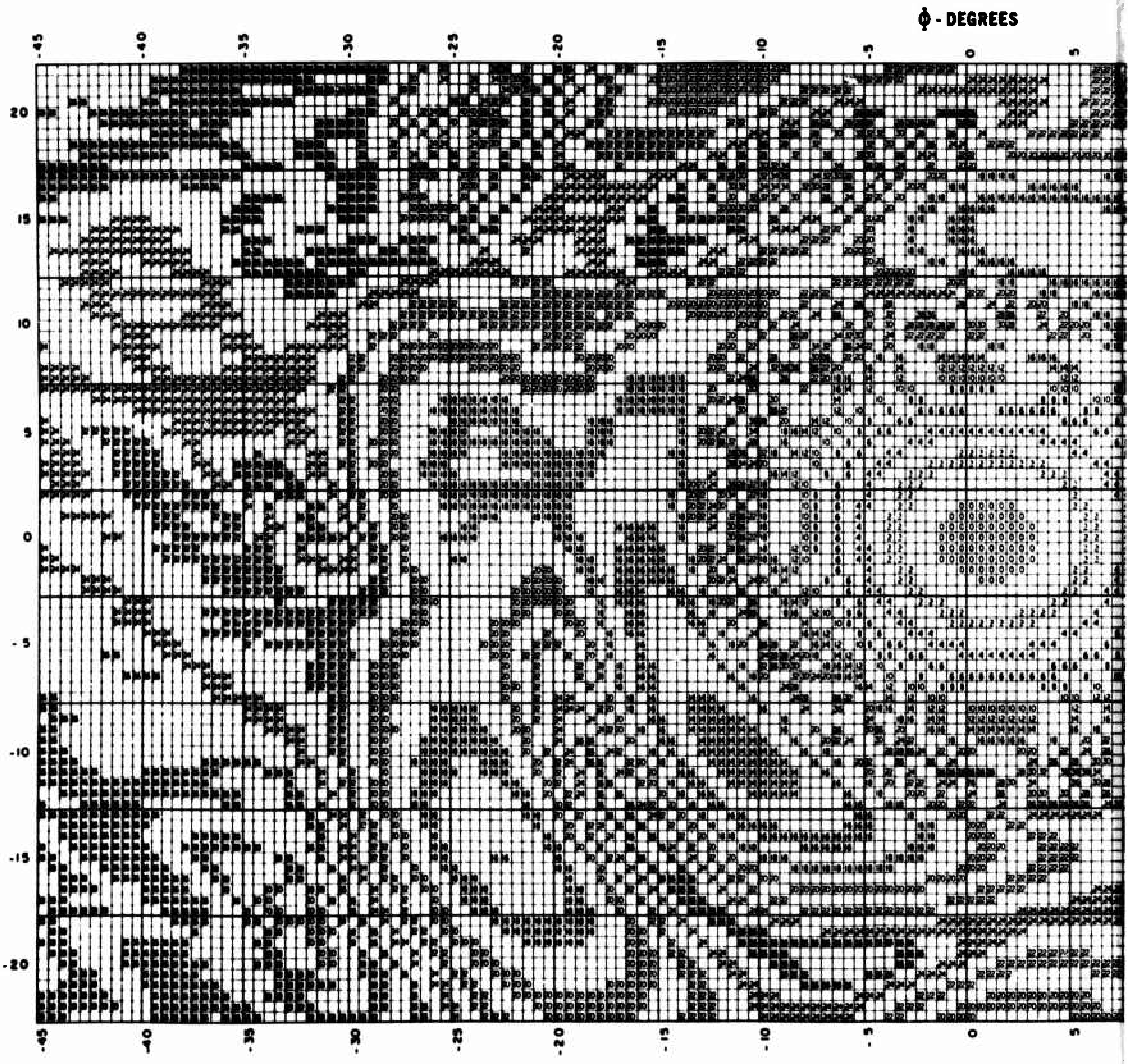

TEST PROGRAM OR VEHICLE: ________ INSTRUMENTATION SYSTEM: ________ PROJECT: 508

DATE: 12-10-62 PATTERN NO: 401 ORGANIZATION: SCIENTIFIC-ATLANTA INC. ENGRS: REP

ANTENNA TYPE: 6 FOOT PARAB FREQ. RANGE: ________ PATTERN MEASUREMENT FREQ. 1100MC

PREDOMINANT POLARIZATION: Eφ, LINEAR MODEL SCALE: ________ LOCATION OF POINT P'y (φ=0, θ=90°): ________

GAIN PLOT:

GAINS ARE

PHASE-ANGL

PHASE ANGL

A

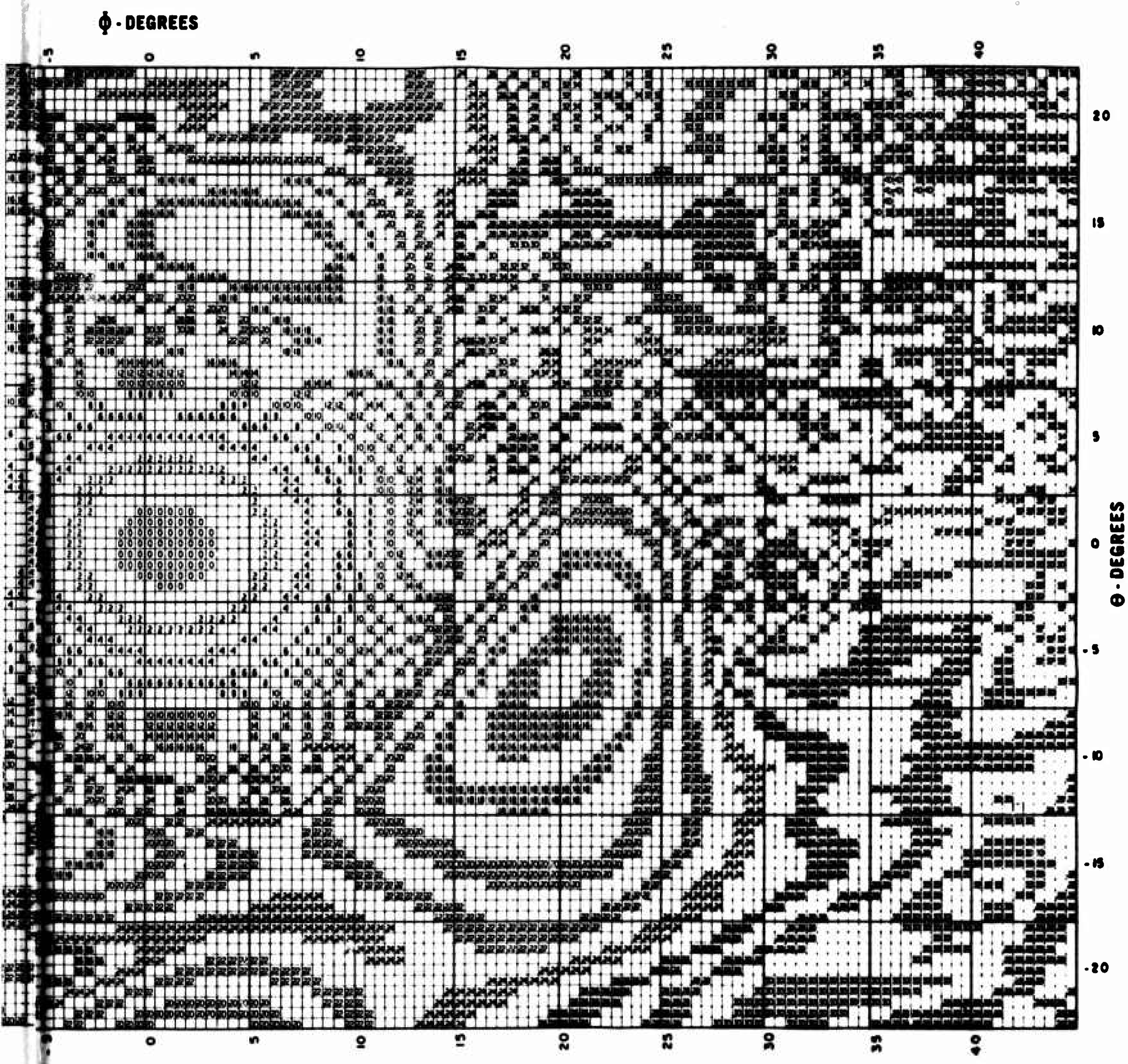

LOT: ☑ ________

IRE IN . REP ________

ANGLE . 1100MC ________

ANGLE ________

GAIN PLOT: ☑ POLARIZATION COMPONENT RECORDED: LINEAR ☒ Eϕ, ☐ Eθ; CIRCULAR ☐ RH, ☐ LH

GAINS ARE IN DECIBELS BELOW A REFERENCE LEVEL OF +☒ −☐ 24.5 DB RELATIVE TO AN ISOTROPIC ANTENNA OF LINEAR POLARIZATION

PHASE-ANGLE PLOT: ☐ PHASE ANGLE RECORDED: ☐δ, ☐δ'

PHASE ANGLES ARE RECORDED VALUES IN DEGREES MULTIPLIED BY 10.

D-853

Figure 3

Radiation Distribution Table

B

both even and odd signal levels, and emphasizing the contour levels by another means as described in Section 2.4.

It was recommended in the final report[1] of Phase I that a nearly ideal presentation from the viewpoint of ease of manual data analysis only, and ignoring other factors, would be in the form of a booklet of signal level versus ϕ cuts and θ cuts with a radiation distribution table for the angular region included by the θ and ϕ cuts as a preface and index to the data booklet. The overall picture of the radiation pattern would be provided by the radiation distribution table; detailed data would be obtained from individual graphs.

It was pointed out that such a complete and detailed presentation would not normally be warranted, but that data would be recorded in greater detail than is presently done if the data could be recorded conveniently and at high speed. Two approaches were recommended for recording and presenting pattern data. These would employ

(a) A high-speed recording system with capability of providing a complete booklet of patterns prefaced by a radiation distribution table, but with system flexibility for providing patterns for as rapid and cursory requirements as are likely to be required. This system would require development of a high-speed graphic recorder and radiation distribution recorder. It was suggested that the most practical technique for recording antenna patterns at high speeds was one which displayed the pattern on the face of a cathode-ray tube and photographed the pattern for a permanent record. The recordings could be stored on 35 mm film and viewed in a microfilm reader for fast retrieval of selected data. Alternatively, antenna patterns could be recorded on magnetic tape and selected cuts displayed on a digitally controlled X-Y recorder operating from the tape file. The magnetic tape system would offer greater flexibility in reproducing the antenna patterns and would be useful for entering data into a computer for further data analysis.

(b) A high-speed radiation distribution recorder in conjunction with a slower speed, high-accuracy graphic recorder. The overall

---

[1] FR-I, page 33.

> radiation pattern would be described by the radiation distribution table. Selected cuts, such as principal-plane cuts and others of specific interest, would be recorded by the graphic recorder. The radiation distribution table would be used to indicate what cuts are necessary for additional analysis of the data. Since this method requires considerably fewer graphic recordings than contained in the booklet of patterns previously described, a slower-speed graphic recorder would suffice. A recorder with a writing speed comparable to the slewing speeds of conventional antenna pattern recorders, but with better static and dynamic accuracy, would offer a reasonable compromise.

Since each of the above presentation methods requires a radiation distribution recorder with speed, accuracy, and flexibility capabilities exceeding those of existing equipment, an investigation was made of possible recording techniques. Phase II of the program was undertaken to prove the feasibility of the recording method proposed in Phase I and to define in greater detail an optimum recording system. Results of the feasibility investigation are given in Section 2.3, and details of the proposed system are given in Section 2.4. Since a detailed investigation of high-speed pattern recorders or magnetic tape recording systems was beyond the scope of the study program of Phase II, a further study of these recording methods should be undertaken in order that equipment may be developed to meet the goals of the RADC program.

2.2 Objectives of High-Speed Radiation Distribution Recorder

The major factors to be considered in defining the objectives of the high-speed radiation distribution recorder are

(a) The number of data points per ϕ cut,
(b) The number of ϕ cuts per table,
(c) The amplitude resolution,
(d) The method of emphasizing contours, and
(e) The recording speed.

The above factors must be considered in light of the application of the radiation distribution table and practical limitations of the recording system. In addition, the format for the radiation distribution table must enable the data to be easily read and present a clean appearance.

In considering the number of data points required for each ϕ cut, it is helpful to observe the appearance of the radiation distribution table shown in Figure 3. It can be seen that in cases where the slope of the pattern is equal to or less than 1 decibel per sample increment, the lobe structure of the pattern can be easily recognized. The sampling increment is, therefore, related to the antenna beamwidth and the depth of the sidelobes for which contour information should be preserved. To recognize the overall pattern structure there should be a minimum of approximately 12 and preferably 18 to 24 data points per beamwidth for each angular coordinate.

In Figure 3 the 3-db beamwidth is approximately 11.5 degrees and the sampling increment is 0.5 degree. There are approximately 23 data points per beamwidth. In this case, the number of data points per ϕ cut (180) is sufficient to display the main diffraction region on a single radiation distribution table. However, as the amplitude resolution of the table is increased the angular resolution should also increase, and the number of data points per ϕ cut should increase proportionately to maintain the same ϕ sector coverage. Practical limitations, however, determine an upper limit on the number of data points that can be recorded on a single line. Some of the factors to be considered in establishing the maximum number of data points are:

(a) Resolution capabilities of the recording system,

(b) Reproduction methods and capabilities of commercial duplicating equipment, and

(c) Readability of a very large table.

Consideration of the maximum resolution achievable in a practical recording system, based on results of the experimental recorder described in Section 2.4 and further studies, indicate a factor of two increase in the number of data points for each angular coordinate over that of Figure 3 is reasonable. Furthermore, since it is desirable to make 360-degree ϕ cuts while sampling in a convenient increment such as 0.2, 0.5, 1.0, or 2.0 degrees, the number of data points per line should be 180, 360, 720, or 1800 in correspondence with the sampling increment. Of this selection, 360 data points is the maximum number of points that would provide convenient readability and reproducibility of an entire radiation distribution table, and is in agreement with the resolution achievable in a practical recording system. Therefore, the radiation distribution recorder should be designed to record 360 data points per ϕ cut, and should be capable of recording fewer points if desired.

The number of ϕ cuts in the radiation distribution table can be related to the number of data points per ϕ cut. Since it is required that the system record 360° ϕ cuts in 1-degree sampling increments, complete spherical coverage can be achieved by 180 θ increments with equal angular resolution in both coordinates. Therefore, the system should be capable of recording twice as many data points for both θ and ϕ coordinates as shown in Figure 3, giving a total of four times as many data points for the entire radiation distribution table.

It should be noted that a large high-resolution table could be obtained by combining several small radiation distribution tables covering adjacent sectors. Two or more tables of small sectors could be recorded and then placed side by side to display a large sector. However, producing the desired number of data points on a single table reduces the time required to obtain the data and simplifies operation of the system.

If the radiation distribution table is to be used to obtain only an overall picture of the radiation pattern, signal level resolution of 1 decibel is generally sufficient. For some applications, such as close examination of the main lobe of a narrow-beam antenna, greater resolution and accuracy may be desirable. Various methods to display 0.1 db resolution have been considered. These methods included (1) recording each data point as a 3-digit number (or 2-digit number for the range 0 to 9.9 decibels) with the tenth-decibel figure raised slightly to distinguish it from the others, and (2) recording each sample as a 2-digit number (or 1-digit number for the range 0 to 9.9 decibels) and indicating the value to a tenth of a decibel by a binary-coded dot pattern.[2] The difficulty with each of these methods is that they require greater resolution of the display than required for 2-digit numbers only and the resulting table is cluttered with detail not normally required.

One of the major problems to be encountered in developing the recording system is that of maintaining sharp character detail so that the table will be as easy to read as possible. Since it is felt that it is more important to record the maximum

---

[2] An example of these methods is given in Figures 24 and 25 of FR-I.

practical number of data points than to record only approximately half that number with tenth-decibel resolution, the format shown in Figure 4(a) is recommended. Data are recorded as shown as 2-digit numbers. Resolution' of one-tenth decibel is provided for the range 0 to 9.9 decibels by the 2-digit number. The right-hand numeral, which is in tenths of a decibel, is shown in a superscript position to differentiate between the 2-digit numbers for 10 decibels and greater.

Additional accuracy may be achieved for values greater than 10 decibels through contour emphasis. Contours may be identified by circumscribing a box around values within the selected contour increment as illustrated in Figure 4(b). The contour increment should be selectable in tenths of a decibel about each integral value. That is, it should be possible to record the contour identification symbol at integral values of the input data, or when the input data are within either ±0.1, ±0.2, ±0.3, ±0.4, or ±0.5 decibel of an integral value. Furthermore, the separation between contour centers should be selectable in 1-, 2-, 3-, 6-, or 10-db increments. Thus, the display can be read directly in tenths of a decibel for the range 0 to 9.9 decibels where accuracy and resolution are most important in antenna measurements, and will provide for tenth-decibel accuracy for the remainder of the range through contour emphasis, while providing the greatest readability of data and with a reasonable compromise on recorder complexity. For the intended use of the radiation distribution table, the format shown in Figure 4 is an optimum compromise between the desired number of data points, resolution of each data point, ease of reading and interpreting the table, and practical limitations on the recording density and system complexity.

Provisions must be included for recording major coordinate lines and for recording the major coordinate values in the margin surrounding the table. The format for this display is shown in Figure 4(c). It is not practical to employ an overlay for the coordinate lines because of the registration problem.

The recording speed should be as high as is reasonable in order to minimize the recording time. The maximum recording speed will, of course, depend on the type recording system employed. A reasonable data rate is 100 data points per second for a recorder similar to the experimental model discussed in Section 2.3 and the proposed recorder discussed in Section 2.4. The minimum recording time for a single cut would be 3.6 seconds and, if 0.4 second is allowed for

(a) Example of numerical display. Superscript numerals in display at left are in tenths of a decibel. Display at right is read directly in decibels.

(b) Method of emphasizing contours. The box circumscribed around a number indicates that sample was within the selected contour increment.

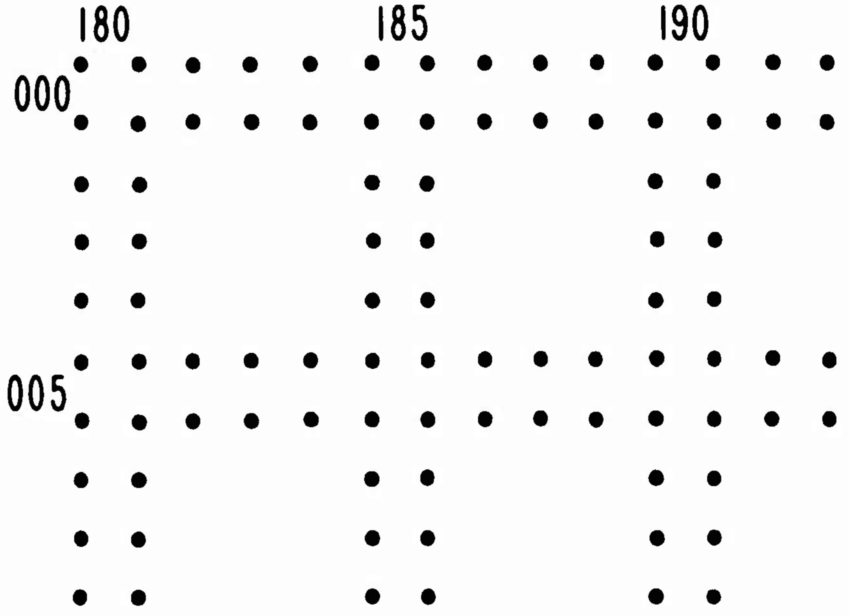

(c) Method of identification of major coordinates

Figure 4

Proposed Radiation Distribution Table Format

D-855

the recorder to advance a single line, the total recording time for a radiation distribution table of 180 θ increments would be 12 minutes.

2.3 Experimental Measurements

During the previous study contract an investigation was made of recording techniques[3] suitable for producing a radiation distribution table, and the method illustrated in Figure 5 was proposed for evaluation. In this system the table is recorded at a reduced size on fine-grain silver-halide film. Because it is impractical to display an entire radiation distribution table on the face of a cathode-ray tube (CRT), the film is positioned to image each group of characters to the correct θ, ϕ location on the film. The characters are displayed at a fixed location on the face of the CRT. The film is mounted on a digitally controlled film transport as illustrated. Numbers are written across the film by alternatively projecting the 2-digit numbers, coordinate lines, and contour-identification symbols onto the film and stepping the film in the X (ϕ coordinate) direction. The film is advanced one increment in the X direction by a stepping motor for each angular increment of rotation of the antenna in ϕ. Upon completion of each ϕ scan the film is stepped one increment in the Y (θ coordinate) direction by a stepping motor.

After the film has been exposed to the entire radiation distribution table it is developed and observed in a microfilm viewer. Alternatively, an enlarged print can be made from the film transparancy with commercially available field equipment.

The above method of producing a radiation distribution table results in a relatively simple recording mechanism. The numbers of the CRT are magnified in size over the image on the film. This magnification allows the characters to be formed on the screen of the CRT large enough so that the character quality is not degraded by resolution limitations or halation of the CRT. Other characteristics of the system, such as film resolution, film sensitivity, and recording rates are compatible with the objectives outlined in Section 2.2.

During the current contract a one-axis model of the recorder was constructed and tested to prove the feasibility of the recording method illustrated in Figure 5

---

[3] FR-I, pp. 100-113.

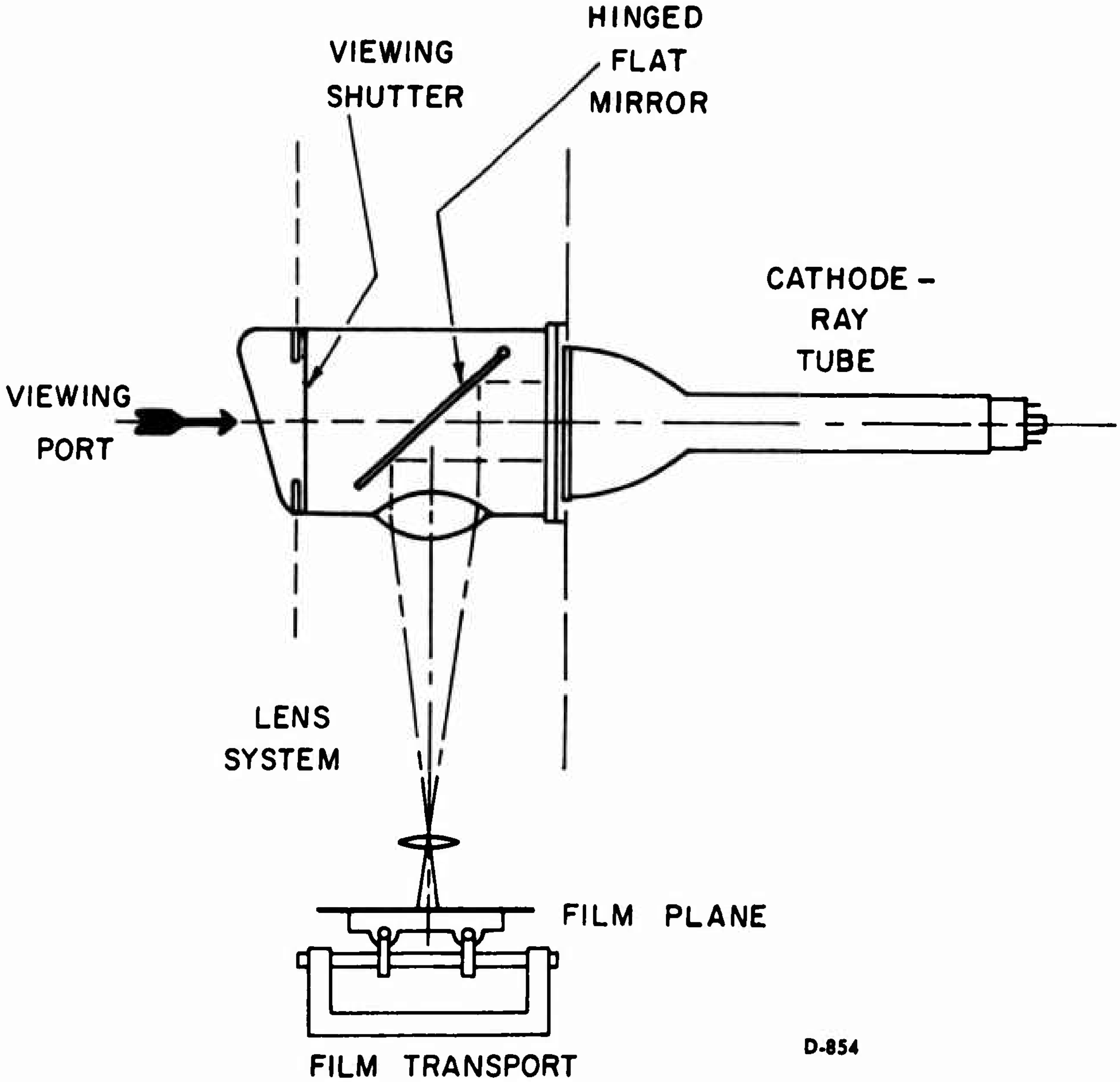

Figure 5

Photographic Method of Recording Radiation Distribution Table Proposed in Phase I and for investigating associated mechanical, optical, and photographic problems. Results of these tests were reported in the third quarterly report and are given in paragraph 2.3.2 along with additional data. For these experiments Polaroid type 55 Positive/Negative film was used for convenience; suitable rapid-processing equipment for other films was not on hand.

The experimental recorder was designed specifically for making measurements to prove the feasibility of the proposed recording system. A more sophisticated design based on results of the experimental program would be incorporated in a prototype model and would result in improved dynamic performance.

The purpose of the experimental tests was to

(a) Investigate dynamic characteristics of the carriage and drive mechanism,

(b) Determine practical stepping rates,

(c) Investigate film characteristics, and

(d) Investigate associated optical and mechanical problems.

2.3.1 Description of Experiment

The configuration of the experimental set-up is shown in Figure 6. Straight traces and 2-digit numbers (consisting of the digits "0" and "1") were written on the screen of the CRT by auxiliary equipment synchronized with the carriage stepping rate. The traces and characters were focused on the film surface by a lens mounted in the camera box. The film carriage was positioned by a ball-screw drive connected to a Sigma stepping motor. The film was held flat against its mount by a vacuum hold-down system.

The film carriage mechanism consisted of a modified Polaroid 4x5 film holder (No. 500) with attached guide members which rode in a vee-block. The film carriage was thus restricted to a single degree of freedom. The carriage drive motor, which was rigidly mounted to one end of the light-tight box, had 20 incremental static positions per revolution. A 0.2222-inch pitch ball screw was attached to the motor, and the ball-bearing nut held fixed in the base of the carriage. Each 18-degree step of the drive motor advanced the film carriage approximately 0.011 inch. The incremental travel of 0.011 inch is somewhat smaller than required to record 360 data points on the 5-inch wide film, but

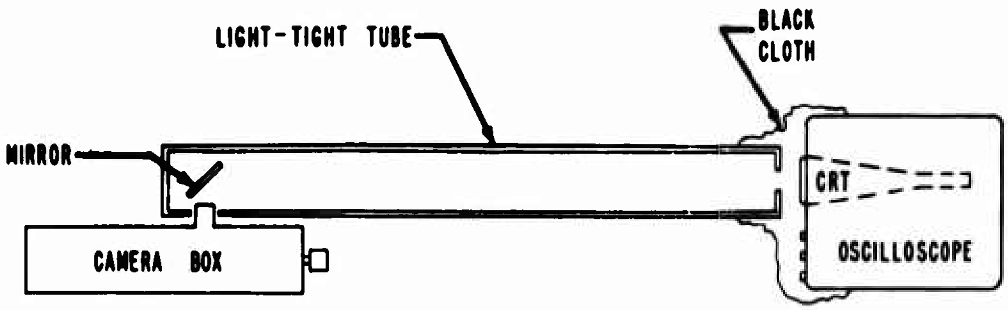

(a) Test Configuration

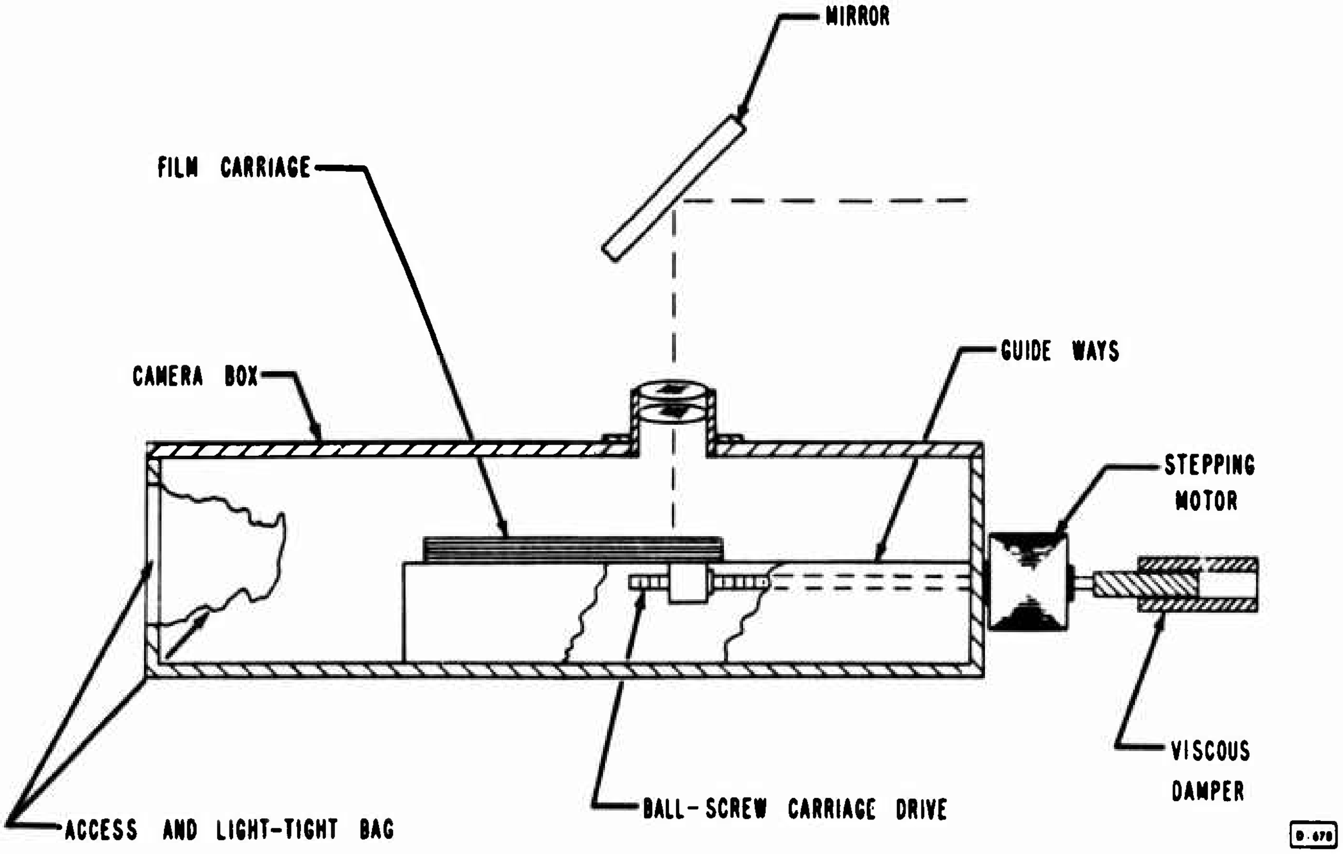

(b) Film Transport Mechanism

Figure 6
Experimental Recording System

was selected based on a standard pitch for the ball screw. The stepping motor was controlled by a flip-flop driver with adjustable pulse width. Satisfactory operation was achieved with pulse widths of 7 to 15 milliseconds. A viscous damper was fabricated to control the overshoot of the carriage. The device consisted of a two-inch long cylinder that rotated in a tube with approximately 0.0005 inch clearance for an oil film. The amount of damping was adjusted by changing the oil viscosity and by varying the depth of insertion of the cylinder in the tube.

A Tektronix Model 545A laboratory oscilloscope with a P-11 phosphor CRT was employed for the experiments. The digits "0" and "1" were generated by an external circuit and were synchronized with the leading edge of the pulse applied to the stepping motor. The display size was adjusted so that the two digits were within a 0.5-inch square on the CRT screen. The brightness of the display was maintained low enough to prevent blooming of the characters.

Polaroid type 55 Positive/Negative film was used for all tests. This film produces a positive print and a fine-grain negative. The resolving power of the negative is rated at 165 lines per millimeter when the negative is properly developed and rinsed. The film, which comes in single-exposure packets, was inserted in the modified film holder and developed outside the camera box.

The traces and characters written on the CRT screen were focused on the film surface with a 58-mm focal-length Primoplan camera lens. All of the tests were performed with a lens opening of f/2.8. The image-to-object magnification factor for the experimental set-up was 1/45 in order to reduce the 0.5-inch display cell to the 0.011-inch carriage stepping increment. For a focal length of 58 mm, the image and object distances are 59.3 mm and 2670 mm (8.8 feet), respectively, for the given magnification ratio. The relatively long object distance of 8.8 feet was accommodated by a plywood light-tight tube, 8.0 feet long. In a finished model a shorter object distance can readily be obtained by the use of a shorter focal-length lens system without degradation of the optical characteristics. It is suggested in Section 2.4 that a lens with a focal length of about 6 mm and an effective aperture of 3 mm could be used.

2.3.2 Test Results

Figure 7 summarizes the series of tests that were performed to evaluate the

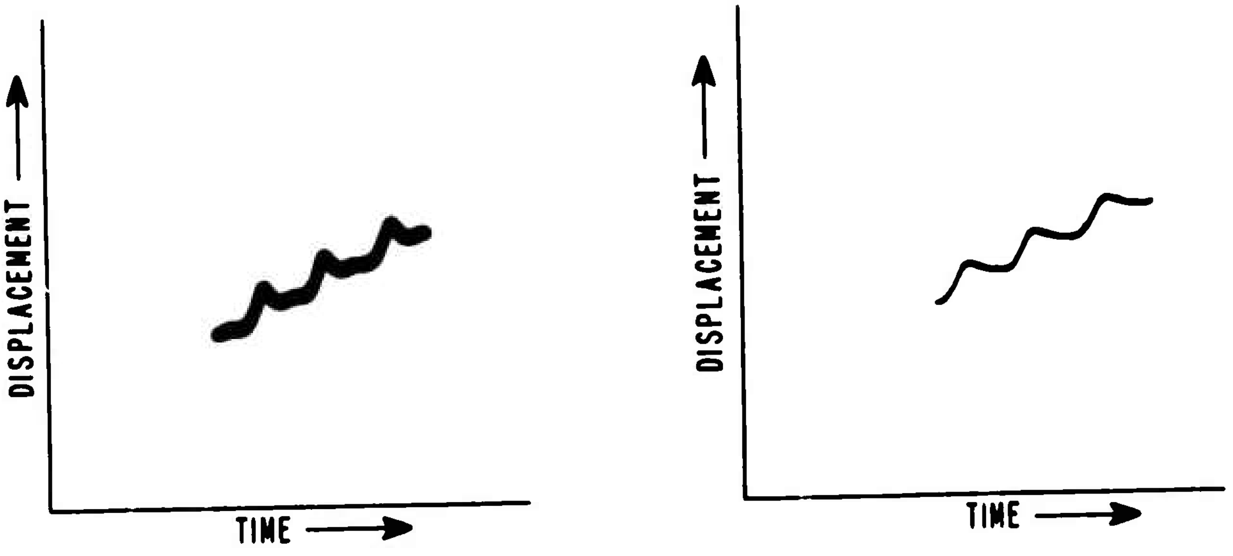

(a) 50 Steps per Second
No Damping

(b) 40 Steps per Second
Viscous Damping

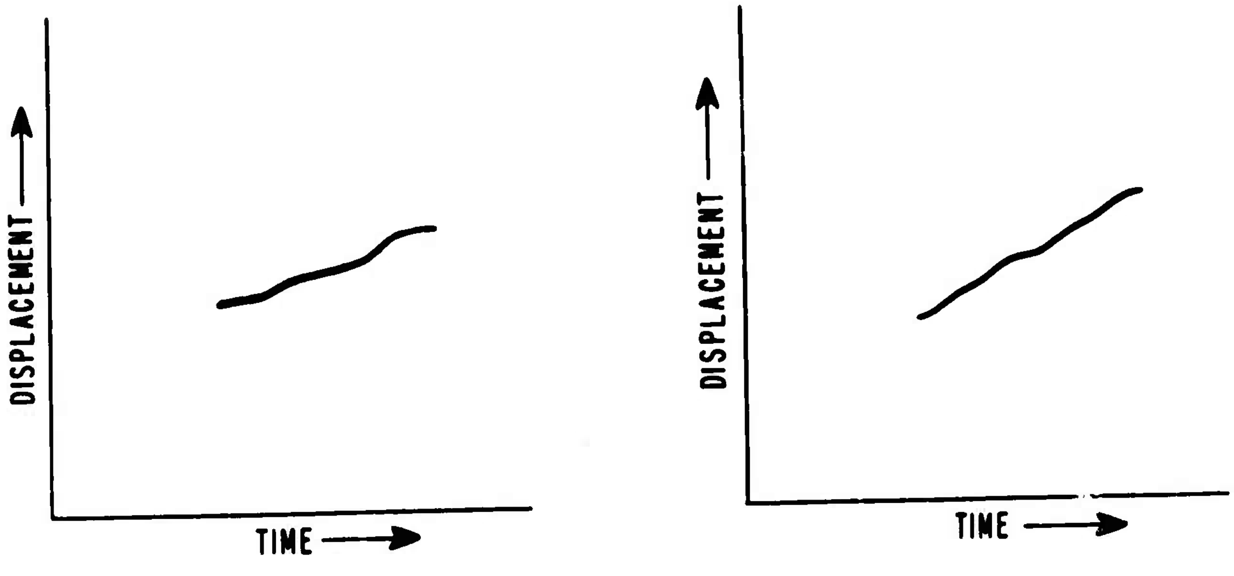

(c) 80 Steps per Second
Viscous Damping

(d) 100 Steps per Second
Viscous Damping

D-718

Figure 7
Step Response of Film Carriage

dynamic velocity characteristics of the incremental drive system. This figure is a record of the step response of the carriage as a function of the amount of viscous damping. These photographs were obtained by opening the camera shutter while the CRT spot was being deflected at a linear rate to provide a time base. The image of the CRT trace was focused onto the film surface perpendicular to the direction of carriage motion.

Figure 7-A is a record of the carriage dynamic response for the case in which damping was supplied by the greased guide ways only. It is clearly evident from the large overshoot that occurs at each step that the system is underdamped. The addition of the variable viscous damper was necessary to reduce the overshoot to an acceptable level as illustrated in Figure 7-B.

As the stepping rate of the film carriage was increased, the dwell time between each step became shorter. At 80 steps per second (Figure 7-C) the carriage velocity approached zero between drive pulses, but at 100 steps per second the carriage did not come to rest. The nearly straight sloping line of Figure 7-D indicates that the carriage velocity was nearly constant.

Figure 8 is a reproduction of the test results in which the number "10" was formed on the CRT in synchronism with the drive pulses to the stepping motor. Because the character-generator circuit did not have the capability of changing numerals during a single run, the CRT was blanked during alternate steps of the motor to ensure that there was no carry-over of the image between frames.

The numbers of Figure 8-A were recorded at a step rate of 40 per second. There was no blurring of the characters from motion of the carriage, because at this stepping rate the carriage is essentially at rest during exposure. The writing rate on the CRT was adjusted to form the two characters in 1.0 millisecond.

The numbers in Figure 8-B were obtained with a writing time of 125 microseconds per character. The rate of 130 steps per second was too fast to permit the film carriage to come to rest between steps. However, at a rate of 130 steps per second, the carriage moved only 0.00018 inch in 125 microseconds. This amount of movement is insignificant when one considers that the line width of a character on the film is approximately 0.002 inch. The uniformity of the spacing of the 2-digit groups confirmed that the carriage velocity is nearly

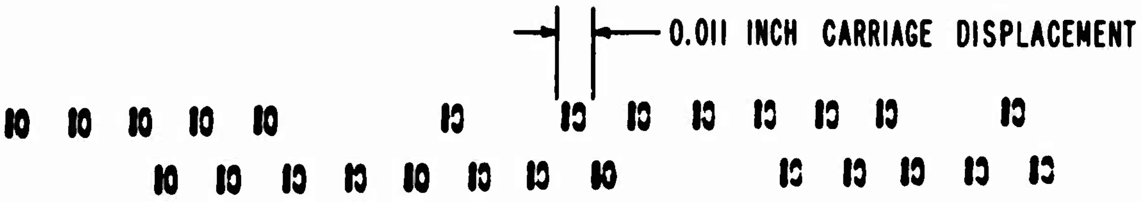

(a) 40 Steps per Second Carriage Velocity

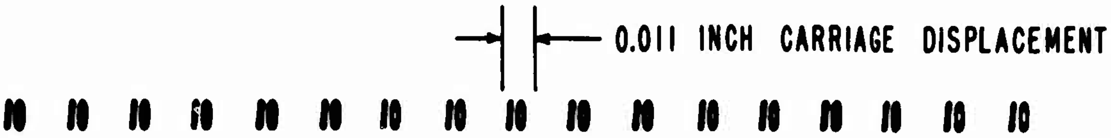

(b) 130 Steps per Second Carriage Velocity

D-719

Figure 8.

Reproduction of Photographs Obtained with Experimental Recording System constant. The results of this test show that recording rates in excess of 100 samples per second are practicable.

An examination of the negatives showed that the minimum line width was about 0.001 inch and was usually between 0.0015 to 0.002 inch. The minimum line width was not limited by grain size of the negative, but apparently the film was overexposed to obtain high contrast. Efforts to obtain sharper images at reduced contrast usually resulted in unacceptable contrast of the characters. This problem was not pursued further because of a decision to use a different type of film and film processing as described in Section 2.4.

2.4 Proposed Recording System

2.4.1 General Description

Experience gained with the breadboard model of the radiation distribution recorder described in Section 2.3 verifies that the basic approach is feasible and that recording rates in excess of 100 data points per second are practicable. The major problem from the standpoint of convenience of operation in the field was with the Polaroid film. The Polaroid type 55 Positive/Negative film is developed in 20 seconds. However, the negative must be properly rinsed and dried before it can be used. For best results, the negative should be cleaned in a sodium sulfite solution, washed in an acid bath containing acetic acid and potassium alum, rinsed in running water, and then dried. This not only delays the operator from viewing the radiation distribution table, since the negative must be put into a projector for magnification to a readable size, but requires special processing facilities and handling of the film.

Alternate approaches using other films and papers were considered. The best approach at this time appears to be one that uses conventional film in roll form and a rapid processor to develop and dry the film. This method is particularly attractive because the system can be made automatic to avoid handling the film, and suitable high quality rapid processors are available. Processors similar to that required for the proposed system have been developed for military applications such as processing of airborne radar films and aerial camera photography. A brief description of the rapid processor is given in paragraph 2.4.5.

The proposed recorder is basically similar to that described earlier and illustrated in Figure 5 except that in the new method strip film is used and the film is driven in a rotary motion instead of an X-Y motion. In addition to providing greater automation, this approach has the advantage that critical mechanical tolerances are easier to achieve with rotary motion than with the X-Y motion. The dynamic problems of the incremental drive system appear to be comparable in either case.

The recording method proposed is shown symbolically in Figure 9. This figure is intended to illustrate the principle of operation of the recorder, and is not a true representation of the mechanical details necessary for the system. The detailed design of the recording mechanism will be influenced largely by the problems associated with maintaining sharp focus and good registration over the entire film area.

The use of continuous strip film and the general configuration of the recording mechanism is oriented toward high speed operation and operator convenience. As illustrated in Figure 9, the film is drawn from a bulk supply reel and remains threaded through the system as successive tables are recorded. At the end of each recording the film is automatically advanced to feed the exposed film through the rapid processor and into the hands of the operator. Marks exposed at the edge of the film are sensed as it merges from the processor to automatically shear the film. While the film is being advanced, fresh film is brought to the recorder section for a new recording. Manual threading of the film through the system is required only after the film supply reel has been exhausted.

The film is driven by the ϕ-axis drive system while data are being recorded. The film loops shown in Figure 9 permit the ϕ-axis drive to advance and return the film while it remains stationary on the supply reel and in the processor. After the programmed number of the ϕ cuts have been made to expose the entire radiation distribution table, the film is automatically advanced. The film is drawn from the supply spool and fed through the recording section and processor at a constant rate. After the exposed film has been processed and ejected from the recorder the system is ready to record a new radiation distribution table.

2.4.2 Radiation Distribution Table Configuration

The film width selected for the radiation distribution table is 105 mm. This size appears to be the best compromise in that (1) it is large enough to enable an

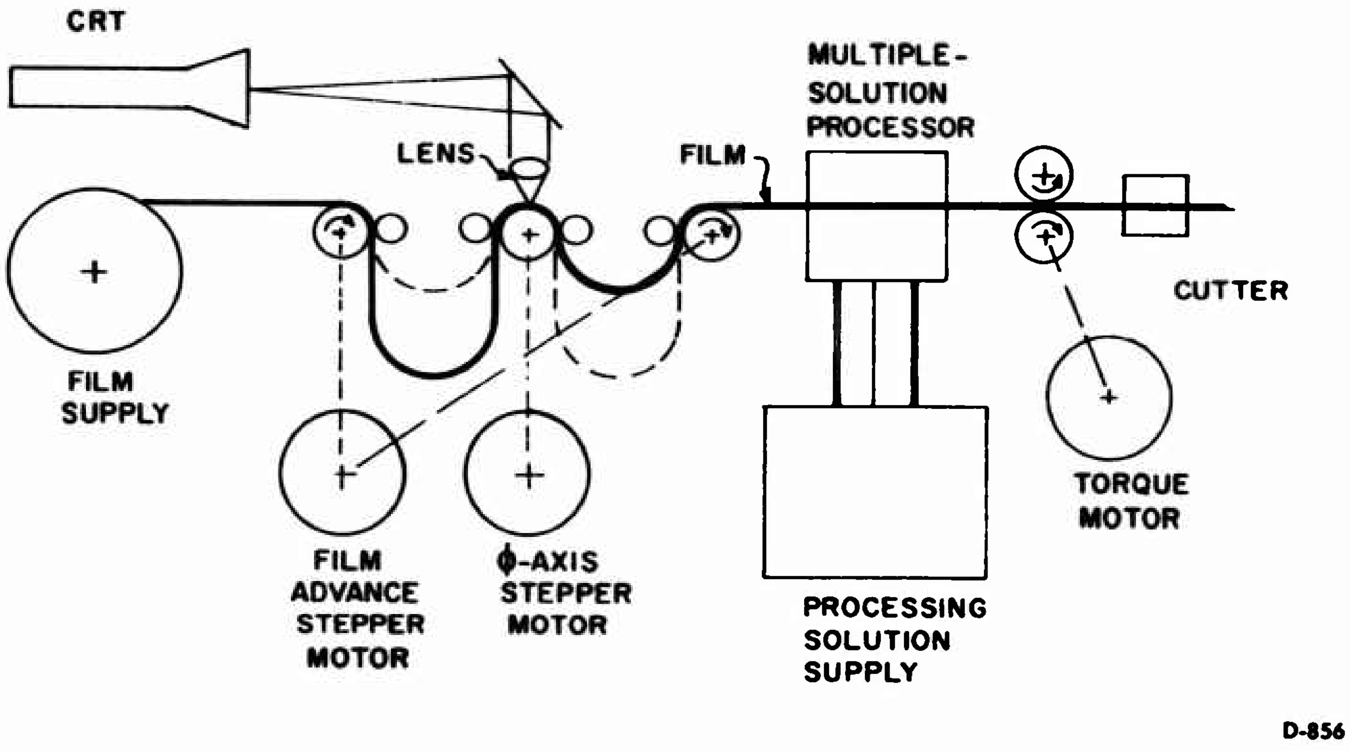

Figure 9

Symbolic Representation of Recorder Mechanism entire table to be recorded on a single film and maintain crisp images without excessive resolution problems, (2) it is large enough to avoid highly critical tolerances in the mechanical drive system, (3) it is small enough to enable the high data rates to be achieved with a relatively simple film drive system, (4) rapid film processors and viewing equipment are available for this size, and (5) it is a convenient size for storage of files of data.

Some of the standards adopted by the National Microfilm Association and federal government agencies for 105 mm microfiche film cards[4] can be retained for this application. The microfiche format used for document storage is shown in Figure 10. Microfiche records are used for storage of drawings, reports, and libraries of information. Sixty pages of data are normally recorded on a single microfiche as indicated by the page numbers shown in Figure 10.

A layout of the radiation distribution table is given in Figure 11. The title block area is reserved for attaching an identification strip to the film for information such as the antenna tested, antenna pattern number, date, and other key data. The information may be written large enough to be readable without magnification and would be used to locate film cards within the film card file. The title may be prepared by typing or writing on a transparent strip of material and placing this strip in the title-block area prior to making a contact print. Strips of acetate with an adhesive at each end are available for this purpose.

The radiation distribution table requires an area of approximately 76 by 137 mm, or 3.0 by 5.4 inches. The cell size for each data point, which is determined by the requirement to display data in one-degree increments over the range of 360 degrees, is 0.015 inch square. A total of 180 θ increments is required for complete spherical coverage when sampling in one-degree increments. However, space is available for recording up to 200 ϕ cuts when sampling in smaller increments of θ.

2.4.3 Recording Mechanism

The simplified diagram of Figure 12 shows the essential elements of the proposed recording mechanism. The ϕ and θ motions are accomplished by a drum and carriage mechanism. The film is supported and moved by the drum while the lens is supported by a carriage that moves parallel to the axis of the drum.

---

[4] National Micro News, No. 66, October 1963, pp. 42-76.

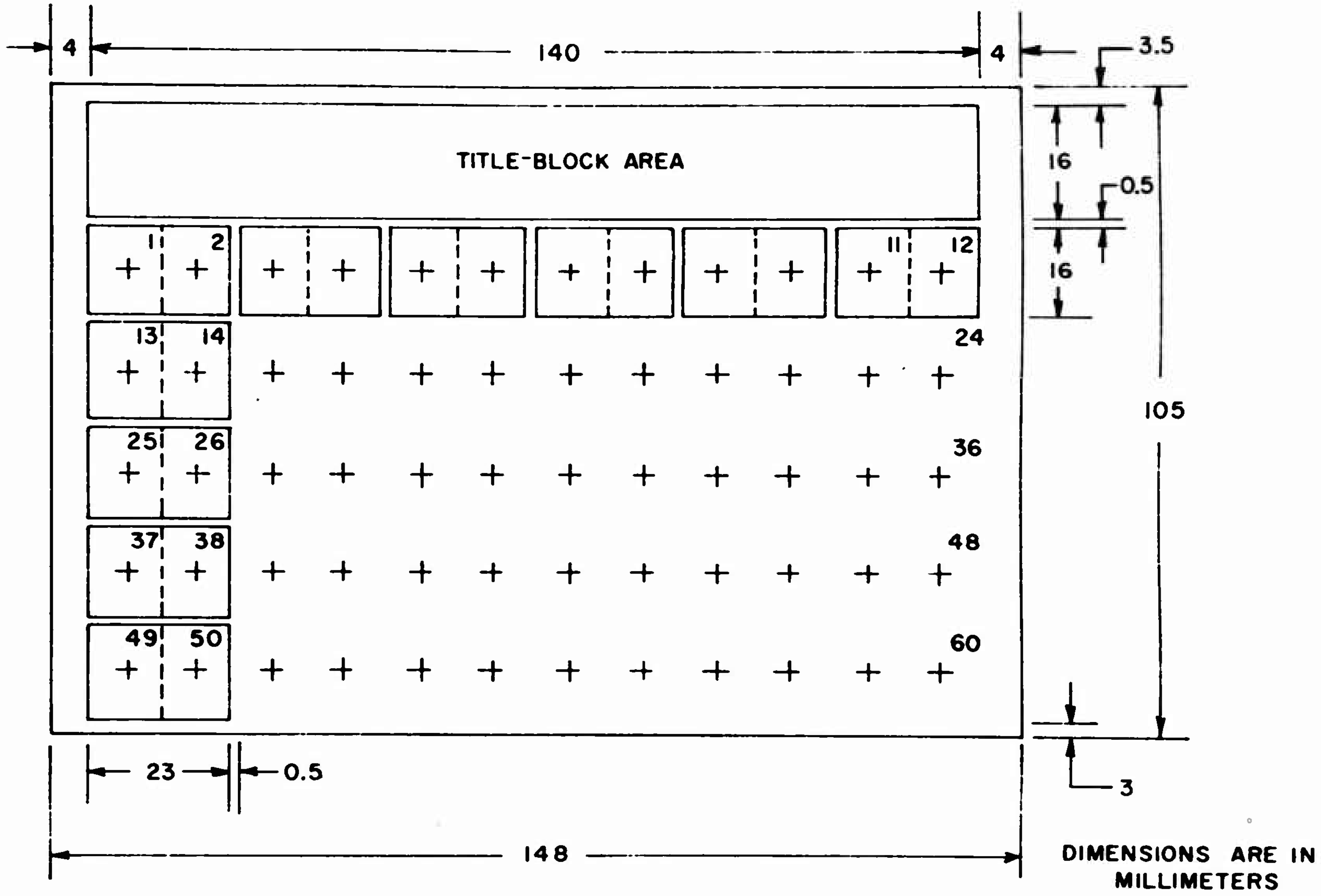

Figure 10

105 by 148 mm Microfiche Format

D-857

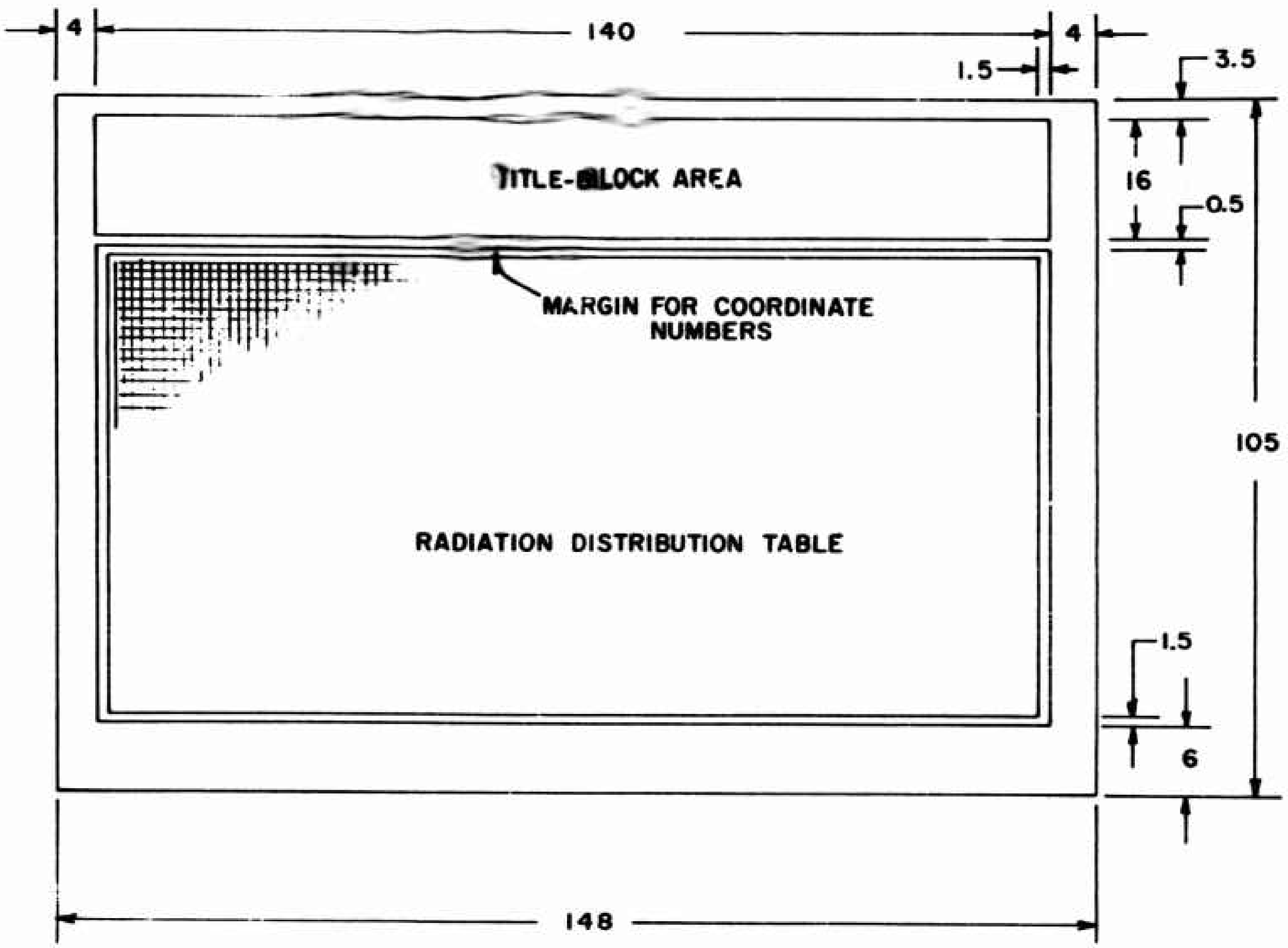

DIMENSIONS ARE IN MILLIMETERS

D-858

Figure 11

Radiation Distribution Table Dimensional Outline

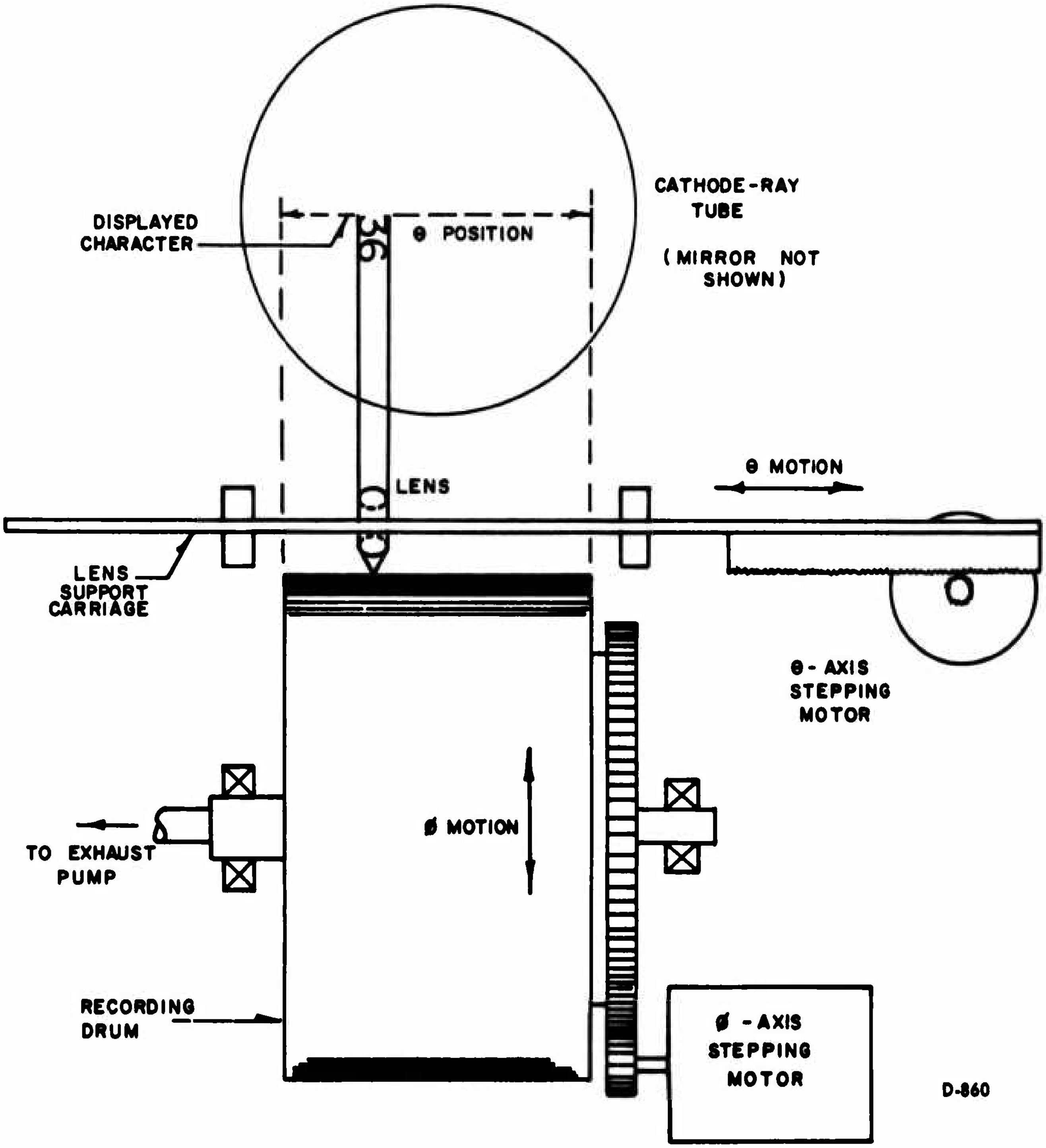

Figure 12
Recorder Section

Data are recorded in tabular form by generating characters and lines on the face of the cathode-ray tube (CRT) and focusing these onto the film. The film is positioned in the ϕ direction in increments of 0.015 inch by the ϕ-axis stepping motor. At the end of each ϕ cut the drum is stopped and the θ-axis stepping motor moves the cross carriage with lens assembly 0.015 inch to prepare for recording the next line on the radiation distribution table. The images on the face of the CRT are likewise positioned in increments of 0.015 inch after each ϕ cut to maintain axial alignment with the lens and to keep the images focused on the film. After the complete table has been recorded the lens carriage is repositioned to the starting point for recording the first line of the next table.

Figure 13 illustrates some of the features suggested for the drum assembly. The circumference of the drum is about four times the width of the table so that a complete scan in the ϕ direction corresponds to approximately 90 degrees of drum rotation. The 90-degree section under the area to be exposed contains a "vacuum-hold-down" pad. The low pressure area in the drum holds the film securely in place to prevent any slip or creep during recording and also provides good contact of the film with the drum to keep the film in focus. Atmospheric air pressure is vented to the low pressure area to release the film when the system is switched to the film advance mode.

The drum is rotated by an incremental stepping motor geared to the outer periphery of the drum. During slow speed operation when the stepping motor is operating at less than 30 steps per second, the drum is expected to have a definite start-and-stop motion. As the speed is increased up to 100 steps per second the drum is expected to move at an essentially constant velocity but under positive position control by the incremental stepping motor. The motion of the drum should be similar to that shown previously in Figure 7. At the higher stepping rates a correction must be applied to make the columns of data line up as data are recorded in either ϕ direction. This correction can be applied by positioning the characters on the cathode-ray tube an amount proportional to the lag of the drum.

2.4.4 Lens System

A high resolution cathode-ray tube of the type referred to in paragraph 2.4.6.2 can display the character information for a single data point within an area approximately 0.15 inch square on the face of the tube. The magnification factor

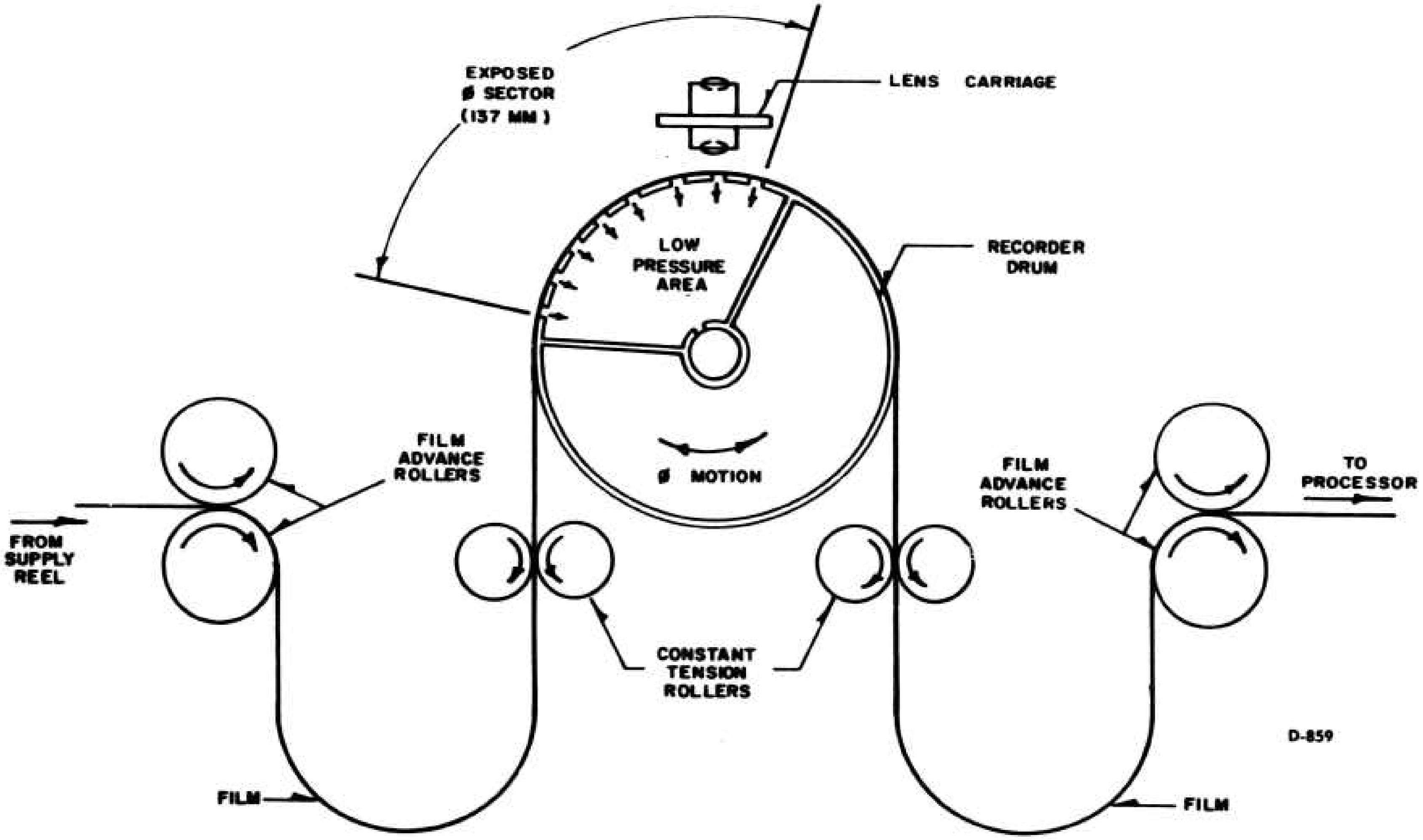

Figure 13
Recorder Drum

required for the recording lens is, therefore, approximately one-tenth. That is, the image size and image distance will be approximately one-tenth the object size and object distance. The lens requirements can easily be met with a short focal length lens designed to insure optimum transmission efficiency and focal characteristics for the optical spectrum of the cathode-ray tube. It is expected that the lens might have a focal length of about 6 mm and an effective aperture of about 3 mm.

The cell size for each data point on the film is 0.015 inch or 0.38 mm square. In order to provide reasonably distinct images, the optical system and photographic film should be capable of an overall resolution of approximately 100 lines per millimeter, or 38 lines per cell width. Resolving power of this order can be achieved without requiring extreme precautions in the lens design or an unusually fine film grain. It has been shown that the theoretical resolving power of a 1-inch diameter lens is about 5.5 arc seconds and that the resolving power is inversely proportional to the aperture. Therefore, the 3 mm lens can be expected to have a resolving power of 47 arc seconds or 2.3×10^{-4} radians. Using an image distance of 6 mm the 3 mm aperture lens should resolve a pattern of 700 lines per mm.

2.4.5 Film Processor

A number of processing techniques[5] and film processors are available for rapid processing of silver halide films. Through the use of special films and processing chemicals, together with elevated temperatures and special methods for applying processing chemicals to the film, automated negative development can be accomplished in a few seconds.

Rapid photo-processing techniques can be classified by the manner in which the processing chemicals are applied to the film.[6] The spray-processing method sequentially sprays developer, fixer, and wash onto the film within a single processing chamber. Another method forces the three processing liquids sequentially into a very thin chamber which is adjacent to the film; entry of one

---

[5] A Short Annotated Bibliography on Rapid Processing, The Department of Information Services, Research Laboratories, Eastman Kodak Company, Rochester 4, New York, October 1960.

[6] R. T. Loewe, R. L. Sisson, and P. Horowitz, "Computer Generated Displays," Proc. IRE, p. 161; January 1961.

solution forces the preceding one out of the chamber. The monobath technique uses a single solution containing all necessary processing chemicals; these chemicals have response-time characteristics such that developing, fixing, and washing take place in the proper sequence. This solution can be applied to the film by passing the film over a saturated applicator. The use of three sequential baths at three different stations is perhaps closest to conventional processing. One such method uses a saturated spongelike applicator instead of immersing the film in the liquids.

The latter method is recommended for the radiation distribution recorder based on a survey of packaged hardware available at this time and other practical considerations. The degree of complexity will depend on the results desired, primarily the processing time, keeping quality, and dryness of the film as it emerges from the processor. The optimum system would provide archival keeping quality and completely dry the film before it is ejected. The additional cost and complexity of the processor necessary to ensure a film life of greater than two years and to completely dry the film is reasonable for the benefits that these features offer.

One particular processor* that could be employed uses separate solutions to develop, fix and wash the film and dries the film with filtered warm air. The total processing time can be less than 60 seconds. In operation, the film is held against a rigid low-friction back-up plate while it is pulled at a constant rate past porous stainless-steel applicator heads. Small gaps exist between the applicator heads and the film, and a meniscus is formed across each gap as the processing solutions are fed through the heads. The solutions contact the emulsion side of the film only. Small constant-displacement pumps feed the solutions to the applicator heads. These pumps and the supply bottles are located external to the applicator head assembly for ease of servicing. A slight excess amount of the solution is supplied to the head assembly and drained off as waste; only fresh solutions are supplied to the film.

In order to reduce film access time, the developer is heated just prior to being applied to the film. The temperature of the developer is maintained constant by a proportional-controlled heat exchanger. The solutions in the reservoirs

---

*The "Rapidata" processor manufactured by Photomechanisms, Incorporated, 15 Stepar Place, Huntington Station, Long Island, New York.

are not heated. This increases the life of the chemicals and reduces the warm-up time. An automatic self-purging system flushes the applicator heads and supplies fresh solutions.

2.4.6 Recording Electronics

A simplified block diagram of the recorder electronics is given in Figure 14. The two main functions provided by this circuitry are programming and displaying character information on the cathode-ray tube. The programmer continuously monitors the positioner θ and ϕ angles and causes data to be recorded at the selected angular intervals. The programmer also provides outputs for feeding a positioner servo control unit for generation of the positioner scan functions. The programmable servo control unit is not included in this phase of the study program since it can be assembled from standard Scientific-Atlanta components for the particular positioner requirements. A discussion of the programmer and display circuitry is given in paragraphs 2.4.6.1 and 2.4.6.2.

2.4.6.1 Programmer Circuitry: Inputs to the programmer are to be obtained from the existing positioner readout system. In this system are three Wayne-George Model DD360K Digisec Optical Encoders and electronic units, one for each of the three positioner axes. During recording, only two of these axes, designated θ and ϕ, are employed. The positioner encoder and readout system provides both a visual decimal display and binary-coded decimal (BCD) outputs for recording purposes. The angles are measured to 0.001 degree and displayed from 0.000 to 359.999 degrees. In addition, the zero reference for the system can be digitally offset in 0.001 degree increments over the range of 360 degrees.

The programmer as proposed contains circuitry for automatically recording data between selectable ϕ-sector limits. These sector limits can be set by thumb-wheel switches on the front panel of the programmer. The programmer monitors the angular input data and generates trigger pulses on coincidence with the sector limits. After each line on the radiation distribution table has been recorded, the θ-axis stepper motor is automatically advanced. Provisions should also be included for recording 360-degree ϕ cuts (in one-degree increments), in which case the positioner will rotate in the same ϕ direction instead

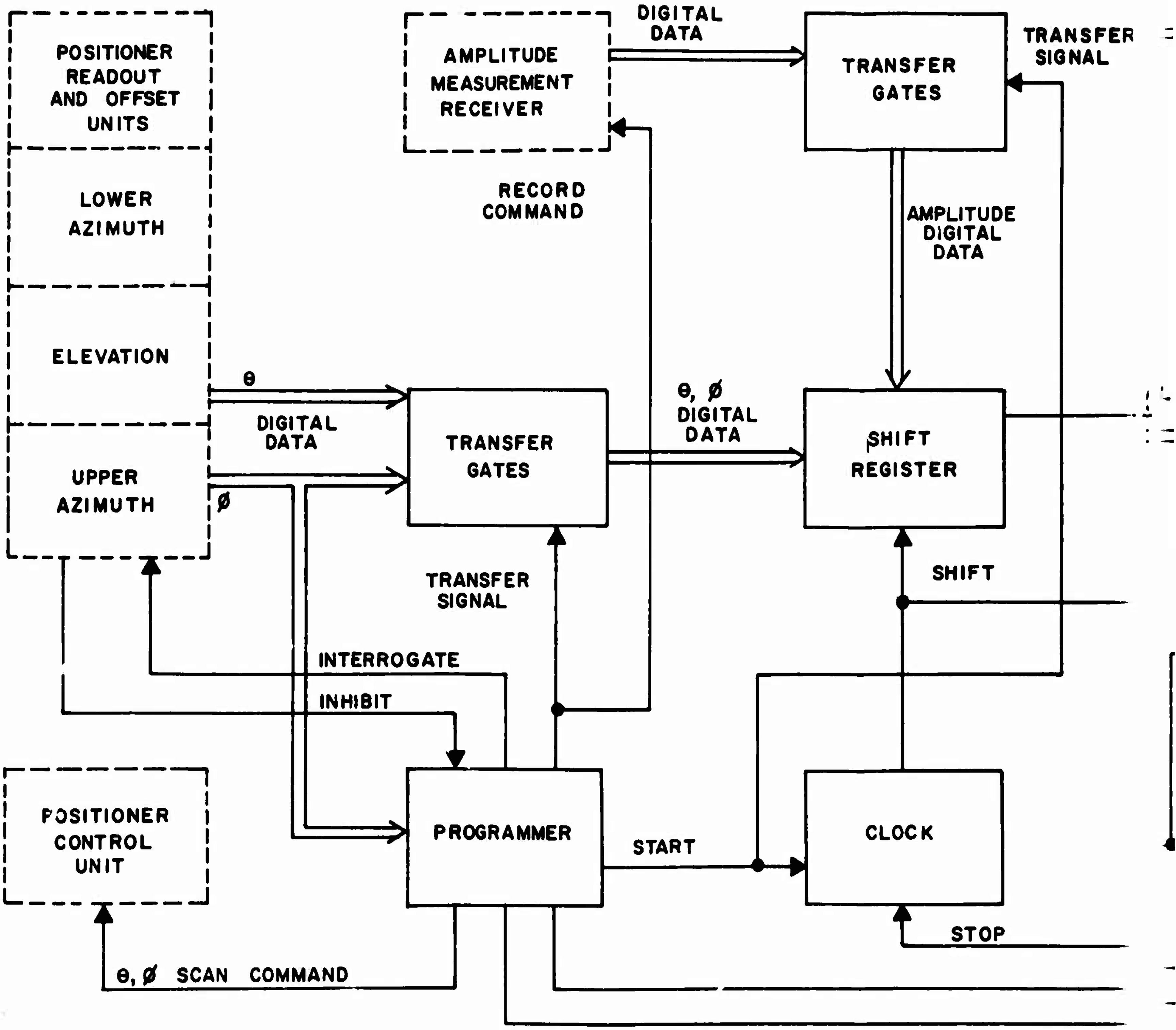
POSITIONER READOUT AND OFFSET UNITS
LOWER AZIMUTH
ELEVATION
UPPER AZIMUTH
AMPLITUDE MEASUREMENT RECEIVER
DIGITAL DATA
TRANSFER GATES
TRANSFER SIGNAL
RECORD COMMAND
AMPLITUDE DIGITAL DATA
θ
DIGITAL DATA
Ø
TRANSFER GATES
θ, Ø DIGITAL DATA
SHIFT REGISTER
TRANSFER SIGNAL
SHIFT
INTERROGATE
INHIBIT
POSITIONER CONTROL UNIT
PROGRAMMER
START
CLOCK
STOP
θ, Ø SCAN COMMAND

D-861

A

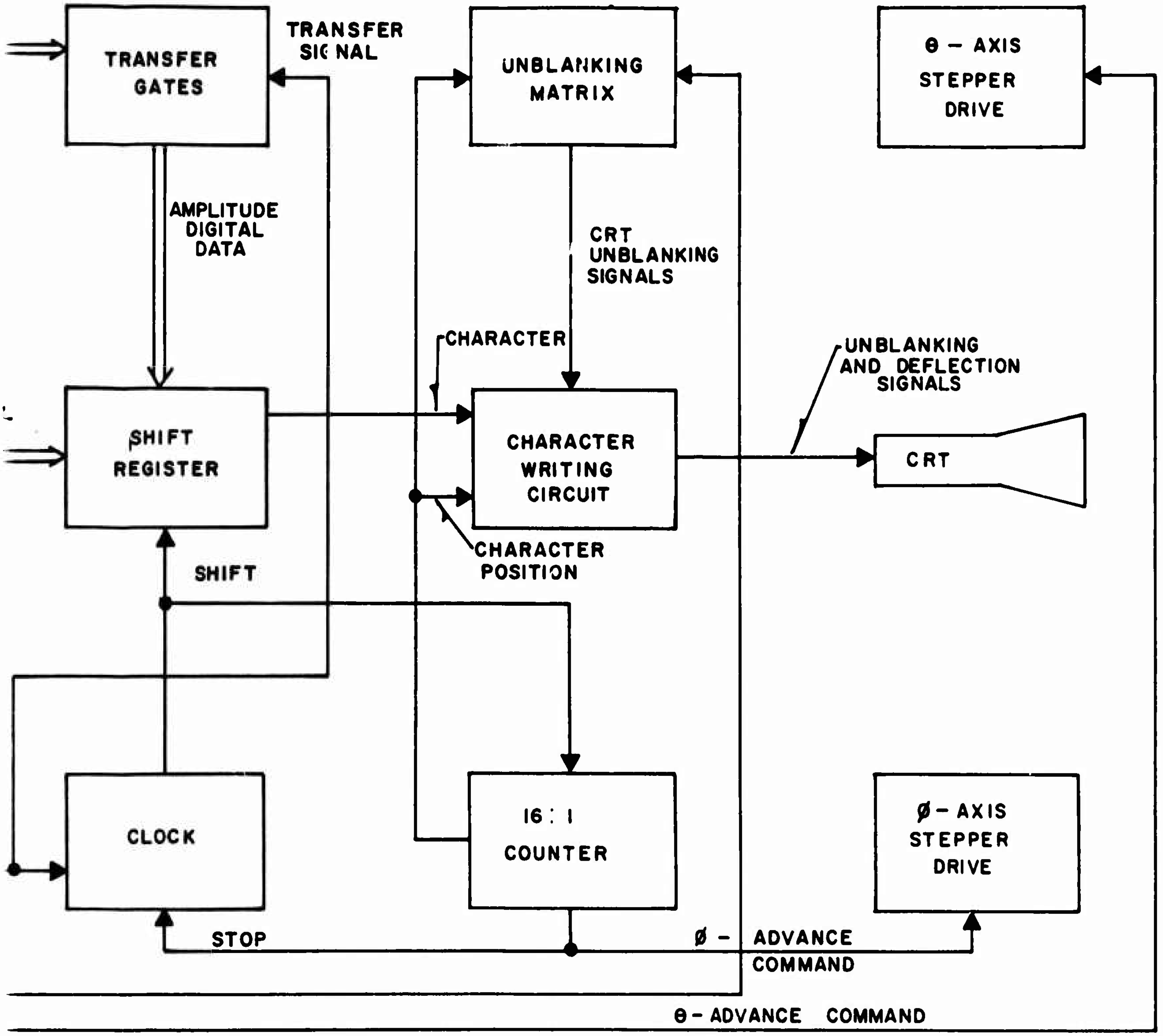

B

Figure 14

Block Diagram of Recording System

of sector scanning. In addition, the programmer should automatically stop after recording a selected number of ϕ cuts.

It is proposed that the sampling points be selectable in increments of 0.01, 0.02, 0.05, 0.1, 0.2, 0.5 and 1.0 degree. The programmer controls the recording of data in these increments by monitoring the ϕ-input angular information and generating output pulses as the positioner rotates through the chosen angular increments. These output pulses, which are referred to as record command pulses and appear as the positioner rotates between the chosen ϕ sector limits only, are fed to the receiver and display circuitry described in the following paragraphs.

2.4.6.2 Display Circuitry: Inputs to the display circuitry are obtained from the programmer and precision amplitude measurement receiver. The receiver, which is currently under development under the hardware phase of this program, digitizes the input signal level in decibels. The receiver provides four decades of visual display and binary-coded decimal outputs for recording purposes. The resolution of the receiver is 0.01 degree. The receiver may be triggered internally at a fixed 1 kc sampling rate or externally at a variable rate. When operating with the radiation distribution recorder, the receiver is triggered by the record command pulse from the programmer, causing the input signal level to be sampled and digitized, and the digital outputs are fed to the display circuitry.

The function of the display circuitry is to process the input data and generate a display on the face of the cathode-ray tube in the format shown in Figure 4. A total of up to 16 steps may be required to display all information on the CRT for a single data point. The individual characters and symbols to be displayed are as follows:

(1) two amplitude numerals,
(2) four numerals for major ϕ coordinates,
(3) four numerals for major θ coordinates,
(4) major coordinate identification dots, and
(5) contour identification symbols.

Since, practically speaking, only a single character can be displayed at a time on the face of the CRT, it will be necessary to display the above data sequentially. The characters to be displayed (amplitude numerals and θ, ϕ coordinates) are fed through transfer gates to a shift register upon receipt of the record command pulse. The θ, ϕ digital data are obtained from the positioner readout system previously referred to. The record command pulse also initiates the recording cycle after the digital data have been transferred by triggering a clock. The output of the clock shifts the contents of the storage register a character at a time into the character generating circuits and simultaneously triggers a 16:1 counter.

The output from the 16:1 counter and outputs from the programmer are fed to the unblanking matrix and character writing circuits. The unblanking matrix controls the blanking of the CRT so that only certain characters contained in the shift register are displayed at each data point. Thus, the unit- and tenth-decibel characters are unblanked if the signal level is greater than 10 decibels, and the tens- and units-decibel characters are unblanked for signal levels of 10 decibels or less. The θ, ϕ characters and coordinate dots are unblanked only when the positioner is at a major coordinate value. Furthermore, the θ and ϕ characters must be unblanked only when data points at the periphery of the table are being recorded, so that the major θ, ϕ values will be recorded in the margin surrounding the radiation distribution table. In addition to the logic circuitry for the above functions, circuitry must be incorporated to cause the contour identification symbol to be unblanked when the signal level is within the selected contour increment.

The character-writing circuits generate characters and symbols in response to the digital outputs from the shift register. Thus, as each character or symbol is shifted into the character-writing circuit from the shift register it is displayed on the CRT provided the CRT is unblanked by the unblanking matrix. The character-writing circuits, in addition, position each character to a given location on the CRT in response to outputs from the 16:1 counter and programmer.

It is proposed that a shaped-beam CHARACTRON CRT[7] manufactured by General Dynamics/Electronics be employed. In this tube, electrons from the cathode flood a matrix stencil to form individual character-shaped beams. The character to be displayed is selected by electrostatically deflecting the shaped

---

[7] J. H. Redman, "Advanced Display Techniques Through the CHARACTRON Shaped Beam Tube," presented at the First National Symposium of the Society for Information Display, March 14, 1963.

beams to allow only the selected character to pass through an aperture. The selected character is then deflected by a magnetic deflection yoke to the desired location on the fact of the CRT. Since the shape of the character is determined by the stencil within the tube, good character readability can be achieved.

2.4.7 Peripheral Equipment

Equipment should be incorporated in the recording system to make contact duplicates of the microfiche original and to view and print enlargements. Contact prints can be made on Kalvar film with a small commercial microfilm printer. Units of this type expose Kalvar by intense ultraviolet light and fix the image by heating the film to 240°F or higher for a few seconds. In addition to providing duplicate microfilm records, the Kalvar process offers the following advantages:

(a) Virtually unlimited shelf life of unexposed film,
(b) Unexposed film may be handled briefly in ordinary room light,
(c) Film processed without chemicals,
(d) Processed film may be handled without damage,
(e) Archival keeping quality of developed film, and
(f) A positive duplicate is obtained from the original negative.

The latter point is of particular importance; an image reversal from the original negative is necessary to project for viewing bright numbers on a dark background or to print black numbers on a white background in a photographic enlarger.

A considerable amount of commercial equipment is available for viewing microfilm documents and printing full-size copies. This equipment is generally combined into a single viewer-printer unit, and, in most cases, the copy is made on special photographic paper. These viewer-printers contain a monobath or stabilization processor to develop the exposed paper. The total time required to obtain a print is less than one-half minute, and the print emerges slightly damp but dry enough to be handled. The size of the viewing screen and hard copy output are generally limited to a maximum of 18x24 inches in the more common units. It is expected that certain modifications will be required to a standard viewer-printer to incorporate special features for use in the recording system.

3. INVESTIGATION OF ENVIRONMENTAL EFFECTS ON ACCURACY OF ANTENNA MEASUREMENTS

3.1 Statement of Problem

Basic to the problem of obtaining accurate antenna measurements is the achievement of adequate simulation of the expected operational environment of the antenna under test. When related to antenna pattern measurements, the problem involves that of illuminating the test antenna[8] with an incident wave which is essentially constant in amplitude and phase over the test aperture. The requirement arises from the fact that most antennas operate over ranges which are very large compared to the size of the antenna aperture. The major sources of error which result in poor simulation of the operational environment are

(a) variation of the phase of the incident field over the aperture,
(b) variation of the amplitude of the incident field over the aperture,
(c) mutual coupling between the transmitting and receiving antennas,
(d) inhomogeneities of the atmosphere, and
(e) reflections and other extraneous signals.

The aforementioned factors have been discussed in a previous report submitted by Scientific-Atlanta, Inc., to Rome Air Development Center.[9] In particular, the antenna range design criteria which are imposed by phase and amplitude variations over the test aperture are derived. Briefly, the commonly accepted minimum separation is given by

$$R \geq \frac{2d^2}{\lambda} \tag{1a}$$

and

$$R > 10\lambda \tag{1b}$$

where d is the maximum dimension of the test aperture and λ is the wavelength.

---

[8] This report will consider all antennas to be tested on receiving. The receiving pattern thus obtained will be identical to the transmitting pattern, in accordance with the Rayleigh-Helmholtz reciprocity theorem, for all antennas except for those containing non-reciprocal components, such as ferrites. This pattern will be referred to as the radiation pattern with the understanding that the discussion refers to reciprocal antennas.

[9] FR-I, Chapter 2.

The separation of (la) limits the phase error over the test aperture to a maximum of $\pi/8$ radians, which is acceptable for many measurement purposes, although a greater separation is required for measurement of the pattern details in the vicinity of nulls. When d is less than λ, the separation of (lb) is required to remove the test antenna from the induction field of the transmitting antenna.

The maximum amplitude taper of the transmitted beam over the test aperture is restricted to a maximum value of 0.25 db if the maximum dimension of the transmitting aperture, d_t, is given by

$$d_t = \frac{R\lambda}{4d} \quad . \tag{2}$$

The error arising from mutual coupling can be noticeable if the gain of the transmitting antenna is too great. This type of error affects the peak of the main lobe, primarily, and does not significantly affect the sidelobe level; however, because of the error in measurement of the level of the pattern maximum, there is an apparent error in the measured sidelobe levels. Coupling errors may be suppressed by reducing the gain of the transmitting antenna to a reasonable level. Estimates of error from this source are given in reference 9.

Atmospheric inhomogeneities cause a phase variation across the receiving aperture which combines with the phase error due to the curvature of the phase front and the intrinsic error of the antenna to affect the total signal at the test aperture. The rms atmospheric phase error across a 50-foot aperture, at 10 Gc, for typical weather conditions, has been calculated[10] to be approximately 3 degrees for a 50,000-foot range. Severe atmospheric turbulence or higher operational frequencies would result in higher values, but, for a range of 7500 feet, the phase error should be negligible. The major remaining sources of environmental error are from extraneous signals caused by reflections, or by radio interference from outside sources.

The discussion which follows will apply to reflections. Reflections interfere with the direct signal at the test aperture and distort the field as demonstrated in the following example. Consider the case of a plane wave of amplitude E_d

---

[10] Ibid

which is normally incident on the test aperture as shown in Figure 15(a). Let an extraneous signal of amplitude E_r enter the aperture at an angle θ from the normal. At any point in time, the phase of the direct wave will be constant across the aperture so that the field may be expressed as

$$\bar{E}_d = E_d e^{j(\phi + \omega t)} \quad , \qquad (3)$$

while the phase of the extraneous wave will vary across the aperture so that the extraneous field is given by

$$\bar{E}_r = E_r e^{j(\phi' + \omega t)} \qquad (4)$$

where ϕ and ϕ' are constants, λ is the wavelength, and x is distance measured across the aperture parallel to the plane containing the directions of propagation of E_d and E_r. The total field in the aperture is then given by

$$\bar{E}_t = \bar{E}_d + \bar{E}_r = \left[E_d e^{j\phi} + E_r e^{j\left(\frac{2\pi x \sin\theta}{\lambda} + \phi'\right)} \right] e^{j\omega t} \qquad (5)$$

Equation (5) describes a field with a sinusoidal variation in one dimension as sketched in Figure 15(b). E_{r_1} and E_{r_2} represent two successive phase fronts of the reflected wave separated by λ, and E_d is a phase front of the direct wave. At points x_1 and x_2 the two waves are assumed to be in phase. The resulting field at x_1 and x_2 is

$$E_{max} = E_d + E_r \quad .$$

Halfway between these two points the waves are in phase opposition and the resultant amplitude is

$$E_{min} = E_d - E_r \quad .$$

The total amplitude variation within the aperture is given by

$$E_t = E_{max} - E_{min} = 2E_r \quad . \qquad (6)$$

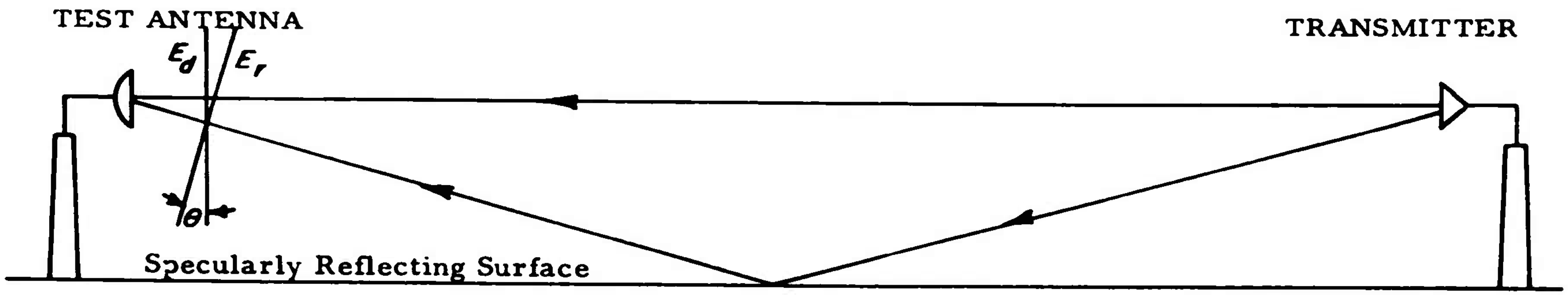

(a) Reflected Wave Incident on a Test Aperture at an Angle θ from the Direction of Propagation of the Direct Wave

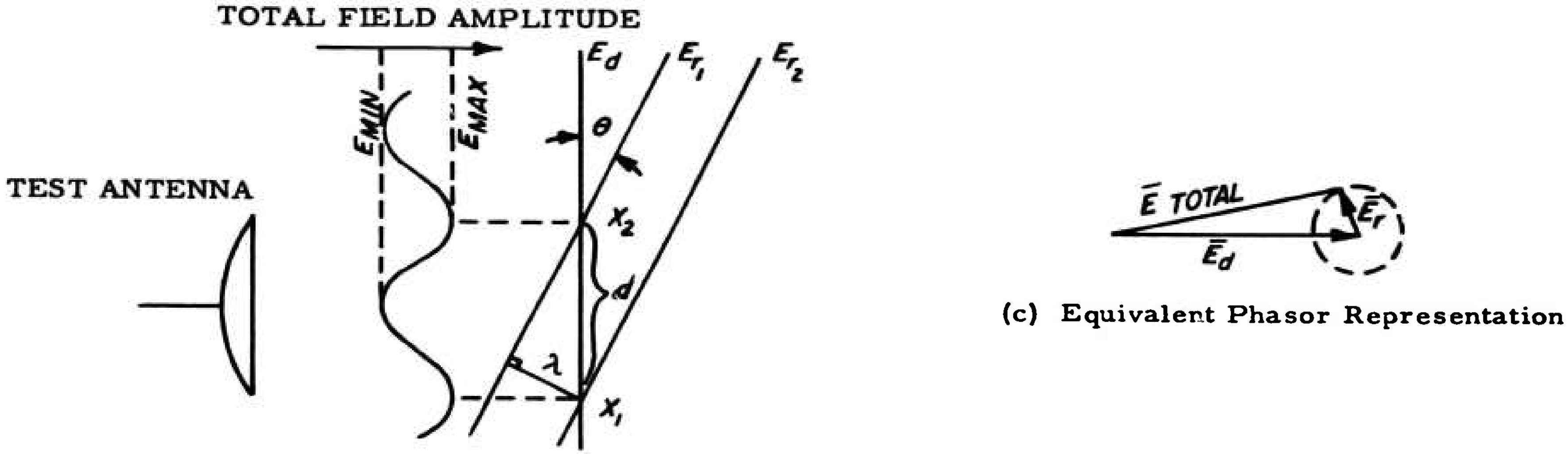

(b) Details of Wave Interference

(c) Equivalent Phasor Representation

Figure 15. Simplified Sketch Illustrating Total Aperture Field Variation Caused by a Single Specularly Reflected Wave

The angle θ can be determined by

$$\theta = \sin^{-1} \frac{\lambda}{d} \tag{7}$$

where d is seen in Figure 15(b) to be the distance between two successive peaks of the standing wave.

The field in the aperture may also be represented as the sum of two phasors, E_d and E_r as illustrated in Figure 15(c), where E_r rotates about the tip of E_d. The phase of the field across the aperture will vary as the phase of this sum. The total phase variation is

$$\Delta\phi = 2 \tan^{-1} \frac{E_r}{E_d} \tag{8}$$

The preceding example, although representing an idealized reflection, demonstrates the manner in which extraneous signals distort an otherwise planar wavefront. In a more realistic case, neither the direct nor the extraneous waves would be strictly planar, and there would be many extraneous signal sources which could contribute to the total aperture field. Therefore the aperture field would not be distorted in such a simple fashion; on the other hand, a simple model such as equation (5) is often quite useful in studying cases where one reflection is somewhat stronger than others which are present.

Reflections may be caused by any object or surface in the vicinity of the test range, although reflections from the range surface lying under the transmission path are usually more serious than those coming from sources lying at large horizontal angles from the line of sight, due to the decreased probability of specular reflection of the latter and the discrimination provided by the directivity of the antenna under test.

The reflections may be roughly classified in two groups, specular reflection and diffuse scattering. Specular reflection obeys well known optical principles and is characterized by phase coherence. If the reflecting surface is sufficiently smooth and lossless, the coefficient of specular reflection can approach unity for a plane surface and can exceed unity for concave surfaces. When path lengths much longer than a wavelength are involved, a single specularly reflected wave can approximate the idealized case presented above, and a regular interference pattern may result.

Diffuse scattering results from the summation of wavelets scattered from all points of a rough surface. If the surface is smooth, the incremental contributions over the surface will cancel except for the energy which is radiated in the specular direction. If the surface is periodically rough, regular cancellation and enforcement will result and a set of grating lobes will be formed. If the surface is randomly rough with variations spaced less than a wavelength apart, diffuse scattering will radiate energy in all directions. The scattering pattern becomes increasingly omnidirectional as the magnitudes of surface variations increase. Figure 16 illustrates the qualitative effect of increasing surface roughness on the scattering pattern.

The transition from diffuse to specular reflection is a gradual change as shown in Figure 16. Several authors have established surface "roughness" criteria which define the difference between the two states. The vell-known Rayleigh criterion, proposed by Lord Rayleigh, is given by

$$\Delta h < \frac{\lambda}{k \sin\gamma} , \qquad (9)$$

where Δh (Figure 17) represents the height of a surface irregularity, k is a constant, and γ is the grazing angle. This criterion is based on the quasi-geometrical optics approach, which is often employed in problems of this type where the wave is assumed to propagate by means of rays even though the wavelength is not vanishingly short as required by geometrical optics.

The derivation of the criterion is illustrated in by Figure 17(b). Consider two rays from a plane wave front, F_1, which approach a surface on which a pedestal of height Δh is located. Let the ray a strike the top of the pedestal and let the ray b strike the plane surface near the pedestal. Let the two rays be reflected in accordance with Fermat's laws of reflection[11] from the two surfaces and proceed to form part of a second front at F_2. The Rayleigh criterion is based on the geometrical difference in path length traversed by the rays in travelling from F_1 to F_2 (Figure 17b). Let the distance traversed by ray a be $d_1 + d_2$.

---

[11] Silver, S, Microwave Antenna Theory and Design, Radiation Laboratory Series, Volume 13, pp. 122-128, McGraw-Hill Co., 1949.

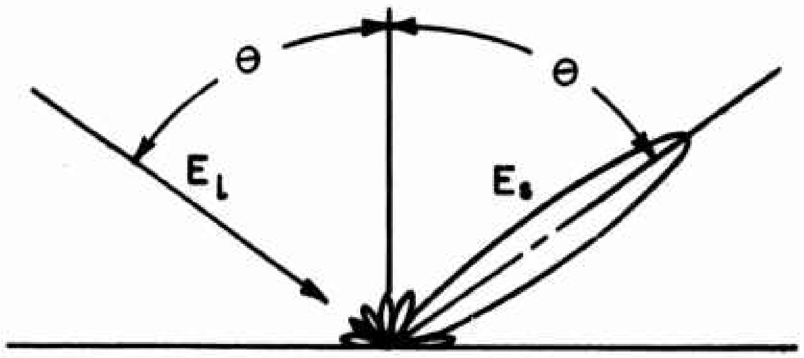

(a) Smooth Surface--Specular Reflection

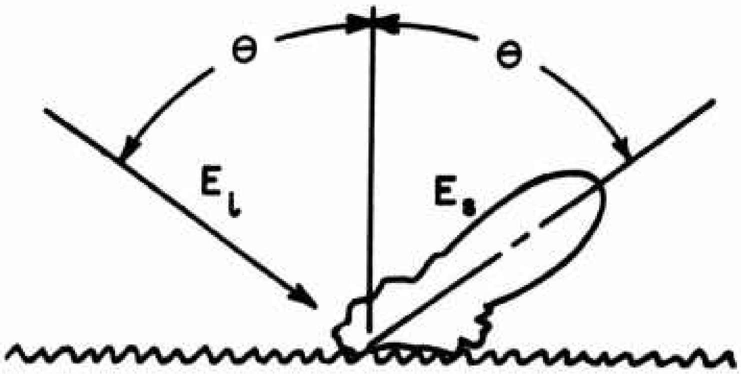

(b) Moderately Rough Surface--Partial Specular Reflection

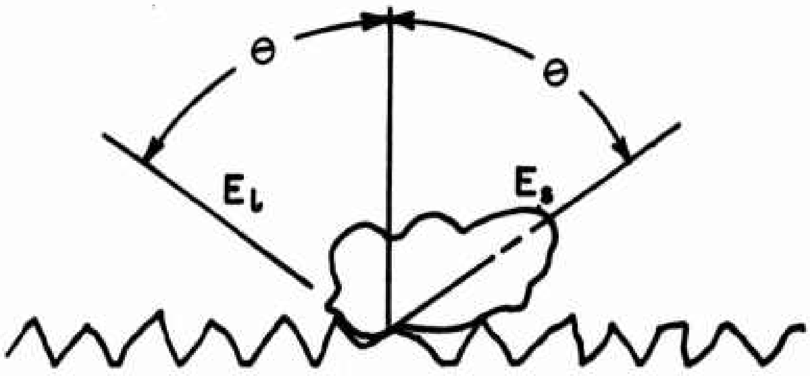

(c) Very Rough Surface--Diffuse Scattering

Figure 16. Sketch Showing the Qualitative Effect of Increasing Roughness on the Distribution of Scattered Energy from a Reflecting Surface

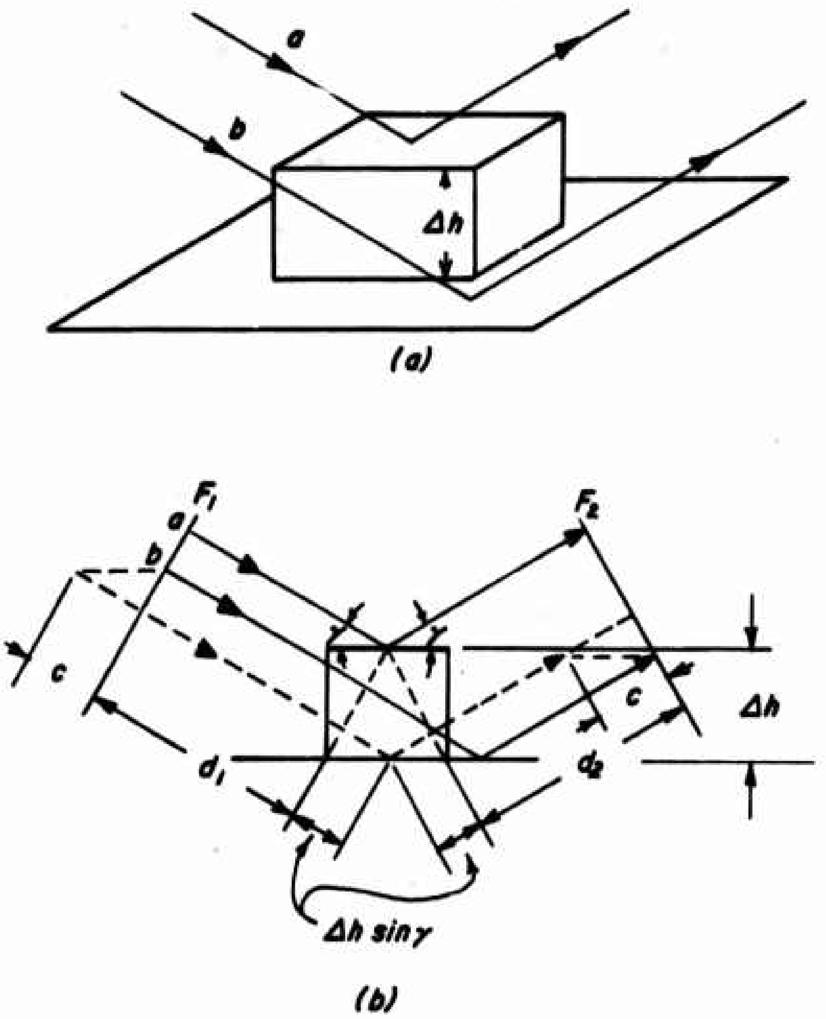

Figure 17. Phase Difference Between Rays Reflected From Two Levels

From inspection it can be seen that ray b will travel the distance $d_1 + d_2 - c + c + 2\Delta h \sin\gamma$ and that the difference in path length Δd is given by

$$\Delta d = 2\Delta h \sin\gamma \quad . \tag{10}$$

Letting $\Delta d < 2\lambda/k$ gives the criterion of (9).

For values of Δh less than $\lambda/k \sin\gamma$ the surface is regarded as smooth and essentially specularly reflecting, while for larger surface perturbations, the surface is assumed to be rough and, hence, a diffuse scatterer. Lord Rayleigh suggested a value of 8 for k, which corresponds to a phase difference of $\pi/2$, while other authors[12] have suggested values ranging as high as 32, corresponding to a difference of $\pi/8$.

Another approach is to regard reflected energy as the sum of a specularly reflected component and a diffuse component; the two types of reflection can then be treated separately. The following section summarizes the theoretical development of the problem of reflections from a random rough surface. The resulting expressions are applied in Section 3.4 to the specific problem of determining the probable level of reflections at the RADC antenna test range at Newport, New York.

3.2 Theoretical Development

The problem of reflection from a rough surface involves determining the magnitude and polarization of the energy reradiated by a reflecting surface. Rigorous treatment of the problem includes consideration of cross polarization effects, requiring that the reflections be analyzed as a vector problem. The investigation may be simplified by considering the individual orthogonal components of the reflected field separately. This approach reduces the vector problem to a scalar problem where the reflected signal is assumed to possess the same polarization as the transmitted signal. The three dimensional, scalar scattering problem is one of determining a function, E_r, interior to a surface, S, enclosing a source-free volume which is a solution of the scalar Helmholtz equation

$$(\nabla^2 + k^2) E_r = 0 \quad , \qquad (11)$$

and which satisfies the boundary conditions imposed by Maxwell's equations at S. The problem has been treated by numerous authors,[13-19] and the detailed mathematics will not be presented here. The following paragraphs summarize the theory upon which this study is based.

---

[12] Kerr, D. E., Propagation of Short Radio Waves, Radiation Laboratory Series, Volume 13, McGraw-Hill Co., 1951, p. 411 and footnote, p. 416.

[13] Clarke, R. H., and G. O. Hendry, "Prediction and Measurement of the Coherent and Incoherent Power Reflected from a Rough Surface," IEEE Transactions on Antennas and Propagation, Volume AP-12, No. 3, May 1964; pp. 353-363.

[14] Beckmann, Petr, "Shadowing of Random Rough Surfaces," IEEE Transactions on Antennas and Propagation, Volume AP-13, No. 3, May 1965; pp. 384-388.

Consider a surface, S, which encloses a source-free volume, V, as illustrated in Figure 18. A transmitting antenna, T, and an observation point, P, are located exterior to the surface. The point, P, is surrounded by a sphere, S', of radius, R, which is connected to the outside of the surface by a tubular surface, S''. The point, P, represents a point in the aperture of the test antenna,

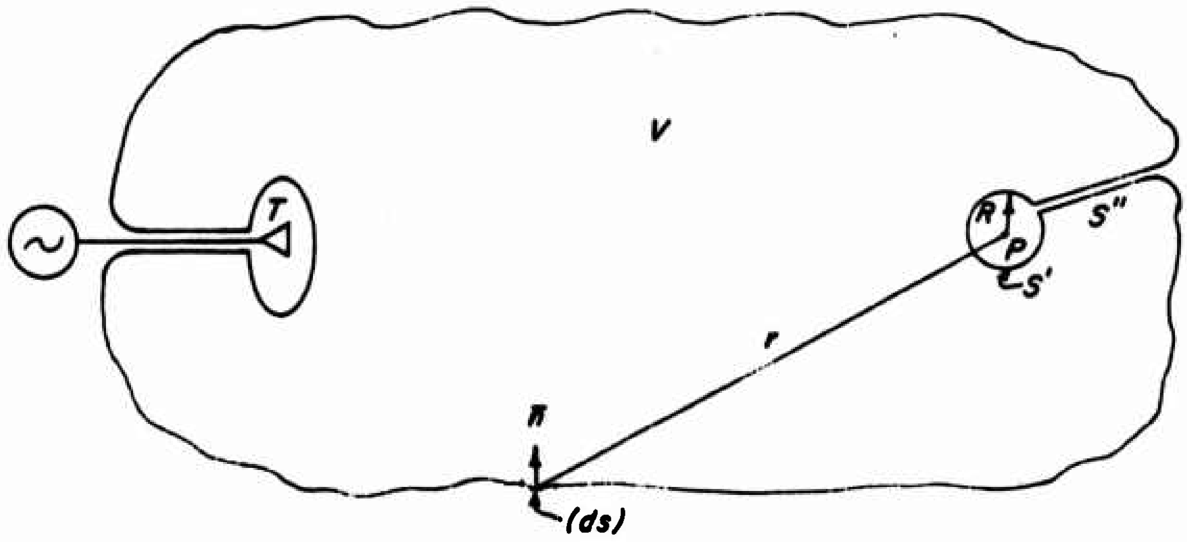

Figure 18. Sketch of the Geometry Relating to the Helmholtz Integral

---

[15] Twersky, Victor, "Signals, Scatterers, and Statistics," IEEE Transactions on Antennas and Propagation, November 1963; pp. 668-680.

[16] Twersky, Victor, "On Scattering and Reflection of Electromagnetic Waves by Rough Surfaces," IRE Transactions on Antennas and Propagation, January 1957; pp. 81-90.

[17] Beckmann, Petr, and Andre Spizzichino, The Scattering of Electro-Magnetic Waves from Rough Surfaces, The MacMillan Company, 1963; pp. 9-10.

[18] Silver, op cit, Chapter 5.

[19] Kerr, Donald E., Propagation of Short Radio Waves, McGraw-Hill Book Company, 1951; Volume 13, Chapter 5.

while the surface, S, includes the antenna range surface and an imaginary surface in the atmosphere above the test range. If E is a solution to the equation (11) which is regular at infinity, and if the radius, R, is allowed to go to zero, then the value of the integral[20]

$$I(P) = \iint_S \left[\frac{e^{jkr}}{r} \frac{\partial E}{\partial n} - E \frac{\partial}{\partial n} \frac{e^{jkr}}{r} \right] dS \tag{12}$$

is given by

$$I(P) = -4\pi E(P) \tag{13}$$

Here, $\partial/\partial n$ denotes differentiation along a normal direction into the closed surface, and r represents the distance from P to a surface increment, dS. This integral, which follows directly from the divergence theorem and Green's theorem, is known as the Helmholtz integral; it gives the value E(P) for points interior to S in terms of the values of E and its normal derivatives over S.

The surface S can be considered to be the sum of several surface regions S_i such that

$$S = \sum_{i=1}^{n} S_i \tag{14}$$

The contribution of any surface region to the field at P is given by

$$E(P) = \frac{1}{4\pi} \iint_{S_i} \left[\frac{e^{jkr}}{r} \frac{\partial E}{\partial n} - E \frac{\partial}{\partial n} \frac{e^{jkr}}{r} \right] dS_i \tag{15}$$

A typical surface region, s, where s is some S_i illuminated by a plane wave, E_1, is shown in Figure 19. The surface is defined by the function $\zeta(x, y)$ and its projected area in the xy plane is equal to A. The incident wave arrives from the negative x direction at an angle θ_1 from the z axis and parallel to the x axis, with the propagation vector $\overline{k}_2$ a vector in the direction of the reflected wave. The magnitudes of $\overline{k}_1$ and $\overline{k}_2$ are $2\pi/\lambda$. The direction to the point of observation P is defined by elevation and azimuth angles θ_2 and ϕ_2, respectively. Equation (12) can be used to determine the contribution of s to the field at P. The total field will be given by the summation of all such contributions.

---

[20] Baker, B. B., and E. T. Copson, The Mathematical Theory of Huygen's Principle, Oxford University Press, London, 1950; pp. 23-32.

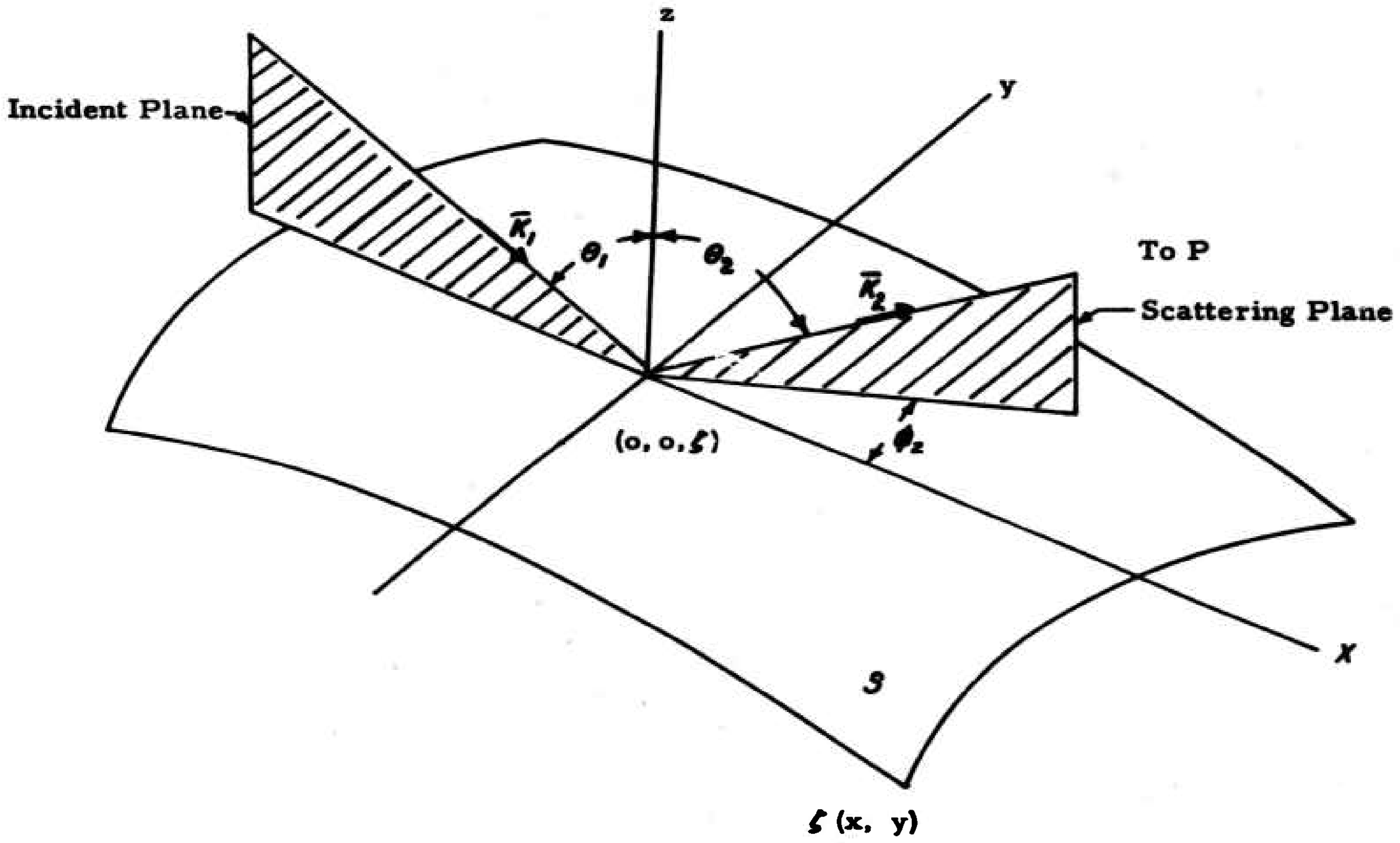

Figure 19. Coordinate System for Scattering from a Surface

In order to solve equation (15), the boundary values for E and ∂E/∂n must be known over S. Exact determination of the boundary conditions is impossible for a random rough surface; hence approximations are necessary. Beckmann[21] takes the field at any point to be equal to the field that would be present on a tangential, smooth plane at that point. This approximation is quite good for slowly varying surfaces and less valid for rough surfaces with sharp edges. With this approximation, the boundary values are

$$E_s = (1 + R_o)E_1 \tag{16a}$$

and

$$\frac{\partial E}{\partial n_s} = (1 - R_o)E_1 \bar{k}_1 \cdot \bar{n} \quad , \tag{16b}$$

where $\bar{n}$ is the unit vector normal to the surface, and R_o is the coefficient of reflection of a smooth surface. The value of R_o is dependent on the polarization of E_1 and is shown by Jordan[22] to be

$$R_V = \frac{\frac{\epsilon_2\mu_1}{\epsilon_1\mu_2}\cos\theta - \sqrt{\frac{\epsilon_2\mu_1}{\epsilon_1\mu_2} - \sin^2\theta}}{\frac{\epsilon_2\mu_1}{\epsilon_1\mu_2}\cos\theta + \sqrt{\frac{\epsilon_2\mu_1}{\epsilon_1\mu_2} - \sin^2\theta}} \tag{17a}$$

or

$$R_H = \frac{\cos\theta - \sqrt{\frac{\epsilon_2\mu_1}{\epsilon_1\mu_2} - \sin^2\theta}}{\cos\theta + \sqrt{\frac{\epsilon_2\mu_1}{\epsilon_1\mu_2} - \sin^2\theta}} \tag{17b}$$

where ϵ_1 and μ_1 are the permittivity and permeability of the propagating medium, ϵ_2 and μ_2 are those of the reflecting medium, θ is the "local" angle of incidence and where R_H and R_V denote the coefficients of horizontal and vertical polarization respectively. Vertical polarization is defined as polarization in which the $\bar{E}$ vector lies in the plane defined by $\bar{k}_1$ and $\bar{n}$, while horizontal polarization is

---

[21] Beckmann, op cit.

[22] Jordan, E. C., Electromagnetic Waves and Radiating Systems, Prentice-Hall, Englewood Cliffs, New Jersey, 1950; pp. 132-142.

perpendicular to this plane. When $\mu_1=\mu_2=\mu_o$, and when the propagating medium is free space ($\epsilon_1=\epsilon_o$), equations (17) reduce to

$$R_V = \frac{\epsilon_r \cos\theta - \sqrt{\epsilon_r - \sin^2\theta}}{\epsilon_r \cos\theta + \sqrt{\epsilon_r - \sin^2\theta}} \tag{18a}$$

and

$$R_H = \frac{\cos\theta - \sqrt{\epsilon_r - \sin^2\theta}}{\cos\theta + \sqrt{\epsilon_r - \sin^2\theta}} \tag{18b}$$

where ϵ_r is the complex relative permittivity of the reflecting medium.

Equation (15) is modified to solve for the coefficient of reflection rather than the reflected field by dividing both sides by the field which would be reflected in the specular direction by a smooth plane. If the reflecting surface is given by $\zeta(x, y)$, the radius vector, $\bar{r}$, is defined as

$$\bar{r} = x\bar{x}_o + y\bar{y}_o + \zeta\bar{z}_o \ , \tag{19}$$

where $\bar{x}_o$, $\bar{y}_o$, and $\bar{z}_o$ are unit orthogonal vectors defined by the coordinate system. The coefficient of reflection of the surface is then[23]

$$\rho = \frac{F_3}{A} \iint_S e^{j\bar{v}\cdot\bar{r}}\, dS \tag{20}$$

where A is the area of the surface,

$$F_3 = R_o \left[\frac{1 + \cos\theta_1 \cos\theta_2 - \sin\theta_1 \sin\theta_2 \cos\phi_2}{\cos\theta_1(\cos\theta_1 + \cos\theta_2)}\right] \tag{21a}$$

and

$$\begin{aligned} v &= \bar{k}_1 - \bar{k}_2 \\ &= \frac{2\pi}{\lambda}\left[(\sin\theta_1 - \cos\phi_2 \sin\theta_2)\bar{x}_o - (\sin\theta_2 \sin\phi_2)\bar{y}_o + (\cos\theta_1 + \cos\theta_2)\bar{z}_o\right] \end{aligned} \tag{21b}$$

---

[23] Beckmann and Spizzichino, op. cit., p. 27.

Equation (20) neglects second-order terms called "edge effects." However, these are small when

$$A >> \lambda^2$$

The discussion of this section provides a background for predicting the distribution of scattered energy from a reflecting surface, but requires definition of the character of the reflecting surface before equation (20) can be applied to the solution of practical problems. Equation (20) gives a value of reflection coefficient for an arbitrary rough surface if one can describe the detailed character of the surface. The accuracy of the result depends on the degree to which the physics of the actual problem adheres to the restrictions which have been made.

Several approximations were required to arrive at the form expressed in (20). The more significant assumptions are:

A. The reflection coefficient, R_o, is assumed to be constant over the region of integration. This case may be realized in practice by dividing the surface into areas of different reflection characteristics, such as bare ground, rocks, wooded ground, etc.

B. Shadowing and multiple scattering effects are ignored. This approximation is valid if the surface is gently varying. Extremely rough surfaces require the introduction of a "shadowing factor" in the expression for which will account for the fact that all of the surface is not illuminated. Such a factor has been derived by Beckmann[24].

C. The incident wave is linearly polarized with the $\bar{E}$ vector either in the incident plane or perpendicular to it. No prediction is made concerning the polarization of the scattered energy. A rough reflecting surface is known to cause depolarization, but the problem of a random rough surface has not been solved or even extensively studied. Little can be said, consequently, except that the degree of depolarization would be expected to be less for relatively smooth surfaces than for rougher surfaces.

---

[24] Beckmann, op. cit.

D. The transmitter and the point of observation, P, are sufficiently far removed from the surface, S, that plane wave approximations can be employed. At first thought, this might seem to imply that the analysis is not valid for transmitter and point of observation separations of distances such as those employed in antenna ranges. This is not so, however, because, while the definition of ρ in (20) is defined such that ρ is unity for a planar surface its definition does not require an identically plane wave. It will be shown that the reflection coefficient of concave surfaces can exceed unity because of the finite radius of curvature of the incident phase front and the finite distance from the reflecting surface to the field point.

The above approximations do not seriously impair the theoretical results. The analysis stands or falls on the validity of the boundary conditions which are used; hence discretion must be used in application of equation (20) to a specific surface. Generally, one would expect the coefficient of reflection for the specular direction to be somewhat less for a surface composed of sharp edges than for a smoother surface with the same heights of perturbations.

3.3 Postulation of a Model of the Reflecting Surface

In order to evaluate equation (20), the function $\zeta(x, y)$ must be known explicitly. This is clearly not practical for most rough surfaces, so that the solution, as expressed in equation (20) is not a useful form. Most authors have attempted to find solutions based on statistical methods. The crux of this problem is in the postulation of a model which adequately describes the scattering action of the surface under investigation. Many such models have been proposed, including random arrays of spheres, mirrors, and other shapes. Different models will in general yield somewhat different results, so that the proper choice of a model has been a point of extensive investigation. Beckmann and Spizzichino suggest a normal (Gaussian) distribution of ζ over the surface, with $\langle \zeta \rangle = 0$, where the symbols $\langle \; \rangle$ are employed to indicate a mean value. The results derived with this model will be discussed in this report; other authors have arrived at other results, however, and this approach should not be construed as the only one which can be employed.

For the case of specular reflection, in Figure 19, maximum reflection occurs in the direction $\theta_1 = \theta_2$, and $\phi_2 = 0$. For this direction $F_3 = R_o$, and equation (20) reduces to

$$\rho_s = \frac{R_o}{A} \iint_S e^{-j\frac{4\pi \cos\theta_1 \zeta(x,y)}{\lambda}} dS \tag{22}$$

Variations in $\zeta(x, y)$ can be classified (1) as fine grained deviations of the surface from a local mean and (2) in terms of the curvature of the mean surface. If the mean of the surface is planar and if $\zeta(x, y)$ is replaced by Δh, where Δh represents the standard deviation of ζ from the planar surface, the mean square value of the coefficient of specular reflection is

$$\left\langle |\rho_s|^2 \right\rangle = \left[\frac{R_o}{A} \iint_S e^{-j\frac{4\pi \cos\theta_1 \Delta h}{\lambda}} dS \right]^2 \tag{23}$$

or this expression reduces to

$$\left\langle |\rho_s|^2 \right\rangle = |R_o|^2 \, e^{-(\Delta\Phi)^2} \tag{24}$$

where

$$\Delta\Phi = \frac{4\pi \sin\gamma \, \Delta h}{\lambda} \quad . \tag{25}$$

The sine of the grazing angle, γ, has replaced the cosine of the angle of incidence, θ_1, in equation (25). The phase excursion, $\Delta\Phi$, is identical to that which was employed in defining the Rayleigh roughness criterion, and $\Delta\Phi$ is a quantitative measure of the roughness of a surface. A curve of $\left\langle |\rho_s|^2 \right\rangle$ plotted as a function of $\Delta\Phi$ is presented in Figure 20. The coefficient of specular reflection is seen to be very low for values of $\Delta\Phi$ greater than $\pi/2$. Scattering is almost entirely diffuse for these conditions.

Another factor must now be used to account for the effect of curvature of the surface because if $\langle \zeta \rangle$ defines a curved surface, the coefficient of specular reflection will be different from that of a planar surface. For this purpose it is convenient to consider reflection in terms of Fresnel zones on the reflecting surface.

Consider the smooth, planar surface region shown in Figure 21, with a transmitting antenna at T and a receiving antenna at R. For this surface, there is

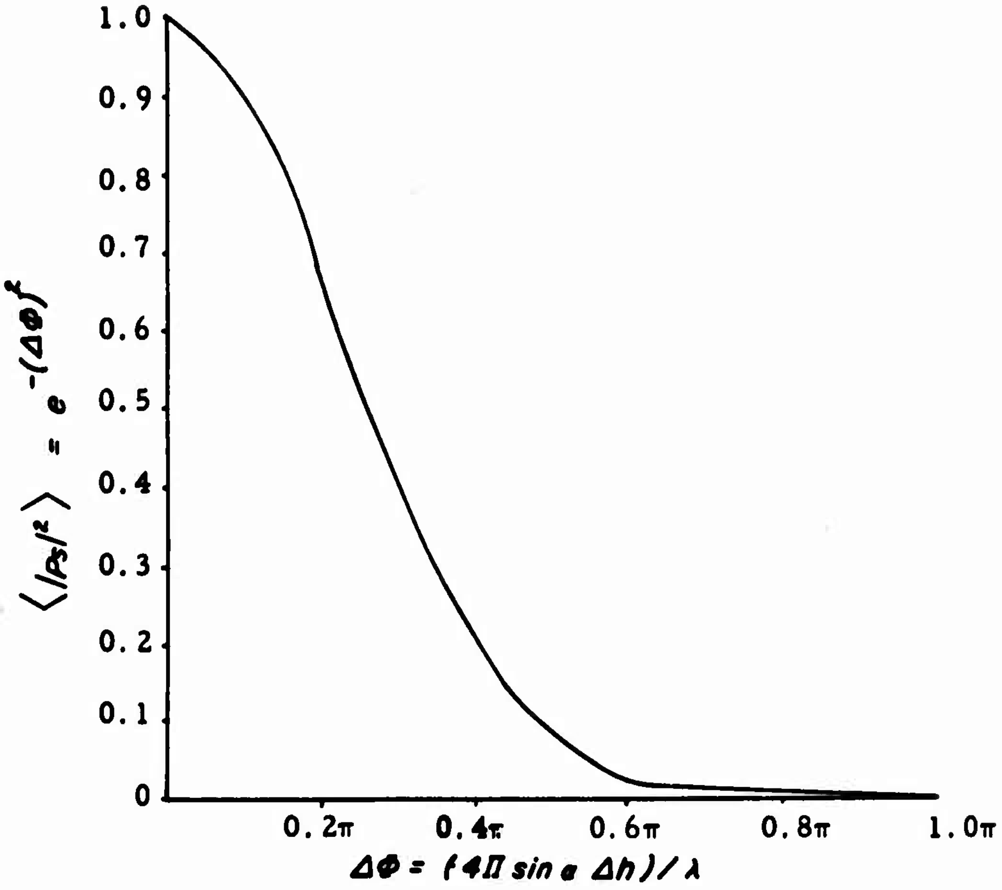

Figure 20. The Mean Square of the Coefficient of Specular Reflection as a Function of $\Delta\Phi$ for R_o Equal Unity

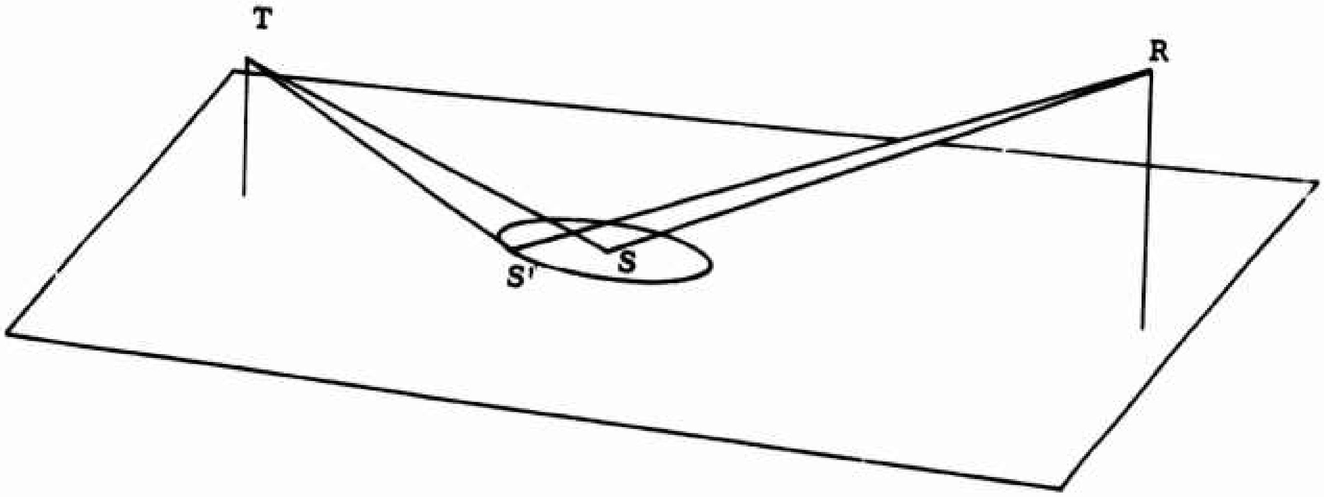

Figure 21. Geometry Employed in Defining Fresnel Zones on a Planar Surface

a point, S, such that the path length, TSR, is the shortest reflected path between T and R. For any other point, S', the path length, TS'R, is greater than TSR; therefore the phase of the wave traveling along the path TS'R will lag behind that of the wave which is reflected at S.

There is a set of points S'' surrounding S for which the phase delays over the paths TS''R are less than π radians. These points define a region known as the first Fesnel zone. Correspondingly, all points S''' for which the phase delay for the path TS'''R exceeds that of TSR by more than $(n-1)\pi$ radians but less than $n\pi$ radians define the nth Fresnel zone.

The Fresnel zones are enclosed by a set of expanding ellipses for the case of a planar surface. Although Fresnel zones are strictly defined for point sources, for practical antenna range geometries Fresnel zones for a point in the receiving aperture can be defined by regarding the transmitting antenna to be a point source located at the center-of-phase of its aperture.

It can be shown that, if the planar surface is lossless, the coefficient of specular reflection will be unity, and reflected energy at the aperture will equal the energy arriving by the direct path TSR. It is therefore convenient to use the smooth, lossless, planar surface as a standard for comparison with other surface shapes. Concave surfaces, for example, may have coefficients of reflection which exceed unity, and, correspondingly, Fresnel zones which are larger than the equivalent zones on a planar surface. On the other hand, the Fresnel zones on a convex surface are always smaller than the corresponding zones on a planar surface, and the coefficient of reflection for a convex surface is always less than unity. Equation (22) can be modified by the inclusion of a divergence factor D so that the coefficient of specular reflection R_s for a curved, rough surface is given by

$$R_s = D\rho_s \tag{26}$$

where ρ_s is the specular coefficient of reflection for a surface which is planar in the mean.

Spizzichino derives a divergence factor D given by[25]

$$D = \left[1 + \frac{2r_1r_2}{a(r_1+r_2)\sin\gamma}\right]^{-\frac{1}{2}} \left[1 + \frac{2r_1r_2}{b(r_1+r_2)}\right]^{-\frac{1}{2}} \tag{27}$$

---

[25] Beckmann and Spizzichino, op. cit., p. 224.

where r_1 and r_2 are the respective distances from the transmitter and receiver to the point of reflection, γ is the grazing angle, and a and b are radii of curvature of intersections of two vertical planes with the surface, one parallel to the direction of propagation and the other perpendicular to the first. D will always be less than unity for convex surfaces but can be greater than unity for concave surfaces.

When the grazing angle is small, the first term of the divergence factor is larger than the second term. Thus, a variation in radius a has greater influence on the reflection coefficient than an equal variation in b. A given curvature in the plane parallel to the direction of propagation is more effective, then, in reducing R_s than one transverse to the direction of propagation. In many cases, where the grazing angle is very low, the second term of equation (27) may be neglected.

3.4 Consideration of Reflections at the USAF Antenna Proving Range, Newport, New York

3.4.1 Summary of the Problem

The problem of reflection from a rough surface is far from being solved exactly for the general case of a random rough surface. The solution presented in the foregoing section is based on several simplifying assumptions, and further simplifications are required if the theory is to be applied to a specific example. A knowledge of the experimental and theoretical work which has been accomplished in this area is quite valuable, however, in attempting to arrive at a reasonable approximation to the precise solution.

The USAF Antenna Proving Range at Newport, New York, consists of two transmission paths identified as transmission paths #1 and #2 in Figure 22. Transmission path #2 is located between a transmitter on Tanner Hill and a receiving station on Irish Hill. The path length is 7520 feet and, at the center of the valley, the clearance from line-of-sight to ground is 470 feet as illustrated in the path profile in Figure 23. The valley between the transmitter and receiver and the crests of each hill are essentially free of heavy vegetation, while the slopes are covered with trees.

If the range design criteria governing path length and aperture sizes, as discussed in Section 3.1, are not violated, the most serious source of error will

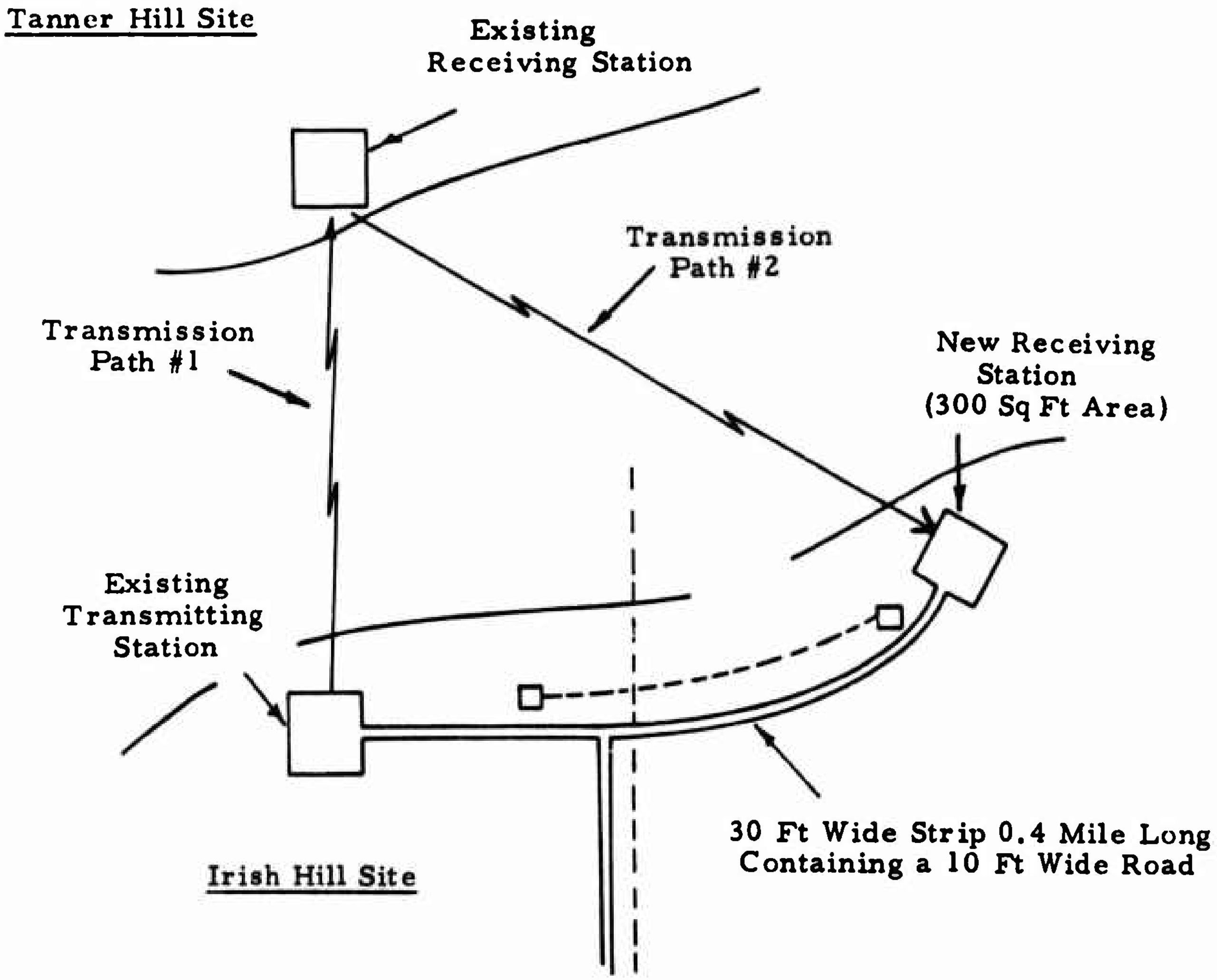

Figure 22. Proposed Layout for the USAF Antenna Proving Range at Newport, New York

probably be from extraneous signals caused by reflections. The two most likely sources of specular reflection are the support towers and buildings and the range surface. The range will be used to test large extremely directive antennas which will exhibit a high degree of discrimination against signals arriving from the rear of the aperture; hence, the most troublesome extraneous signals will probably be those which are reflected by the antenna range surface.

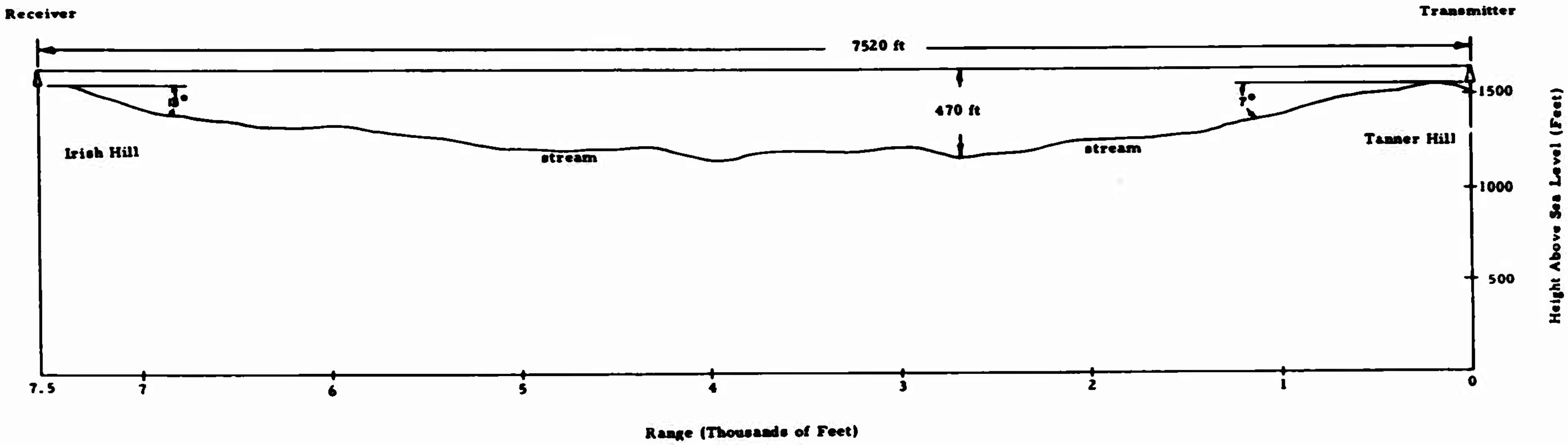

Figure 23. Range Profile of Transmission Path Number 2 at the USAF Antenna Proving Range, Newport, New York

The coefficient of specular reflection is given in equation (26) as

$$R_s = D\rho_s$$

where

$$\left\langle |\rho_s|^2 \right\rangle = |R_o|^2 \, e^{-\left(\frac{4\pi \sin\gamma \, \Delta h}{\lambda}\right)^2} \tag{24}$$

and where

(1) the symbols $\langle \rangle$ represent a mean value,
(2) D is the divergence factor, given by equation (27),
(3) R_o is the coefficient of specular reflection of a smooth, plane earth,
(4) Δh is the standard deviation of the variation in height of the surface,
(5) γ is the grazing angle, and
(6) λ is the wavelength.

In many cases the coefficient of reflection R_o may be very nearly unity; this is particularly true for small grazing angles.[26] Hence, a "worst-case" condition would be

$$|R_o| = 1$$

and

$$\left\langle |\rho_s|^2 \right\rangle = e^{-\left(\frac{4\pi \sin\gamma \, \Delta h}{\lambda}\right)^2} \quad . \tag{28}$$

On this assumption the coefficient of specular reflection from a given specularly reflecting region of the range surface may be evaluated as a function of frequency if the grazing angle and the standard deviation of surface perturbations are known.

3.4.2 Location of the Regions of Possible Specular Reflection

As an aid in locating the specular reflecting regions of the range surface a three-dimensional scale model of the USAF Antenna Proving Range has been constructed from data supplied by RADC in the form of contour maps. The model, built on a scale of 1 inch=160 feet, was used to determine the location

---

[26] Jordan, op. cit., pp. 612-618.

of Fresnel zones in the following manner. Small eyelets were placed in the model at the locations of the transmitting and receiving antennas, and a steel wire was stretched between them. The wire was lengthened until it first touched the surface at some point, locating a center of specular reflection. The wire was then lengthened by 1/16 inch increments and the corresponding contours of constant reflected path length were traced on the surface with a pencil held by a small, sliding loop on the wire. This procedure is illustrated in Figure 24. The contours thus obtained roughly define Fresnel zones on the range surface. At the scale used for this model, consecutive contours represent a difference in path length of 10 feet, which corresponds to 2, 20, and 200 Fresnel zones at 100 Mc, 1 Gc, and 10 Gc, respectively.

The scale model of the antenna range is shown in Figure 25 with the constant path contours plotted on the surface. The receiving antenna is on the left side, and the line of sight between transmitter and receiver is indicated by a black thread. As can be seen from the photograph, there appear to be four major regions from which specular reflection can take place. If these areas are numbered from left to right, number 1 lies at the base of the receiving tower; number 2 lies on the slope of Irish Hill; number 3 lies in the bottom of the valley between the two streams; and number 4 lies at the base of the transmitter. Photographs which have been supplied by RADC indicate that these Fresnel zones fall in areas which are essentially covered with grass or very low vegetation, with the exception of region number 2, which lies on the wooded slope of Irish Hill.

Since all of the regions are nearly directly underneath the line of sight, the approximate grazing angle γ for each can be determined graphically from a profile of the range. The grazing angles thus obtained for regions 1, 2, 3 and 4 are approximately 10, 3.5, 6, and 7 degrees, respectively. These angles are essentially constant over the region of interest surrounding each zone.

The standard deviations of surface irregularities for each zone are estimated by observing the ground covering which appeared to be in existence in the photographs. Regions 1 and 3 are clear except for grass and a value of 3 inches for Δh is considered appropriate. Region 2 lies on a heavily wooded slope, and a value of 10 feet for Δh is used. Region 4 is covered with underbrush and higher grass than regions 1 and 3, and a value of Δh of 1 foot is employeed.

Figure 24. Method Used to Determine the Approximate Location of Fresnel Zones

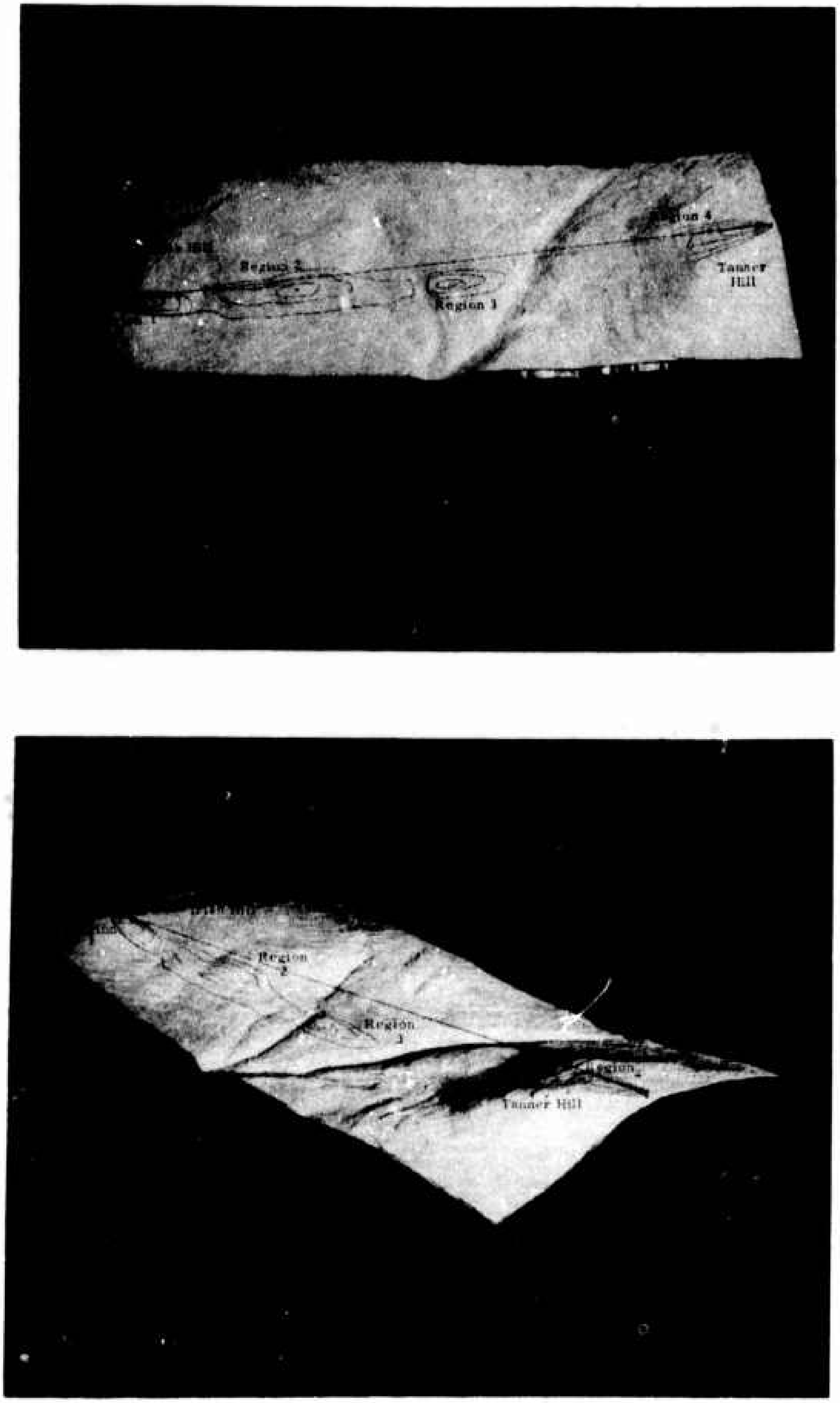

Figure 25. Location of the Possible Centers of Specular Reflection

If the estimated grazing angles and height deviations are used in equation (28), the following values for $\left\langle |\rho_s|^2 \right\rangle$ are obtained:

$$\text{Region 1} - \left\langle |\rho_s|^2 \right\rangle = e^{-\frac{0.028}{\lambda^2}} \tag{29a}$$

$$\text{Region 2} - \left\langle |\rho_s|^2 \right\rangle = e^{-\frac{5.4}{\lambda^2}} \tag{29b}$$

$$\text{Region 3} - \left\langle |\rho_s|^2 \right\rangle = e^{-\frac{0.01}{\lambda^2}} \tag{29c}$$

$$\text{Region 4} - \left\langle |\rho_s|^2 \right\rangle = e^{-\frac{0.22}{\lambda^2}} \tag{29d}$$

where λ is expressed in meters.

Taking the square root of each expression yields the values for ρ_s. The rms coefficients of specular reflection are then

$$R_{S1} = D_1 \, e^{-\frac{0.014}{\lambda^2}} \tag{30a}$$

$$R_{S2} = D_2 \, e^{-\frac{2.7}{\lambda^2}} \tag{30b}$$

$$R_{S3} = D_3 \, e^{-\frac{0.005}{\lambda^2}} \tag{30c}$$

and

$$R_{S4} = D_4 \, e^{-\frac{0.11}{\lambda^2}} \tag{30d}$$

where the numerical subscripts identify the region, and D is the divergence factor due to the local curvature of the surface.

The divergence factors are obtained from equation (27);

$$D = \left[1 + \frac{2r_1 r_2}{a(r_1+r_2)\sin\gamma}\right]^{-\frac{1}{2}} \left[1 + \frac{2r_1 r_2}{b(r_1+r_2)}\right]^{-\frac{1}{2}} \tag{27}$$

where r_1 and r_2 are the distances from the point of reflection to the transmitter and receiver respectively, a and b are the longitudinal and transverse radii of curvature of the surface, and γ is the grazing angle. Since γ is small for all four regions, and since the curvature of the surface is much greater in the longitudinal direction than in the transverse direction, the second term is small in comparison with the first, and the divergence factor is approximated by

$$D = \left[1 + \frac{2r_1r_2}{a(r_1+r_2)\sin\gamma}\right]^{-\frac{1}{2}} \quad . \tag{27a}$$

The range profile in Figure 23 indicates that Tanner Hill drops to a slope of 7 degrees in approximately 1500 feet. If the radius of curvature is considered constant for this region, the geometry is as illustrated in Figure 26. The radius of curvature r is given by

$$r = \frac{1500}{\sin 7^\circ} = 12,000 \text{ feet} \quad . \tag{31}$$

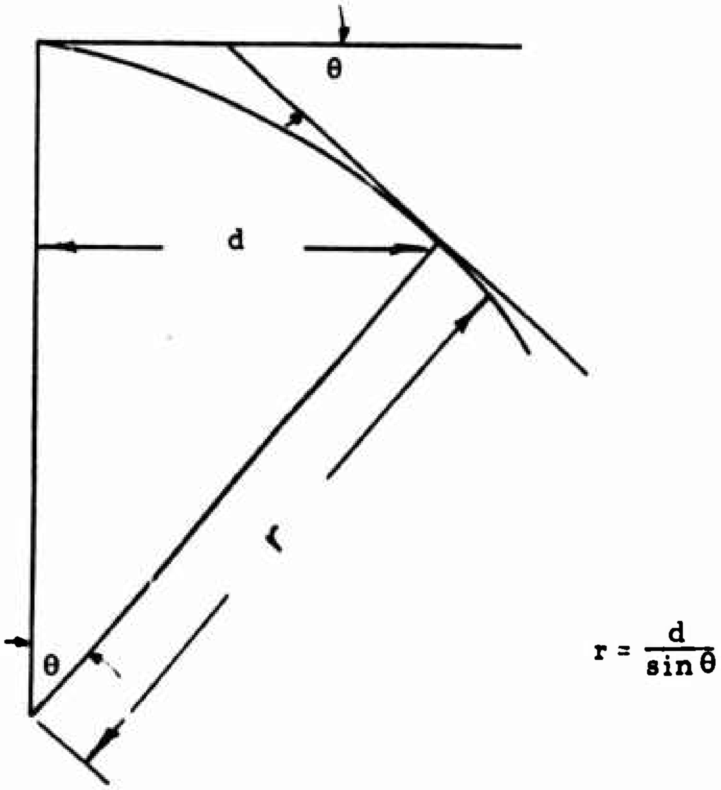

Figure 26. Geometry of Radius of Curvature Calculations (not to scale)

The distances r_1 and r_2 can be approximated by

$$r_1 = 300 \text{ feet}$$

and

$$r_2 = 7250 \text{ feet.}$$

Then

$$D_4 = \left[1 + \frac{2 \times 300 \times 7250}{12000 \times 7550 \times 0.12}\right]^{-\frac{1}{2}} = 0.84 \quad . \tag{32}$$

A similar analysis for the divergence factors of the region near the top of Irish Hill yields

$$D_1 = 0.72 \quad . \tag{33}$$

Regions 2 and 3 are more difficult to evaluate since no direct information is available with which to calculate the curvatures of the surface; these regions appear to be quite flat in comparison with regions 1 and 4, however, and D is estimated to be 0.95 for these areas. This estimate is believed to be conservative, especially in the case of region 3 which may even be slightly concave.

The coefficients of specular reflection for the four regions are:

$$R_{S1} = 0.72\, e^{-\frac{0.014}{\lambda^2}} \tag{34a}$$

$$R_{S2} = 0.95\, e^{-\frac{2.7}{\lambda^2}} \tag{34b}$$

$$R_{S3} = 0.95\, e^{-\frac{0.005}{\lambda^2}} \tag{34c}$$

$$R_{S4} = 0.84\, e^{-\frac{0.11}{\lambda^2}} \tag{34d}$$

These coefficients are plotted as a function of frequency in Figure 27.

The results presented here are based on a unity value for the reflection coefficient R_o. As stated previously, R is often very nearly unity, and this assumption is a "worst-case" condition. The theoretical curves for R_o indicate that for the case of horizontal polarization the reflection coefficient is always

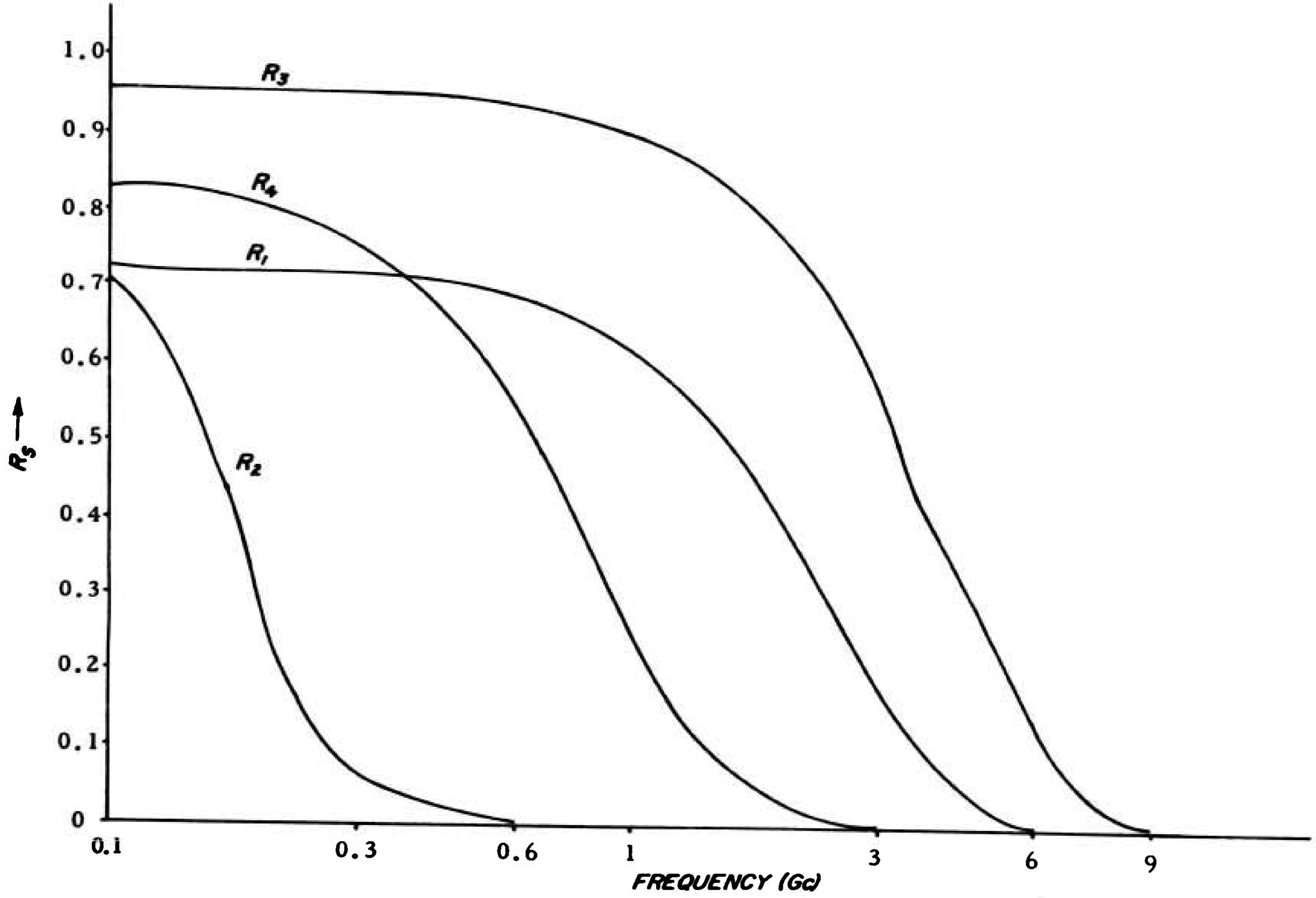

Figure 27. Variation of Coefficients of Specular Reflection with Frequency

near unity. The curve for vertical polarization dips sharply, however, for increasing grazing angle until the Brewster angle is reached, at which point the curve rises again. Curves presented by Jordan[27] show that this minimum occurs for grazing angles of approximately 15-18 degrees for soil of the type found in New York State. The grazing angles for the present at the RADC range vary between 3.5 and 10 degrees, so that R_o falls on the steep slope of the curve, varying between 0.6 and 0.2. Measurement results which have been documented by Kerr[28] and Spizzichino[29] indicate that measured reflection coefficients tend to approximate the theoretical curves closely. For this reason, specular reflection of vertically polarized energy is expected to be 3 to 6 db less than that of horizontal polarization.

3.4.3 Diffuse Scattering

The case of diffuse scattering is more difficult to evaluate theoretically. This type of reflection results from the summation of phasors of random phase radiated from every point on the surface; hence it is not potentially as troublesome as specular reflection, which results from coherent addition of phasors.

The coefficient of diffuse reflection can be approximated by[30]

$$R_d = R_o \rho_d$$

where ρ_d is the diffuse scattering coefficient analogous to ρ_s and R_o is the coefficient of reflection of smooth earth as used in the analysis of specular reflection. Note that the divergence factor D is not included here; investigations and theory indicate that D has very little effect on diffuse reflection, which is, by definition, non-directional.

Results of experiments conducted over various types of terrain for many frequencies exhibit a surprising degree of correlation[31], indicating a diffuse

---

[27] Jordan, op. cit., pp. 612, 613.

[28] Kerr, op. cit., p. 320.

[29] Beckmann and Spizzichino, op. cit., p. 320.

[30] Beckmann and Spizzichino, op. cit., p. 334.

[31] Beckmann and Spizzichino, op. cit., pp. 336, 337.

scattering coefficient which is grouped around a central value of approximately 0.3. Spizzichino postulates that ρ_d has a maximum theoretical value of 0.35, which it approaches asymptotically. The theoretical curve is such that $\rho_d \geq 0.3$ when $\Delta\Phi \geq 0.25\pi$.

The wavelength $\lambda_{0.3}$ for which ρ_d is likely to be as great as 0.3, on the basis of this model, can be determined from equation (25)

$$\frac{4\pi \sin\gamma \, \Delta h}{\lambda} = 0.25\,\pi \tag{35}$$

giving

$$\lambda = 16 \sin\gamma \, \Delta h \; . \tag{36}$$

For shorter wavelengths, lower grazing angles or greater surface roughnesses, ρ_d is likely to increase from this value to values which are no greater than 0.35.

An average value of $\gamma = 6$ degrees is assumed for the RADC antenna range yielding

$$\lambda = 1.7\,\Delta h \; . \tag{37}$$

Diffuse scattering is likely to result primarily from radiation near the ends of the transmission path, i.e., from the tops of the hills. For these areas a value of $\Delta h = 0.1$m may be postulated yielding

$$\lambda_{0.3} = 0.17 \text{ meter} \tag{38}$$

corresonding to a frequency of about 2 Gc.

For frequencies above 2 Gc, the value of ρ_d is likely to be as large as 0.3, while for lower frequencies, ρ_d falls rapidly to a very low value. A unity value for R_o is assumed, as in the case of specular reflection.

3.4.4 Analysis of Possible Errors Caused by Reflections

The measurement error caused by specularly reflected extraneous signal is a function of the phase and amplitude of the signal which is received at the test-antenna terminals. The received extraneous signal is determined by the radiation patterns of the transmitting and receiving antennas as well as the specular reflection coefficient R_s of the surface. The power delivered to the receiving antenna terminals by the extraneous signal, expressed as a fraction of the direct signal is given by

$$\frac{|\bar{E}_r|^2}{|\bar{E}_d|^2} = \frac{G'_1 G'_2}{G_1 G_2} R_s^2 \tag{39}$$

where $\bar{E}_r$ and $\bar{E}_d$ are complex terminal voltages produced by the reflected and direct signals, G'_i and G'_2 are the gains of the transmitting and receiving antennas in the direction of the reflecting surface, G_1 and G_2 are the gains of the antennas in the line of sight direction, and R_s is the reflection coefficient. The antennas are assumed to be polarization matched over the sidelobe structure, i.e., the polarization efficiency factor is taken to be unity. When more than one reflecting surface is present, the extraneous signal level at the antenna terminals is represented by the summation of all reflected signals. The incident signals add as phasors, and the total extraneous signal is given by

$$\bar{E}_t = \sum_{i=1}^{n} \bar{E}_{ri} e^{j\phi_i} = E_t e^{j\phi_t} \tag{40}$$

For this case, equation (39) is rewritten as

$$\left[\frac{E_t}{E_d}\right]^2 = \left[\sum_{i=1}^{n} \frac{G'_{1i} G'_{2i}}{G_{1i} G_{2i}} R_i e^{j\phi_i}\right]^2 . \tag{41}$$

where the factor $e^{j\phi_i}$ accounts for the relative phase of each signal. There are four likely sources of specular reflection on the RADC antenna proving range surface; the factor n is thus taken as 4. The subscript i identifies parameters associated with each of these paths of reflection.

In practice the main beam of the transmitting antenna is nearly always directed toward the receiver so that G_1 is constant for a given antenna and frequency; therefore, the term G'_{1i}/G_1 will be constant for a fixed direction from the transmitter. In order to illustrate the significance of the gain factor underneath the radical of (41), equation (41) will be considered for the case of two isotropic sources. The gain factor becomes unity, and

$$\frac{E_t}{E_d} = \sum_{i=1}^{4} R_i e^{j\phi_i} . \tag{42}$$

The phases of the reflection coefficients will be very nearly the same for each of the reflection zones; the phase factor $e^{j\phi_i}$ on the other hand is a random variable and will allow the summation to take on any value such that

$$0 \leq \left| \frac{E_t}{E_d} \right| \leq R_1 + R_2 + R_3 + R_4 \quad . \tag{43}$$

In the worst case, when all reflections share a common phase, the extraneous signal is a maximum value which is plotted in Figure 28 as a function of frequency. At low frequencies, the reflected signal can be greater than unity. Of course, the total reflected signal will generally be somewhat less than that for the worst case. The mean value which can be shown to be

$$\left\langle \frac{E_t}{E_d} \right\rangle = \sqrt{R_1^2 + R_2^2 + R_3^2 + R_4^2} \quad , \tag{44}$$

is also plotted versus frequency in Figure 28. Note that, for the lower frequencies, E_t is still large relative to E_d.

The gain factor is seen to be important in the suppression of the extraneous signal level at the terminals. This factor is minimized by minimizing the relative gains of the transmitting and receiving antennas in the directions of each of the four zones of specular reflection. Table 1 lists the angles from boresight of the transmitting and receiving antennas to each of these regions. The numbers identifying the regions correspond to those used above. Since the Fresnel zones lie essentially beneath the line of sight, the angles tabulated are measured in the vertical plane parallel to the length of the range. These figures are based on transmitting and receiving tower heights of approximately 40 feet.

Region	Angle From Transmitter	Angle From Receiver
1	0.75 degree	28 degrees
2	3.5 degrees	9 degrees
3	7 degrees	5.5 degrees
4	13 degrees	0.75 degree

Table 1. Angles to Zones of Specular Reflection

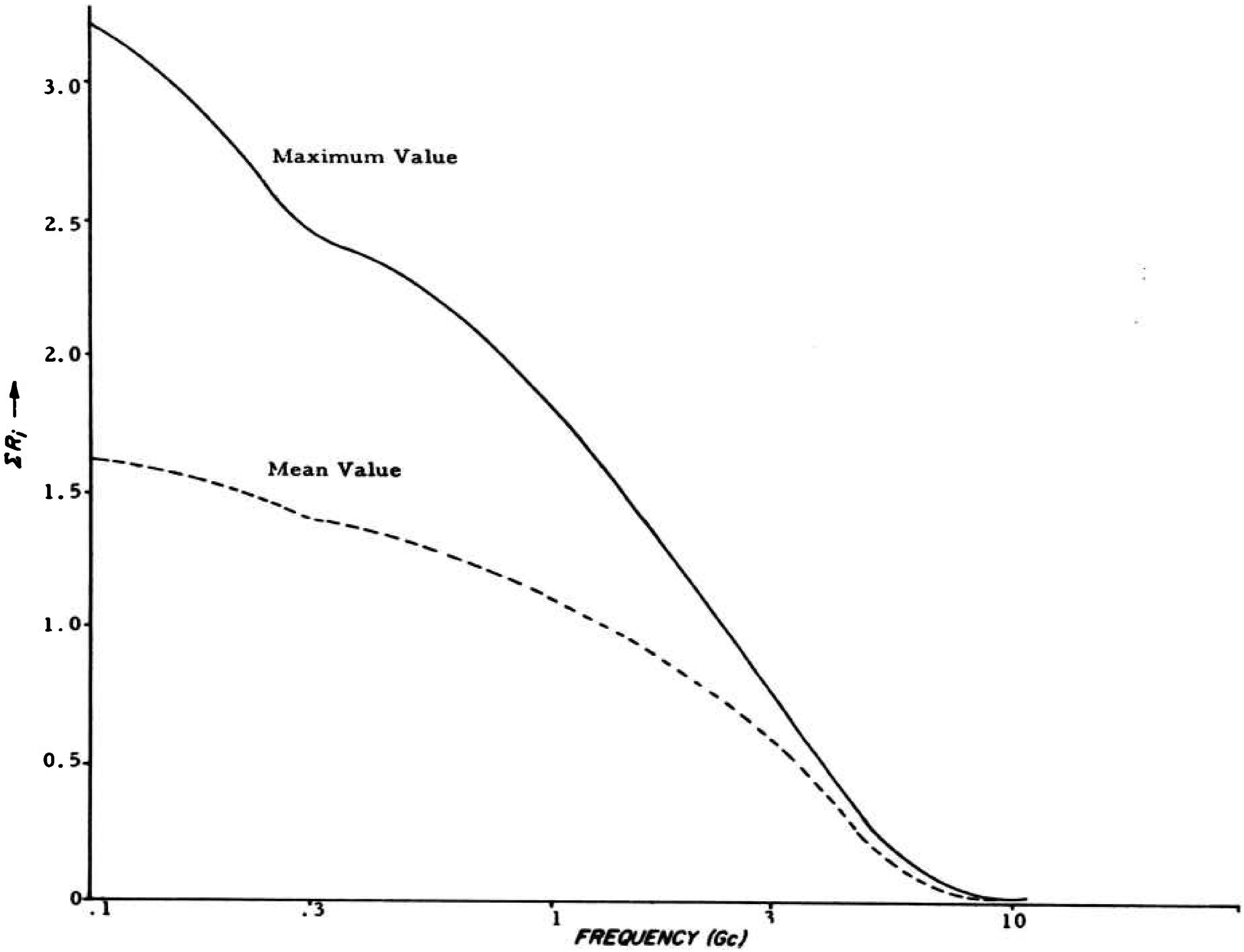

Figure 28. Maximum and Mean Values for the Total Coefficient of Specular Reflection Versus Frequency

Consider the problem of testing a paraboloidal antenna with a diameter d. It is desirable to limit the maximum amplitude taper of the incident wave to 0.25 db over the test aperture. The amplitude variation near the maximum of the main lobe of a typical transmitting antenna can be approximated by

$$A(\theta) = \frac{\sin k\theta}{k\theta} \quad , \tag{45}$$

where θ is the angle measured from boresight and k is a proportionality factor dependent on the beamwidth. The test aperture diameter will subtend an angle ϕ given by

$$\phi \approx \frac{d}{r} \text{ radians} \tag{46}$$

where r is the separation between antennas. In order to assure an amplitude variation of less than 0.25 db over the test aperture, the minimum 3-db beamwidth of the transmitting antenna is found from tables of sin x/x to be

$$\theta_{3\,db} \doteq 3.4\,\theta_{.25\,db} = 3.4\,\frac{d}{r} \text{ radians} \quad . \tag{47}$$

The separation r for transmission path number 2 is 7520 feet. The transmitting beamwidth is thus required to equal or exceed

$$\theta_{3\,db} = \frac{3.4 \times 57.3d}{7520} \doteq 0.02d \text{ degrees} \quad . \tag{48}$$

A 50-foot test aperture would require a minimum transmitted beamwidth of 1 degree. Reference to Table 1 shows that the reflection zone number 1, at the base of the receiving tower is only 0.75 degree below boresight; hence it will be illuminated by energy of the main beam since the width of the main lobe of a typical transmitting antenna is about 2.5 times the 3 db beamwidth. Reflection zone number 1 will be illuminated by the main beam of the transmitter for test apertures larger than 25 or 30 feet. If the transmitter beam is broader than necessary, or if it is directed below the line of sight by even a small amount, the first zone will be illuminated by the main lobe for even smaller apertures.

Reflection zone number 2 will fall outside the main lobe of the transmitted beam if the beamwidth is no greater than 1 degree. In addition, the curves presented in Figure 27 indicate that reflection from this zone will be quite small except for very low frequencies. Zones 3 and 4 will be illuminated by sidelobes of a 1-degree beamwidth antenna, and the energy incident upon these areas will likely be 30 to 40 db down from the peak of the main beam for that case.

Although a 1-degree beamwidth is the broadest transmitted beam which would ever be required for proper illumination of the largest test aperture (50 feet in diameter), represented by the goals of Figure 1, the beam will be somewhat broader at low frequencies due to mechanical limitations. At 200 Mc the 3-db beamwidth of a 50-foot dish would be greater than 7 degrees, and all four zones of possible reflection would be illuminated by the main beam. In addition, the curves of Figure 28 indicate that the reflection coefficients of zones 1, 3 and 4 would be quite large for these frequencies.

The received extraneous signal level is also determined by the receiving antenna directivity. Although reducing the test aperture size allows a narrower transmitter beamwidth and lowers the intensity with which the reflection zones are illuminated, for a fixed frequency, reducing the aperture size reduces the directivity of the receiving antenna and increases the typical value of the G_2'/G_2 portion of the gain factor of equation (41). Lowering the frequency for a fixed test aperture diameter has the same effect. The factor G_2'/G_2 has a considerably greater range of variation than the G_1'/G_1 factor since the main lobe of the receiving antenna is not always directed toward the transmitter. When the sidelobes are directed toward the transmitter, the direct and reflected signals may suffer essentially the same attenuation. If a reflected signal enters through the main lobe of the receiver, the extraneous signal may undergo a gain of 20 to 30 db relative to the direct signal, and the sidelobe measurements will likely be greatly in error; thus it is important that the main beam not be directed toward the range surface during the course of investigating the sidelobes.

To summarize what has been said, the error signal at the terminals of the test antenna will be determined chiefly by two factors, frequency and the size of the test antenna. The effects of these parameters are as follows:

(1) A large test antenna requires a broad transmitted beam, which increases the illumination of reflecting zones.

(2) Decreasing frequency results in (a) less directive transmitting

and receiving radiation patterns for given size antennas with the attendant increase in illumination of reflecting zones, and (b) increasing coefficients of specular reflection.

In the following paragraphs two hypothetical examples are presented as illustrations of the application of the foregoing analyses to specific measurement problems.

Example 1

A 50-foot diameter paraboloidal antenna is to be tested at a frequency of 200 megacycles. The 50-foot test aperture will require that the beamwidth of the transmitting antenna be 1 degree, minimum (see equation 48). This beamwidth would require a transmitting antenna diameter of about 350 feet, which is impracticable. Let us assume that the largest transmitting dish available is 30 feet in diameter. The 3-db beamwidth of this antenna is given approximately by

$$\theta_{3\,db} = \frac{70\,\lambda}{d} = 12 \text{ degrees} \quad . \tag{49}$$

Typically, the beamwidth between the first nulls will be about 2.5 times the three-db beamwidth, or about 30 degrees.

Figure 29 is a sketch of the amplitude distribution of a typical paraboloidal reflector with the abscissa graduated in units of the 3-db half-beamwidth. The sidelobe region is represented by an envelope of typical sidelobe maxima for a paraboloid. The angles from the line-of-sight to the reflection zones are

Zone 1	0.75 degree	(50a)
Zone 2	3.5 degrees	(50b)
Zone 3	7.0 degrees	(50c)
Zone 4	13.0 degrees	(50d)

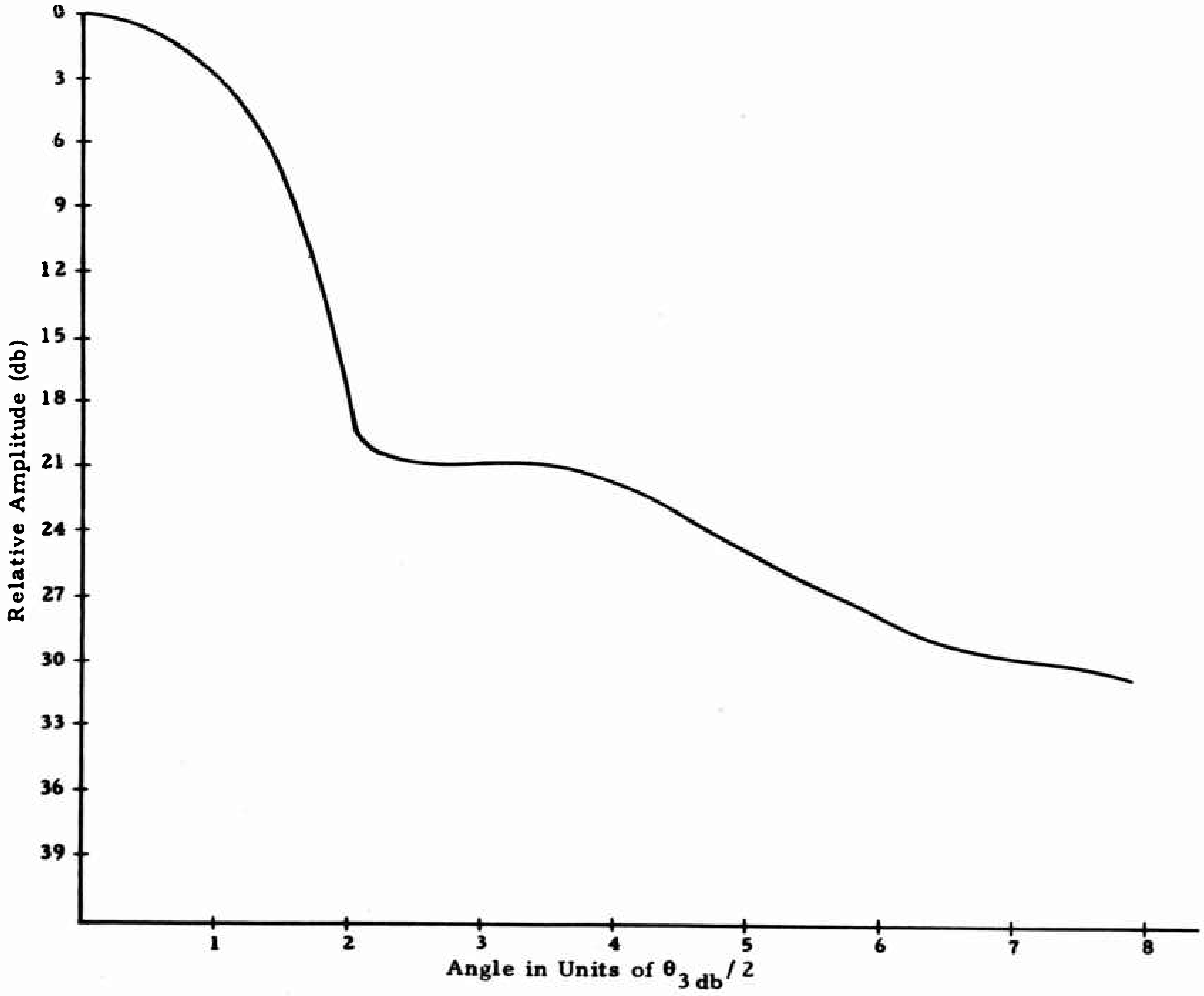

Figure 29. Envelope of the Sidelobes of a Typical Paraboloidal Antenna for Off-Axis Angles in the Region of the Main Lobe

The values G'_1/G_1 are taken from Figure 29 for these angles to be

Zone	G'_1/G_1	Power Ratio
1	-0.10db	0.98
2	-1.0 db	0.795
3	- 4 db	0.398
4	-20 db	0.01

The reflection coefficients for the zones are taken from the Figure 27 to be

$$R_1 = 0.72 \tag{51a}$$
$$R_2 = 0.28 \tag{51b}$$
$$R_3 = 0.95 \tag{51c}$$
$$R_4 = 0.8 \tag{51d}$$

The case of sidelobe measurement will be investigated, in which both the direct and reflected signals enter the receiving antenna through the sidelobes. The factor G'_2/G_2 can vary widely but will be approximated by unity. The mean value of the ratio of extraneous to direct signal is given by

$$\left\langle \left| \frac{E_t}{E_d} \right| \right\rangle = \left[\sum_{i=1}^{4} \frac{G_{1i}}{G_1} |R_i|^2 \right]^{\frac{1}{2}} \tag{52}$$

so that

$$\left\langle \left| \frac{E_t}{E_d} \right| \right\rangle = \sum_{i=1}^{4} \frac{G_{1i}}{G_1} |R_i|^2 \tag{53}$$

$$\left\langle \left| \frac{E_t}{E_d} \right| \right\rangle^2 = 0.98 \times 0.72^2 + 0.80 \times 0.28^2 + 0.90 \times 0.95^2 + 0.01 \times 0.80^2 \tag{54}$$

$$\left\langle \left| \frac{E_t}{E_d} \right| \right\rangle^2 = 0.94 \tag{55}$$

$$20 \log \left\langle \left| \frac{E_t}{E_d} \right| \right\rangle = -0.3 \quad \text{db.} \tag{56}$$

The average value of reflected signal should be very nearly equal to the direct signal. Assuming that the reflected signal is equal to the direct signal errors in measured sidelobe levels can be from +6 db to $-\infty$ db.

Example 2

A 20-foot parabola is to be tested at 10 Gc. The minimum acceptable transmitted beamwidth is

$$\theta_{3\,db} = 0.02 \times 20 = 0.4 \text{ degree} . \tag{57}$$

The maximum allowable diameter for the transmitting antenna is about 17 feet. If such an antenna is employed, the beamwidth between first nulls will be about 1.0 degree, so that the surface will be illuminated almost entirely by the sidelobes of the transmitting antenna.

The coefficients of specular reflection will be virtually zero at this frequency, as shown in Figure 27. The major portion of reflected energy will be diffusely scattered energy. At 10 Gc, the coefficient of diffuse scattering is likely to be very near its theoretical peak value of 0.35, say 0.3. The strength of the extraneous signal at the aperture will be

$$\left| \frac{E_t}{E_d} \right| = \int_s \sqrt{\frac{G_1' G_2'}{G_1 G_2}} \; R_d \, dS \tag{58}$$

where G_1, G_1', G_2, G_2', and R_d are all complex functions over the scattering surface S. Equation (58) may be simplified by assuming an average value, G_{AV}, for the gain function under the radical. G_1' will vary over the surface, but, since the surface is illuminated by sidelobes rather than the main beam, a conservative estimate of -25 db (power ratio = 0.003) for G_1'/G_1 is satisfactory for an average value. The G_2'/G_2 factor is again taken to be unity for the case of sidelobe measurement. The extraneous signal level is

$$\left|\frac{E_t}{E_d}\right| = \sqrt{0.003} \times 0.3 \tag{59}$$

or

$$20 \log \left|\frac{E_t}{E_d}\right| = -35 \text{ db} . \tag{60}$$

This extraneous signal level will cause negligible errors for most measurement requirements.

4. ANTENNA POSITIONING

4.1 Introduction

The current study of techniques and problems related to antenna positioning and angle measurement is a continuation of an analysis which was presented in Section III of the Final Report under Contract No. AF 30(602)-2737.

The specific requirements for equipment to position antennas during testing is dictated to a large extent by the individual requirements of the measurement problem. However, when a high order of angular accuracy is to be attained, careful attention to the coordinate system and positioning system is required. Excessive errors can be introduced in the measurements if the coordinate system of the antenna is not properly aligned with the coordinate system of the antenna range. Additional errors are caused by misalignment of the mechanical axes of the positioning equipment.

The typical antenna test range utilizes a multi-axis positioner to rotate or position an antenna relative to a stationary signal-source antenna. The direction of the signal source relative to the antenna under test is described in terms of angles ϕ and θ of the antenna's spherical coordinate system.

Angle measurement errors from a number of sources must be considered in determining the accuracy of an antenna test range, however the error sources can generally be included in one of the following classifications:

(1) Shaft Position Errors
(2) Positioner or Antenna Deflection Errors
(3) Positioner Axis-Alignment and Coordinate-System-Alignment Errors

Additional direction errors caused by RF phase and amplitude variations over the test aperture, reflections, and parallax are discussed in Section 3 and Section 5.

Shaft-position errors and errors caused by deflection of the positioner or the antenna were analyzed at some length in the previous study.[32] Additional information on these subjects is given in paragraph 4.6 of the present report.

---

[32] FR I-1, Section 3, pp. 44-61.

This section of the study is directed to errors related to positioner axis alignment and coordinate system alignment. Brief introductory discussions are given describing basic coordinate systems and antenna test positioners.

4.2 Coordinate Systems

The radiation pattern of an antenna is defined in terms of the field over a sphere which is centered on the antenna under test. Figure 30 shows the standard spherical coordinate system which is employed for virtually all antenna pattern measurements. This coordinate system may be oriented with respect to the antenna in any manner that is most convenient to the antenna under consideration; the particular orientation usually is determined by the requirements of the using system.

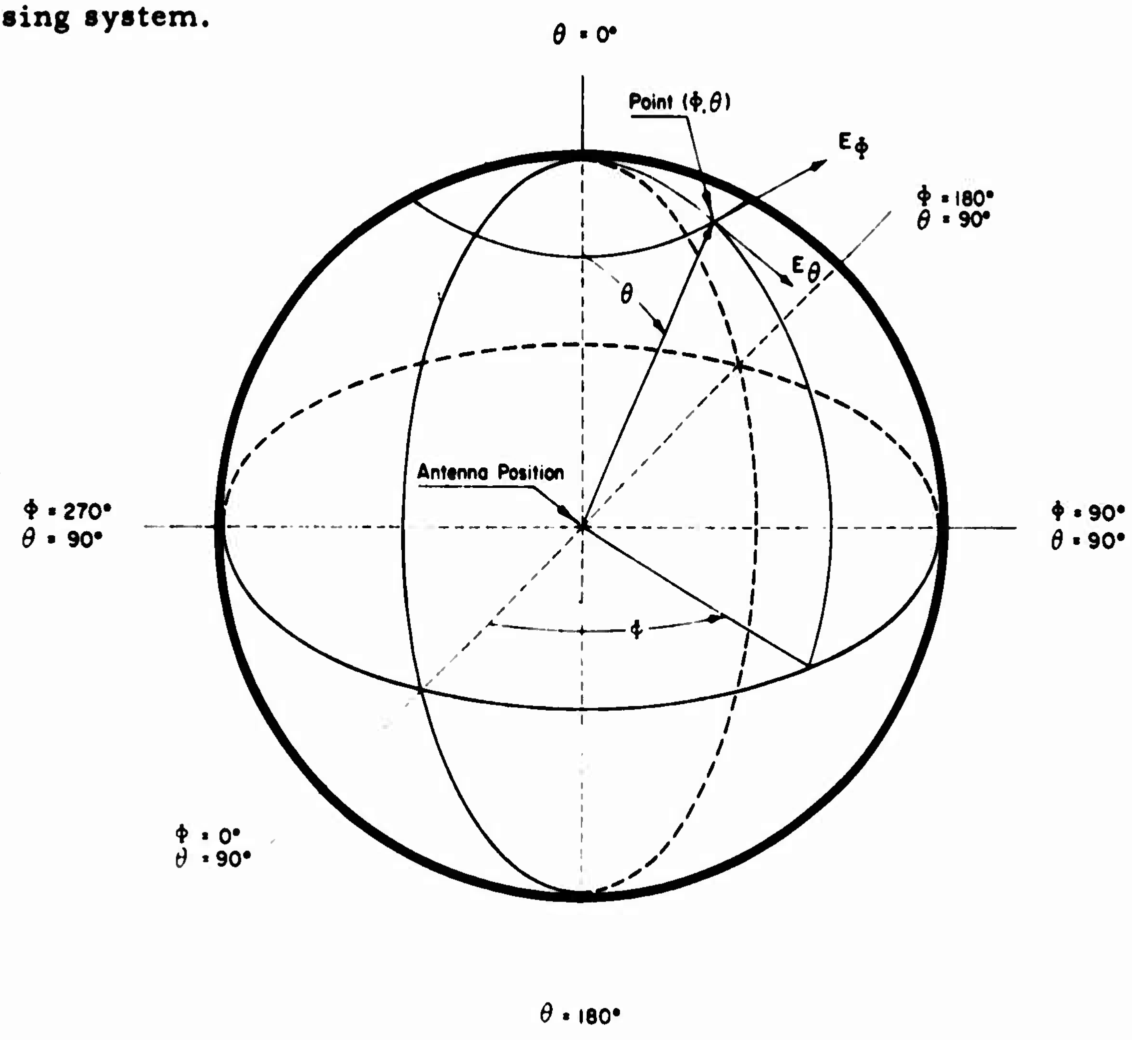

Figure 30. Standard Antenna Coordinate System

For some applications it is desirable to define the coordinate system with respect to a reference other than the radiation pattern. Fixed, ground-based antennas are often described by coordinate systems that are fixed in relation to the earth's surface, usually with the polar axis vertical as defined by local gravity. The special purpose coordinate system shown in Figure 31 has been defined by the Inter-Range Instrumentation Group (IRIG)[33] for use with antennas which are mounted o⁻. aircraft or missile-type vehicles.

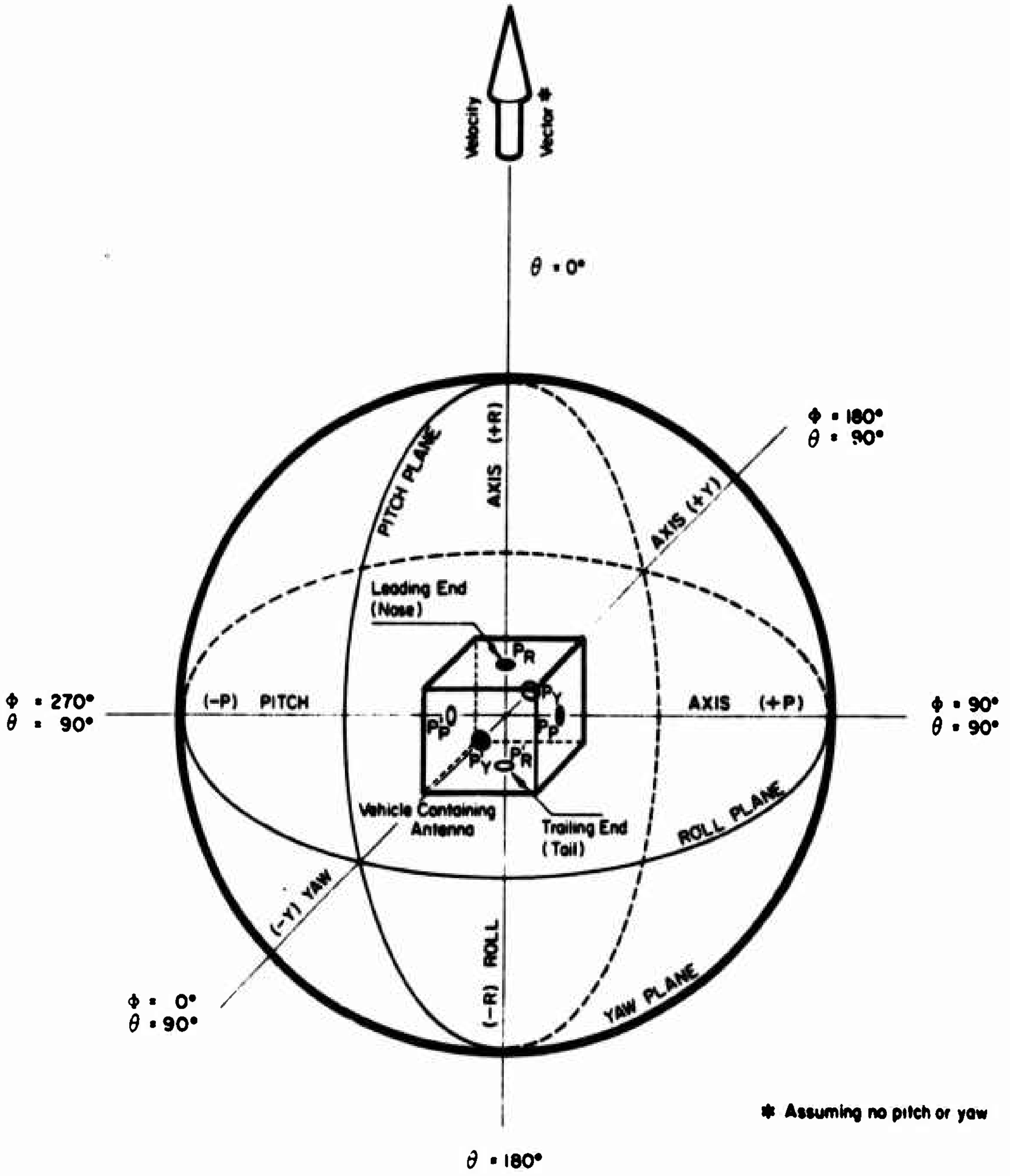

Figure 31. IRIG Consolidated Vehicle and Antenna Coordinate System

---

[33] <u>IRIG Standard Coordinate System and Data Format for Antenna Patterns</u>, Inter-Range Instrumentation Group, IRIG Document No. 102-61, AD 266697, September 1961, Chapter IV.

4.3 Antenna Test Positioners

The discussion which follows relates to coordinates for conventional antenna test ranges, in which the line of sight between a source antenna and an antenna under test remains fixed in direction (usually horizontal or nearly so) while the antenna under test is oriented to simulate movement of the line of sight.

To permit making antenna measurements as functions of ϕ and θ it is necessary for the antenna positioner to have two axes of rotation which are orthogonal. Two positioner configurations, commonly referred to as azimuth-over-elevation and elevation-over-azimuth, are employed for this purpose. Both accomplish the same function but differ in the physical orientation of the coordinate system and in the practical limits of rotation in ϕ and θ. In addition to the two axes of the basic configurations, one or more axes are often employed to provide versatility in making antenna measurements. These configurations are discussed briefly.

4.3.1 Basic Positioner Configurations

The two basic antenna-pattern-range test-positioner configurations and their related coordinate systems are shown in Figure 32 and 33. In both configurations, the antenna is rigidly oriented in the coordinate system XYZ and rigidly fixed to the positioner turntable. Thus the antenna and its coordinate system move with the positioner turntable.

To permit direct measurements in ϕ and θ it is necessary that one of the axes of the positioner be oriented perpendicular to the line of propagation OT between the transmitting antenna, which is located at T, and the antenna under test, which is located at the origin.* The axis OA is oriented perpendicular to OT in both configurations. In Figure 32, axis OA is horizontal and is defined by the elevation axis of the azimuth-over-elevation positioner. In Figure 33, axis OA is vertical, assuming OT is horizontal. It is defined by the azimuth axis of the elevation-over-azimuth positioner.

Comparison of Figures 32 and 33 shows that in the azimuth-over-elevation range, orientation in ϕ is accomplished by rotation about the azimuth axis and

---

*OT will be assumed large compared with the dimensions of the positioner and the antenna under test so that parallax can be neglected. A discussion of parallax is given in FR-I and in Section 5.

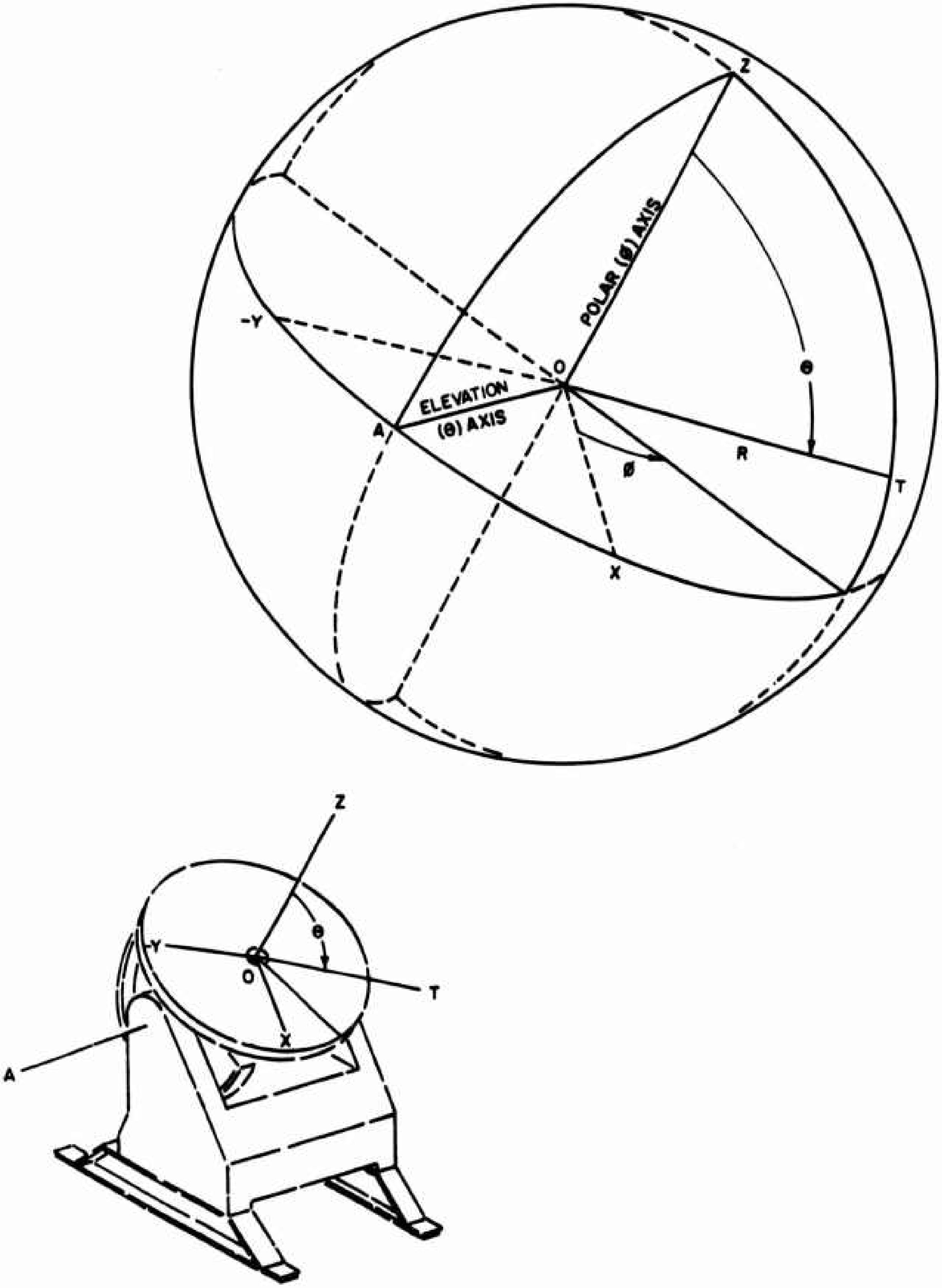

Figure 32. Coordinate System Defined by Azimuth-Over-Elevation Positioner

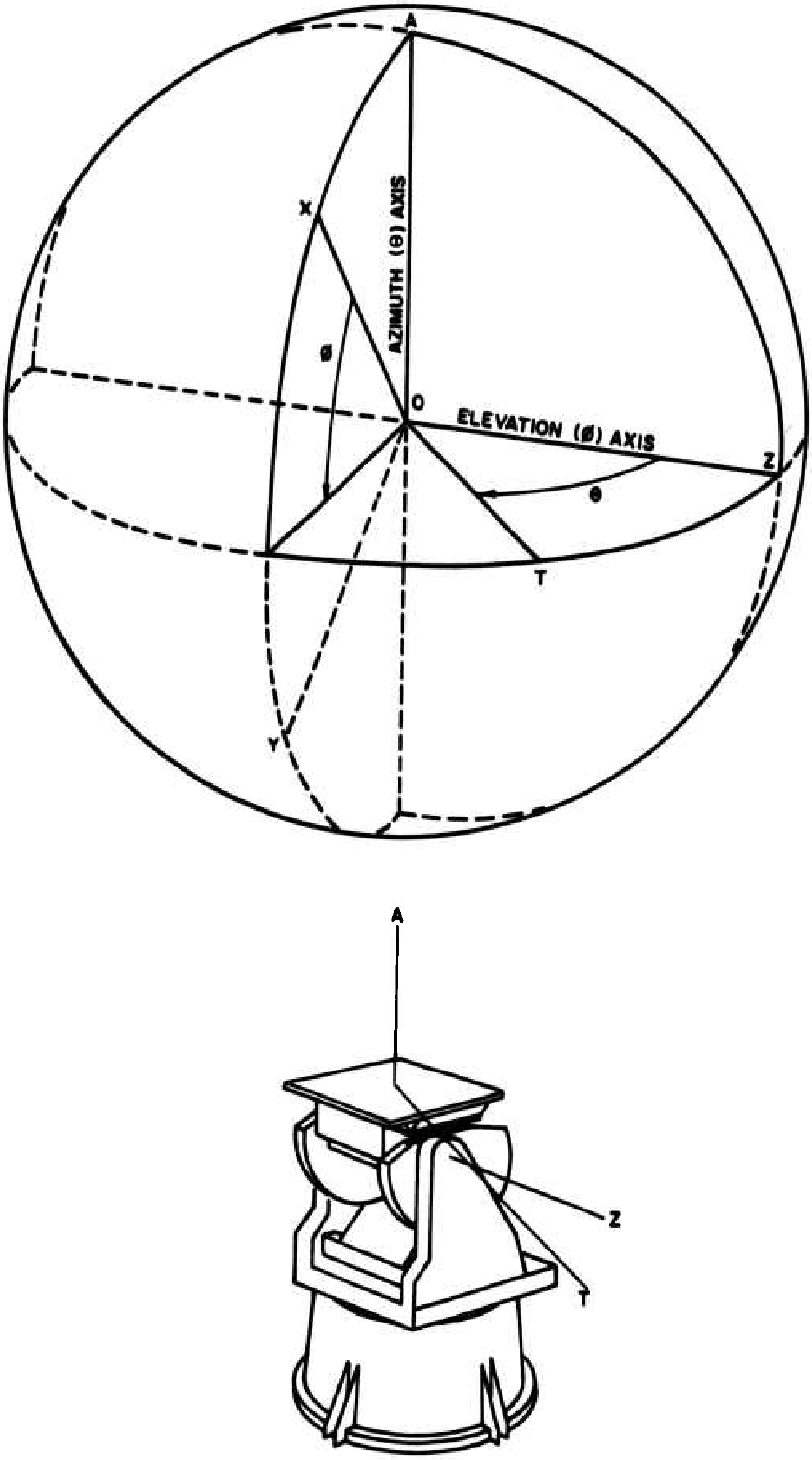

Figure 33. Coordinate System Defined by Elevation-Over-Azimuth Positioner

orientation in θ by rotation about the elevation axis. In the elevation-over-azimuth range the reverse occurs: orientation in ϕ is accomplished by rotation about the elevation axis, while orientation in θ is accomplished by rotation about the azimuth axis. To avoid confusion it is desirable to describe an axis by the rotation it produces in a particular test configuration rather than by its physical orientation; e.g., θ-axis rather than azimuth- or elevation-axis.

Consideration of the positioners shown in Figures 32 and 33 shows that, other than the orientation of the coordinate system, the major practical difference in the two configurations is in the relative coverage of the sphere which is afforded. For example the azimuth-over-elevation configuration provides coverage of 360 degrees in ϕ, but incomplete coverage in θ because of the interference of the side-members which support the elevation shaft. The elevation-over-azimuth configuration gives 360 degrees of rotation in θ, but limited coverage in ϕ for the same reason. Since θ is defined for the interval of 0 to 180 degrees, rotation through 360 degrees in θ combined with limited coverage in ϕ provides coverage over two diametrically opposite sectors of the sphere.

4.3.2 The Model Tower

In many cases it is necessary to isolate the test antenna from nearby sources of reflection. This is particularly true of model-antenna measurements which are concerned with antennas of low directivity. This requirement leads to the use of the model-tower configuration. A model tower normally consists of a dielectric mast with a rotary "head", mounted on an azimuth turntable as illustrated in Figure 34. The coordinate system used with a model tower is the vertical θ-axis system (elevation-over-azimuth) and is identical to that illustrated in Figure 33 except that complete, rather than partial, coverage in ϕ is provided.

4.3.3 Multi-Axis Positioners

In addition to the two basic positioner axes described above, it is usually found desirable to have one or more additional axes. Figure 35 is a simple sketch of a four-axis positioner. This positioner arrangement consists of an azimuth-over-elevation positioner mounted over a second azimuth axis, with the complete positioner mounted on a "tilt-axis" which has a travel of a few degrees.

The positioner can be employed as an elevation-over-azimuth (vertical θ-axis)

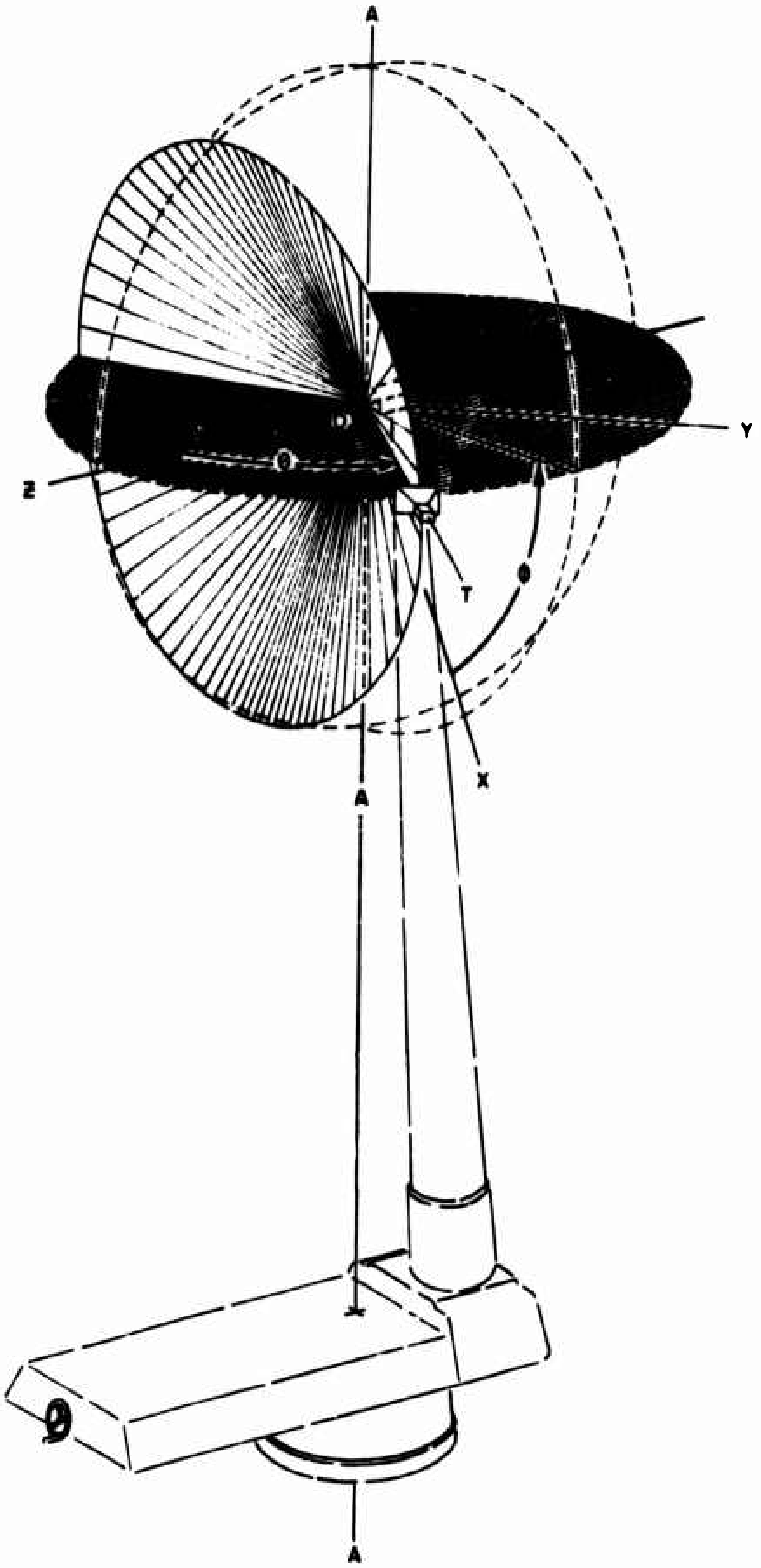

Figure 34. Model Tower and Associated Coordinate System

positioner using the lower-azimuth and elevation axes as shown in Figure 33. In this case the upper azimuth axis serves as a polarization axis. The tilt axis serves to orient the axis OA (the θ-axis) of Figure 33 normal to the line OT. In the sketch the source antenna is shown in two different locations, requiring different adjustments of the tilt axis.

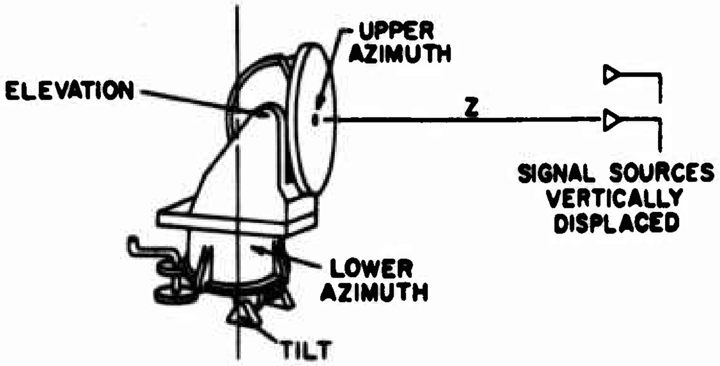

Figure 35. Three-Axis Antenna Positioner with Tilt Adjustment

Alternatively the positioner can be employed in the model-tower mode. The upper azimuth axis serves as the horizontal ϕ-axis to give 360-degree rotation in ϕ. The lower azimuth axis serves as the θ-axis. The elevation axis is adjusted to make the ϕ and θ axes orthogonal and thereafter remains fixed; thus it does not serve as one of the axes defining the coordinate system. The tilt axis is employed as in the previous paragraph.

Finally, the positioner can be employed as an azimuth-over-elevation positioner to define the coordinate system shown in Figure 32. In this case the lower azimuth axis is used (1) to orient the elevation axis (axis OA of Figure 32) perpendicular to OT, and (2) to increase the θ-coverage of the sphere provided by the azimuth-over-elevation positioner configuration. This latter is accomplished by changing the orientation of the lower-azimuth axis through 180 degrees, such that OA is reversed in direction relative to OT.

4.3.4 Antenna Pattern Range Coordinates in Terms of Euler Angles

The relative orientation between two orthogonal, three-space coordinate systems is commonly described in terms of three Euler angles, which are usually designated α, β, and γ; the Euler angles are defined and derived in Appendix A. Definition of the antenna range coordinate systems of Figures 32 and 33 was made in the previous section simply with reference to two axes, OA and OT. Reference to Figure 36 shows that these two axes, with a third orthogonal axis $O\bar{Z}$, define an earth-fixed coordinate system. We will designate this system $\bar{X}\bar{Y}\bar{Z}$, where $O\bar{X}$ is identical with OT and $O\bar{Y}$ is identical with OA. The angles (ϕ, θ) describing the orientation of OT in the XYZ coordinate system (defined by the antenna under test in its position on the antenna positioner, as shown in Figure 36) are described in terms of the relative orientations of the XYZ and $\bar{X}\bar{Y}\bar{Z}$ coordinate systems.

Consider the equations

$$\theta = \cos^{-1}\left[\cos\bar{\theta}\cos\beta + \sin\bar{\theta}\sin\beta\cos(\bar{\phi}-\alpha)\right] \qquad (71)$$

$$\phi = \tan^{-1}\left[\frac{\sin\bar{\theta}\sin(\bar{\phi}-\alpha)}{\sin\bar{\theta}\cos\beta\cos(\bar{\phi}-\alpha) - \cos\bar{\theta}\sin\beta}\right] - \gamma \qquad (78)$$

which are derived in Appendix A. Inspection of Figure 36 shows that the line OT $(O\bar{X})$ is in the direction $(\bar{\phi} = 0,\ \bar{\theta} = 90°)$ of the $\bar{X}\bar{Y}\bar{Z}$ coordinate system and that $\alpha = 0$, since X'' is coincident with $\bar{X}$. Substituting these values in equations (71) and (78) gives the corresponding values of ϕ, θ:

$$\theta = \cos^{-1}[\sin\beta]$$

or

$$\theta = \beta - 90° \qquad (61)$$

and

$$\phi = -\gamma \quad . \qquad (62)$$

In the following section the Euler angle approach is employed in analyzing errors which occur from misalignment in antenna measurement systems.

4.4 Angle Measurement Errors Caused by Misalignment

If the antenna positioner and antenna range being considered were geometrically perfect, the elevation axis OA would be exactly normal to the azimuth axis OZ,

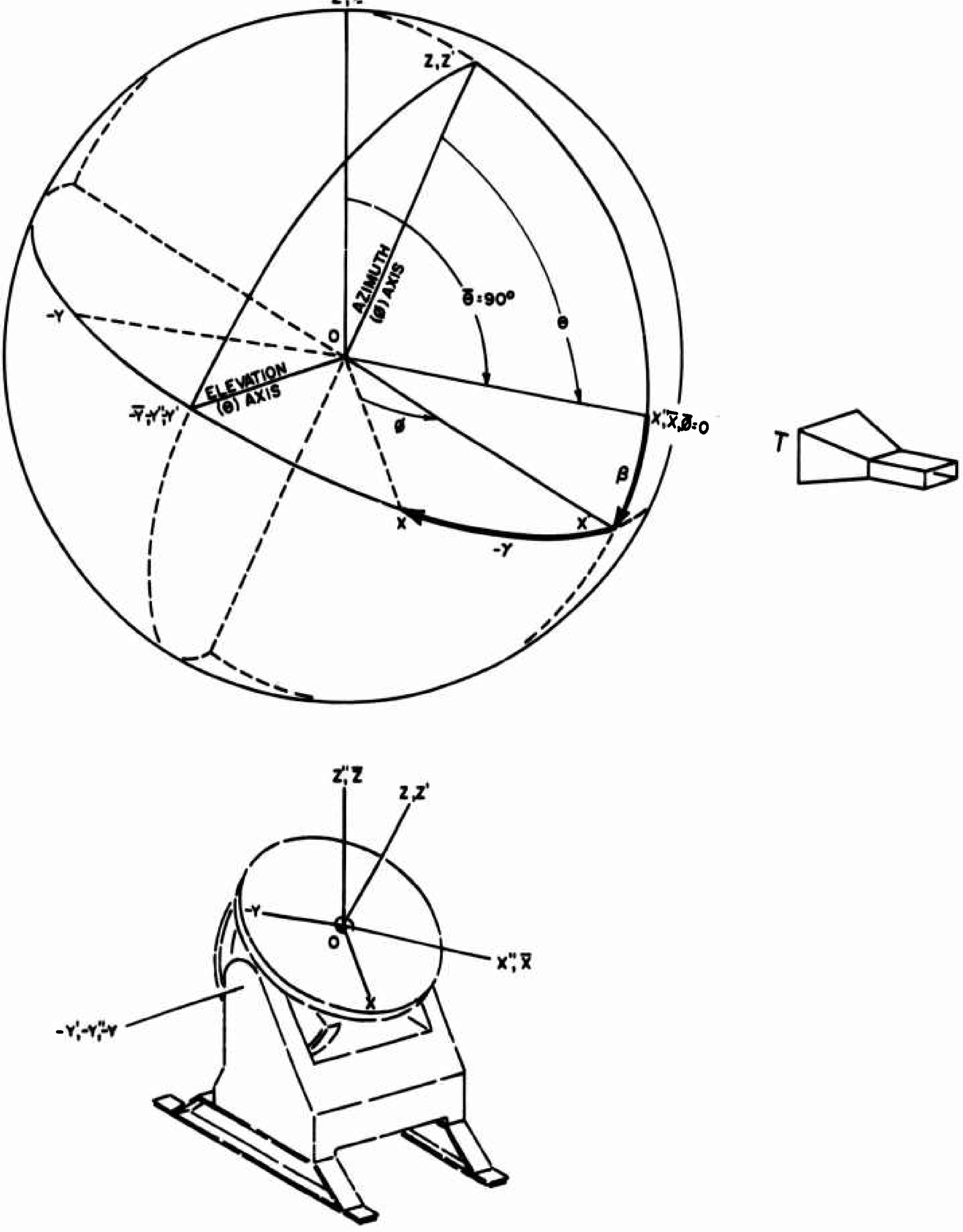

Figure 36. Coordinate System Defined by Azimuth-Over-Elevation Positioner

and the direction line OT from the positioner to the signal source would be exactly normal to OA. The geometrically perfect range system would also have an antenna installed on the turntable so that the coordinate system of the antenna would exactly coincide with the coordinate system of the positioner.

An actual antenna range consists of physical components that may approach the above requirements, but geometric and mechanical errors will always exist. Every antenna measurement system will have three separate geometric errors, which can be identified and described as follows:

(1) Coordinate axis alignment error--Improper alignment of the antenna coordinate system with that of the antenna positioner.

(2) Orthogonality error--Non-orthogonality of the two motion axes of the antenna positioner.

(3) Collimation error--Non-orthogonality of the θ-axis (OA) with the direction OT to the signal source.

The analysis in this section will not present arguments relating to the interdependence of one geometric error upon the others; an analysis of the combined effect of simultaneous errors of the three types is beyond the scope of the present study. For most measurement applications sufficient accuracy will be achieved by calculating the three geometric-error effects separately, and the following calculations will treat them as if they were independent functions.

4.4.1 Coordinate Axis Alignment Error

In order to calculate the errors that are caused by coordinate axis misalignment it is convenient to stipulate that the positioner and range be mechanically perfect in all other respects. That is, it will be assumed that the two motion axes are exactly orthogonal and that the direction to the source antenna is exactly orthogonal to the elevation axis.

Examination of Figure 32 and the analysis of Section 4.3 shows that the polar axis of the antenna coordinate system is to be coincident with the ϕ axis of the positioner. Since the antenna coordinate system is defined with respect to the antenna or its radiation pattern while the azimuth axis is mechanically related to the positioner, some misalignment between the two will always exist in practice. The misalignment can be described and the errors analyzed by the use of Euler angles.

Figure 37 illustrates an antenna range installation in which an antenna coordinate system (XYZ) is positioned and fixed to a positioner turntable such that a misalignment error exists. The direction ϕ, θ is the direction to the source transmitter in the antenna coordinate system (XYZ).

The polar (ϕ) axis of rotation is $O\bar{Z}$ of the positioner turntable coordinate system $\bar{X}\,\bar{Y}\,\bar{Z}$, and the direction $\bar{\phi}, \bar{\theta}$ is the direction of the source transmitter in the positioner coordinate system.

The antenna coordinate system XYZ is misaligned from coordinate system $\bar{X}\,\bar{Y}\,\bar{Z}$ by the Euler angles α, β, and γ.*

In the typical antenna measurements situation the antenna radiation characteristics are required as a function of ϕ, θ. However, the antenna range equipment (positioner, position indicators, recorder) will measure the radiation characteristics as functions of $\bar{\phi}, \bar{\theta}$.

Given the Euler angles α, β, and γ and the direction $\bar{\phi}, \bar{\theta}$, the direction ϕ, θ may be calculated by equations (71) and (78) of Appendix A.

$$\phi = \tan^{-1}\left[\frac{\sin\bar{\theta}\,\sin(\bar{\phi}-\alpha)}{\sin\bar{\theta}\,\cos\beta\,\cos(\bar{\phi}-\alpha) - \cos\bar{\theta}\,\sin\beta}\right] - \gamma \qquad (78)$$

$$\theta = \cos^{-1}\left[\cos\bar{\theta}\,\cos\beta + \sin\bar{\theta}\,\sin\beta\,\cos(\bar{\phi}-\alpha)\right] \qquad (71)$$

4.4.2 Orthogonality

A positioner with an orthogonality error is diagrammed in Figure 38. For this case it is stipulated that all other characteristics of the geometry of the system are perfect. The coordinate system of the antenna coincides perfectly with the positioner coordinate system, and the direction to the source transmitter is exactly normal to the mechanical $\bar{\theta}$-axis, which will be designated OA'. The polar ($\bar{\phi}$)-axis of the antenna positioner is OZ. The mechanical $\bar{\theta}$-axis OA', which should be coincident with OA, is displaced by an angle δ from the XY plane.

---

*The specific Euler angles α, β, and γ employed in this analysis should not be confused with those of equations (61) and (62), describing positioner axis rotations in the theoretically perfect antenna test range.

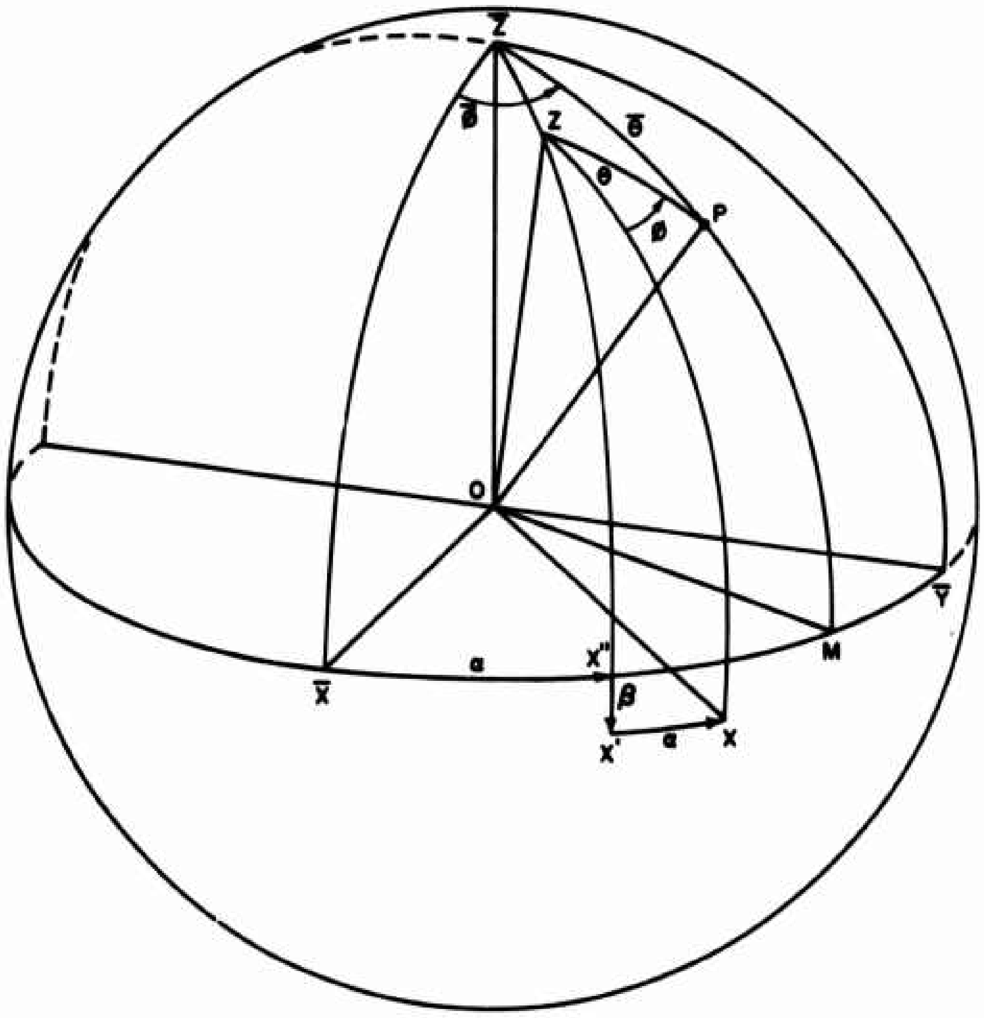

Figure 37. A Direction Described in Two Coordinate Systems

If the geometry were perfect, the antenna coordinate system XYZ could be rotated about OA so that the direction OT to the source transmitter would be in the plane OMZ. However, due to the orthogonality error, rotation of the elevation axis will position OT in the plane OMZ'.

The angles or directions which will be indicated by the instrumentation equipment are $\bar{\phi}, \bar{\theta}$, where $\bar{\phi}$ is the rotation of the positioner polar ($\bar{\phi}$) axis and $\bar{\theta}$ is rotation of the positioner $\bar{\theta}$-axis.

In order to position the direction OT as shown in Figure 38, OT can be considered to have moved from OX to OM by rotation about the OZ axis, then from OM to OT by rotation about the OA' axis. Therefore, the direction $\bar{\phi}$ of OT is the angle between planes XOZ and MOZ.

Since $\bar{\theta}$ is a measure of the mechanical rotation about OA' it is an angle in plane MOZ', which is the plane of the great circle that is normal to OA'.

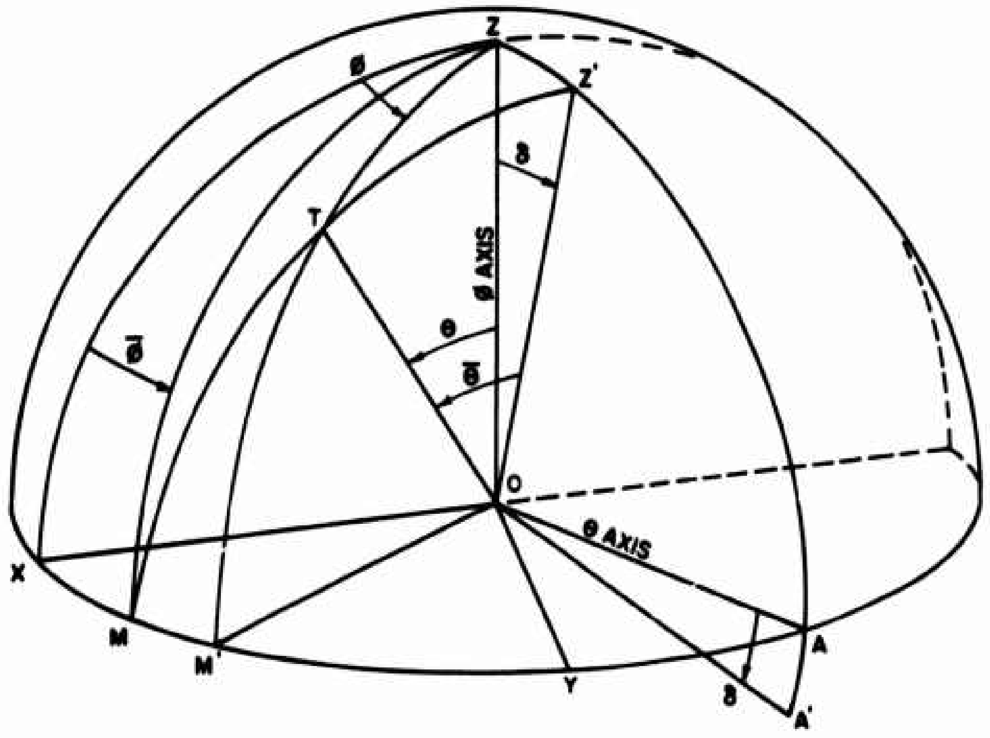

Figure 38. Antenna Positioner with Orthogonality Error

The spherical triangles utilized in the solution are shown in Figure 39. It can be seen that the spherical angles ZX, ZM, ZM' and Z'M are all equal to 90 degrees by definition or construction. Also the spherical angles ZZ'T and TM'M are equal to 90 degrees. Angle δ is the orthogonality error.

From the right spherical triangle Z'ZT

$$\theta = \cos^{-1}(\cos\delta \cos\bar{\theta}) \qquad (63)$$

and

$$\sin^2\theta = 1 - \cos^2\delta \cos^2\bar{\theta} \ . \qquad (64)$$

From the right spherical triangle MM'T

$$\cos\Delta\phi = \frac{\cos(90° - \bar{\theta})}{\cos(90° - \theta)} \ ,$$

or

$$\cos\Delta\phi = \frac{\sin\bar{\theta}}{\sin\theta} \ .$$

Substituting from equation (64) gives

$$\cos\Delta\phi = \frac{\sin\bar{\theta}}{(1 - \cos^2\delta \cos^2\bar{\theta})^{\frac{1}{2}}} \ .$$

It can be seen from Figure 40 that

$$\phi = \bar{\phi} + \Delta\phi \ ,$$

therefore

$$\phi = \bar{\phi} + \cos^{-1}\frac{\sin\bar{\theta}}{(1 - \cos^2\delta \cos^2\bar{\theta})^{\frac{1}{2}}} \ . \qquad (65)$$

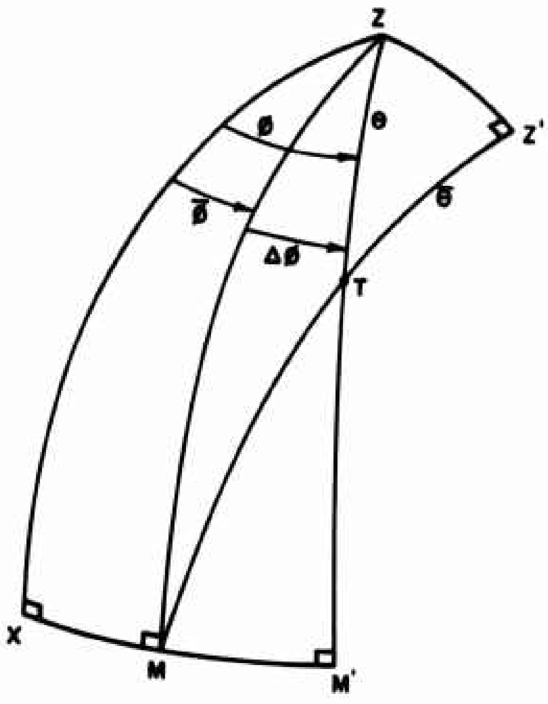

Figure 39. Spherical Triangles of Figure 38

4.4.3 Collimation Error

Collimation error is that error which exists when the direction to the source antenna is not normal to the θ axis. The effect of collimation error is shown in Figure 40. In this analysis the coordinate axes of the antenna are coincident with the coordinate axes of the positioner turntable and the positioner θ axis (OA) is exactly normal to the positioner ϕ axis. Collimation error is identified

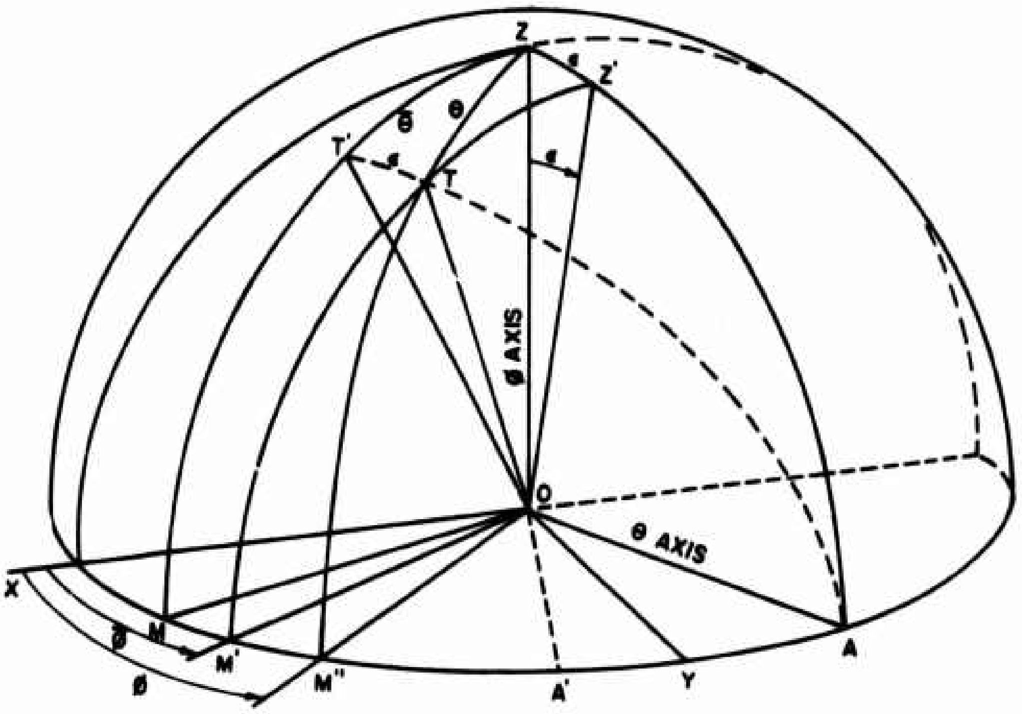

Figure 40. Antenna Positioner with Collimation Error

in Figure 40 as angle ϵ. When the antenna coordinate system XYZ is moved by rotation of the θ axis, OT sweeps a conical surface OZ'M'. The arc Z'M' is a portion of a small circle which is parallel to the great circle (ZM) of axis OA. Arc TT' is a portion of a great circle that intercepts point A. It can be seen that an antenna positioner with collimation error cannot position OT coincident with the OZ-axis; OZ' is the closest approach of OT to the OZ-axis.

The zero position for $\overline{\phi}$ will be defined as that position of the mechanical ϕ-axis that will align OT with the coordinate axis OX. This occurs when OA is at OA', an angle ϵ from Y. The angle $\overline{\theta}$ is again defined as rotation of the axis OA; the zero position for θ is that position which establishes coincidence of OT with OZ'.

The spherical triangles of Figure 40 which are utilized for the solution of angles ϕ, θ are redrawn in Figure 41. By construction, TT'Z is a right spherical triangle with the 90-degree spherical angle at T', and MM''Z is a right spherical triangle with 90-degree spherical angles at both M and M''.

In Figure 40 it can be seen that

$$\epsilon = ZZ' = TT' = MM'$$

and

$$\phi = \bar{\phi} + M'M''$$

or

$$\phi = \bar{\phi} + MM'' - \epsilon \ , \qquad (66)$$

where ϵ is positive when angle A'OT is less than 90°

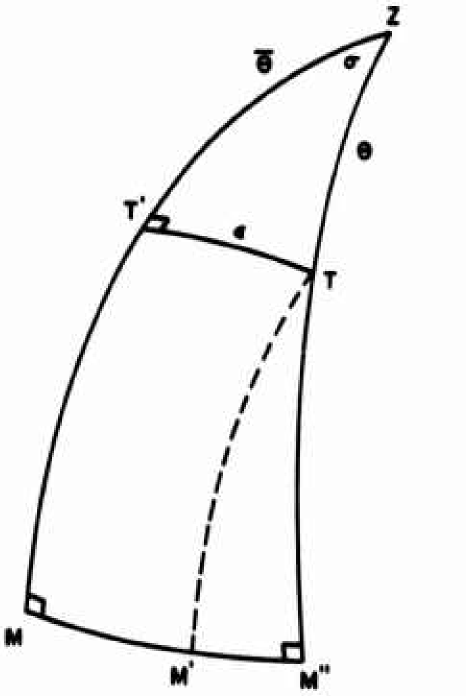

Figure 41. Spherical Triangles of Figure 40

Further

$$\tan \sigma = \frac{\tan \epsilon}{\sin \bar{\theta}} \ ,$$

and since $\sigma = MM''$,

$$MM'' = \tan^{-1} \frac{\tan \epsilon}{\sin \bar{\theta}}$$

which may be substituted in equation (66) to give

$$\phi = \bar{\phi} - \epsilon + \tan^{-1} \frac{\tan \epsilon}{\sin \bar{\theta}} \ . \qquad (67)$$

From the conventional relation between the sides and the angles of the right spherical triangle TT'Z,

$$\theta = \cos^{-1} [\cos \bar{\theta} \cos \epsilon] \ . \qquad (68)$$

4.5 Summary of Geometric Error Calculations

The calculations for a direction ϕ, θ of an antenna system having geometric misalignment errors are summarized as follows:

4.5.1 Coordinate Axis Misalignment

(Figure 62, Appendix A, and Section 4.4.1):

$$\phi = \tan^{-1} \left[\frac{\sin \bar{\theta} \sin (\bar{\phi} - \alpha)}{\sin \bar{\theta} \cos \beta \cos (\bar{\phi} - \alpha) - \cos \bar{\theta} \sin \beta} \right] - \gamma \qquad (101)$$

$$\theta = \cos^{-1} [\cos \bar{\theta} \cos \beta + \sin \bar{\theta} \sin \beta \cos (\bar{\phi} - \alpha)] \qquad (94)$$

4.5.2 Orthogonality Error

(Figure 38 and Section 4.4.2):

$$\phi = \bar{\Phi} + \cos^{-1}\frac{\sin\bar{\theta}}{(1-\cos^2\delta\cos^2\bar{\theta})^{\frac{1}{2}}} \qquad (65)$$

$$\theta = \cos^{-1}(\cos\delta\cos\bar{\theta}) \qquad (63)$$

4.5.3 Collimation Error

(Figure 40 and Section 4.4.3):

$$\phi = \bar{\Phi} - \epsilon + \tan^{-1}\frac{\tan\epsilon}{\sin\bar{\theta}} \qquad (67)$$

$$\theta = \cos^{-1}[\cos\bar{\theta}\cos\epsilon] \qquad (68)$$

4.6 Practical Considerations

4.6.1 General

The study under contract AF 30(602)-3425 required investigation of methods for performing antenna pattern measurements to an angular accuracy of 0.02 degree over a hemisphere and 0.006 degree over a 30 x 30 degree sector. In either case the total angular error is made up of the error elements that are listed in paragraph 4.4. No attempt will be made in this analysis to set an error budget which would allocate a specific maximum value for the errors due to geometric misalignment. However, since there are other errors to be considered it follows that errors due to geometric misalignment could not use all of the total allowable errors.

There are two obvious approaches to the problem of preventing excessively large angular measurement errors which result from geometric misalignment.

The first approach is to design and fabricate the mechanical positioning equipment with such precision and rigidity that the alignment errors are always so small that the resulting errors to ϕ and θ are always within acceptable limits.

The alternate approach is to periodically or continuously measure the geometric misalignment angles by suitable instruments provided with remote indicating or recording capability. The geometric misalignment angles may then be utilized to calculate a more nearly correct value for ϕ and θ by the application of the equations of paragraph 4.5.

The new positioning equipment for the Newport antenna range can probably utilize a compromise combination of the two alternate approaches described above. A combined approach will be practical since the coordinate system alignment and the orthogonality alignment can be accomplished accurately while the collimation alignment will have significant variations due to the support structure deflections.

For example, the coordinate system of the high accuracy antenna is often defined by two orthogonal optical instruments or by precision surfaces that are rigidly fixed to the mechanical structure of the antenna. Similarly, suitably accurate reference surfaces or optical instruments on the positioner turntable could be aligned with the positioner coordinate system. With both coordinate systems accurately defined, the two may be aligned with respect to each other to whatever accuracy is desired.

In April 1965, the orthogonality of the heavy-duty antenna positioner which is to be employed at the Newport antenna range was measured. The angle of misalignment between the upper azimuth and elevation axes was found to be 46 arc seconds. Because of the relatively short distance between the two axes and the rigidity of the structure the variation in orthogonality is expected to be small compared with 46 arc seconds.

When the upper-azimuth and lower-azimuth axes are utilized as ϕ- and θ-axes respectively, the orthogonality is adjustable by means of the elevation axis (see paragraph 4.3.3 and Figure 35).

However, in this configuration relatively large collimation errors can occur as a result of lower axis deviations, which can be caused by wind load stresses and differential expansion from solar radiation. Therefore, continuous monitoring of the lower azimuth axis position is considered both practicable and desirable.

4.6.2 Deflection Monitoring System

Remote indicating electronic levels are recommended for improving the angle measurement accuracy of the positioner installation at the Newport Antenna range. Overall performance of the system will also be considerably improved if solar radiation shielding is employed.

The magnitude of the solar radiation problem can be illustrated by the results of a series of tests that was performed at Scientific-Atlanta in April 1965. Precision, calibrated levels were utilized to measure the inclination of the top of a vertical steel cylinder as it deflected from unequal expansion due to solar heating. The walls of the steel cylinder were 3/8-inch thick, and the cylinder was approximately 240 inches long by 66 inches in diameter. The cylinder was rigidly fastened to a concrete foundation. The exterior surface was coated with red Rustoleum paint. The change in inclination across the north-south and east-west directions was measured at intervals during the day from sunrise and sunset, on a clear day, for which the maximum temperature was 73 degrees Fahrenheit.

As expected, the steel cylinder deflected away from the sun, leaning toward west in the morning, toward north at noon, and toward east in the afternoon. The maximum inclination, which occurred between 3 and 5 PM EST, was approximately 125 arc seconds. The maximum difference in inclination between morning and afternoon was approximately 225 arc seconds (over 0.06 degree).

The seriousness of the solar deflection problem for the new antenna positioner at the Newport antenna range may be examined by comparing it with the deflections that can be expected from wind deflections. The current plans for the Newport installation will put the lower azimuth bearing of the positioner approximately 18 feet above the ground level. The lower azimuth housing is seated on a 12-foot high steel cylinder which is on top of a 6-foot high concrete base. Calculations show that the inclination of the lower azimuth bearing will probably be changed less than 10 seconds by the force of a 30 mph wind on a 50-foot diameter antenna.

It can be seen that the magnitude of lower azimuth axis misalignment caused by solar deflections can be several times that which may be caused by a relatively severe wind load condition. Additionally, the wind load deflection becomes insignificant when small antennas are being tested but the solar deflection would remain a serious problem with any antenna.

To prevent excessively large collimation errors due to solar deflections it is recommended that an insulated shield or barrier be fabricated to cover the positioner support structure from ground level to the lower azimuth bearing. In addition to the solar radiation shield a deflection monitoring system is recommended. The deflection monitor should be installed to indicate the inclination of the lower-azimuth axis relative to the local gravity vector. Electronic levels such as the Taylor-Hobson "Talyvel" or the Geotechnical Corporation Tilt Measuring System, Model 18279, could be utilized for this purpose. Both the Taylor-Hobson and the Geotec levels have remote reading electronic indicators that can be installed in the antenna range control room.

4.6.3 Measurement of Shaft Position

Section 4.4 has defined $\overline{\phi}$ and $\overline{\theta}$ as directions which are determined by the positions of the mechanical axes of the positioning equipment. The shaft positions must be sensed by a measuring instrument. The problems associated with shaft-position encoders and encoder couplings have been under study by several interested groups in recent months.

Scientific-Atlanta, Inc., under contract AF 30(602)-40586 is installing 19-bit shaft encoders on the axes of the three-axis positioner which will be installed at the Newport antenna range. The input shafts of three Wayne-George shaft-position encoders are connected to the rotating elements of the positioner axes with couplings fabricated by Thomas Coupling Division, Rex Chain Belt, Inc. The specifications for the coupling stipulated that the angular error between the drive and the driven shaft be less than 2.5 arc seconds when the assembly is subjected to a maximum of 0.007 inch parallel misalignment and 6 arc minutes of angular misalignment. (See Figure 42.) The installation and testing had not been completed at the time of publication of this report.


Parallel Misalignment

Angular Misalignment

Figure 42. Shaft Misalignment

In early 1965 Wayne-George Corporation completed the design and placed on the market a coupling to be utilized with their shaft-position encoders. Their specifications indicated that coupling will contribute less than 1 second of arc RMS error when subjected to 0.003 inch parallel misalignment and 5 minutes arc of angular misalignment.

During 1965 the Optical Systems Branch, Advanced Development Division, of Goddard Space Flight Center, Greenbelt, Maryland, performed tests on shaft position encoders and encoder couplings from several manufacturers. Their work appears to confirm that a number of couplings are available that will transform positioner-shaft rotation to encoder rotation with an accuracy of 1 to 2 seconds of arc provided the encoder and shaft coupling assembly is aligned to the accuracy specified.

4.6.4 Positioner Requirements for High-Speed Recording

Realization of the data-rate capability of the high-speed radiation recorder which is discussed in Section 2 requires that the positioner with which it is employed not limit the recording speed.

The proposed recorder has a stepping rate of 100 samples per second over selectable angular intervals which are sampled at 360 points. The positioner which will be installed at the Newport antenna test range has a maximum speed of the upper and lower azimuth axes of approximately 0.6 degree per second. On page 34, it was proposed that the sampling points be selectable in the increments shown in Table II. At 360 samples per chart width these sampling intervals result in the measurement sectors shown in the center column.

Sampling Interval (degrees)	Measurement Sector (degrees)	Sampling Rate* (samples/second)
0.01	3.6	60
0.02	7.2	30
0.05	18	12
0.1	36	6
0.2	72	3
0.5	180	1.2
1.0	360	0.6

*For maximum positioner speed of 0.6 degree per second.

Table II. Sampling Interval Versus Sampling Rate

At the presently available maximum positioner speed of 0.6 degree per second, the sampling rates shown in the right-hand column result. It can be seen that at a positioner rotation rate of 0.6 degree per second the high speed radiation distribution recorder would not be utilized at its maximum speed and would be utilized at near maximum rate only when the measurement sector is 3.6 degrees. A higher positioner rotation rate would be desirable for use with antennas requiring measurement sectors greater than 3.6 degrees.

If the antennas to be measured were always in the size range of less than 20 feet diameter and less than 2000 pounds total weight, a relatively simple modification could be utilized to increase the turntable speed of the existing positioner. A 4:1 increase in turntable speed can be achieved by a change to the diameter of the drive motor pulleys. A 10:1 increase in speed can be achieved by installation of new gears in the first stage of the two-stage worm gear reducer that drives the upper and lower azimuth turntables. An increase in speed without changing the motor size would result in a nearly corresponding decrease in the maximum available output torque. However, with these higher speeds available, antennas of 20 feet or less diameter can be rotated through sectors up to 36 degrees at speeds that will utilize the radiation distribution recorder at near maximum rates. Also the wide speed range of the positioner would provide a satisfactory slower speed for measurement of sectors as small as 3.6 degrees.

However, if the simple speed modification described above were utilized, the positioner would not have the available output torque to satisfactorily rotate large, heavy antennas up to 50 feet diameter because of the high torque required for the large inertia and wind drag of the large antenna. Increasing the speed without reducing the output torque will require installation of larger motors.

An alternate to that of supplying larger motors is to provide maximum capability for both the large and also the small antennas by a variable drive ratio. The variable drive ratio will permit the maximum available horsepower to be developed at both a low turntable speed for the large antenna and a high turntable speed for the small antenna. Since the task of changing from a large antenna to a small antenna or vice-versa is usually a major operation the changing of drive ratio could be accomplished manually at the positioner.

If it could be assumed that the large antennas would always have very narrow beams requiring small measurement sectors then the multiple ratio drive system would be an optimum solution to the speed problem. This is of course not the case since for a given antenna size the beamwidth is essentially directly proportional to the wavelength. A multiple ratio drive system can be employed as a compromise between cost and capability; however, the full data-rate capability of the radiation distribution recorder will not be realized in testing large, low frequency antennas.

5. INVESTIGATION OF PARALLAX IN TESTING ASYMMETRICAL ANTENNAS

The investigations reported herein are directed toward a study of parallax in testing asymmetrical antennas. The work is an extension of preliminary investigations which were reported in the final report of Phase I[34]. In the present study a Burroughs Datatron 5000 computer of the Rich Electronic Computer Center of the Georgia Institute of Technology was programmed to calculate antenna patterns as a function of the separation between the source antenna and an antenna under test for certain assumed asymmetrical antenna configurations. In the following paragraphs terms are defined, a summary is given of the technique which was employed in the calculations, and the resulting data are presented.

5.1 Definition of Terms

5.1.1 Parallax

Parallax is defined as the difference in the apparent direction of a point or object as seen from two different station points which are not on a common straight line with the point or object under observation. In Figure 43 let the directions to the point p be measured from station points which are the origins o and o' of two parallel coordinate systems. If the directions to p are defined by (ϕ, θ) and (ϕ', θ') respectively in the two coordinate systems, the ϕ and θ parallax angles are defined by $(\phi' - \phi)$ and $(\theta' - \theta)$*.

The situation depicted in Figure 43 is typical of practical antenna problems, but differs markedly in severity between operational and measurement situations. Let the direction to a target at p be measured in the unprimed coordinate system defined by the shaft orientations of, say, a two-axis positioner with origin at o, the intersection of the positioner axes. Let the center of the antenna be located in o' a distance r_o from o. In the typical operating environment the distance R' to the target is of the order of miles and therefore is so large compared with r_o that ϕ and θ can almost always be considered equal to ϕ' and θ' respectively without measurable error. When measurements are being made of the radiation

---

[34] FR-I, pp. 34-40.

*The transcendental equations for ϕ' and θ' were given in the final report of Phase I (FR-I, p.36) without derivation. These equations are derived in Appendix B of this report.

characteristics of such antennas, on the other hand, the range R' is often not sufficiently great compared with r_o that parallax can be neglected. We will be concerned with the effects of parallax at ranges which are of the order of D^2/λ, where D is the diameter of the antenna under test.

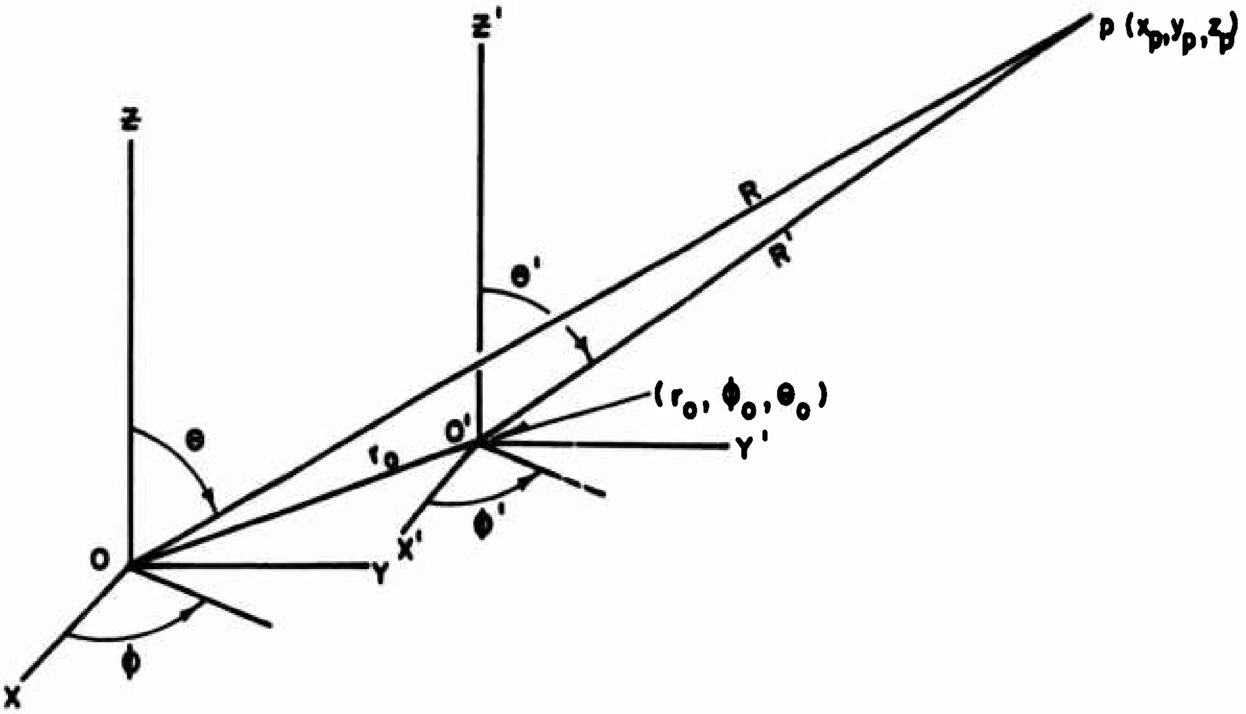

Figure 43. Coordinate Systems Employed for Antenna Measurements, Showing Parallax

5.1.2 Center of Parallax

In the final report of Phase I parallax in measuring radiation patterns of symmetrical antennas was discussed in terms of the center of radiation of the antennas. This term was used synonymously with center of phase. In considering parallax in testing asymmetrical antennas it is necessary to define terms more precisely. In this discussion we will use the term center of parallax in contrast with center of phase, and we will not employ the term center of radiation.

Parallax error can be accounted for and removed in analyzing antenna pattern data, except for a component which exists because of lack of specific information concerning the location of o', the center of parallax of the antenna under test.

The center of parallax will be defined for our purpose as that location o', in or near the aperture of an antenna under test, which can be employed as an origin such that the function $g(R', \phi', \theta')$ describing the normalized radiation pattern of an antenna will be constant with R'.

Strictly speaking, of course, $g(R', \phi', \theta')$ is not constant with R'; thus a true center of parallax does not exist as defined. In pattern measurements of narrow-beam antennas, however, a major concern is that of determining the direction of the main lobe of the radiation pattern. It is of interest, therefore, to consider whether a center of parallax can be defined for practical use in locating the direction which the main beam of an asymmetrical antenna will have at large operational ranges when the measurements are made at distances that are typical in antenna test ranges.

For this study, the direction to the peak of the beam was computed in two ways:

(a) A computer search was employed at given ranges R to determine the point at which the amplitude of the beam had zero slope. The corresponding direction angles to such points are termed Φ_{MR}.

(b) The direction to the 3-db points on each side of the beam maximum was determined by computation at given ranges R, and the average of these angles was taken as the direction to the peak. These angles are termed Φ_R.

The transverse displacement of o' as R was reduced from $R = \infty$ to some finite range R was calculated in the computer program for case (b) above. The defining equation for this displacement can be obtained from Figure 44.

$$\Delta Y = \frac{l}{\cos \Phi_R} \tag{69}$$

$$l \doteq R(\Phi_R - \Phi_\infty) \equiv R\Delta\phi \tag{70}$$

$$\Delta Y = \frac{R\Delta\phi}{\cos \Phi_R} \doteq R\Delta\phi \quad \text{(for small } \Phi_R\text{)} \quad . \tag{71}$$

Plots of $\Delta\phi$, $\Delta\phi_M$ and ΔY are presented for several combinations of phase and amplitude asymmetries as a function of range in paragraph 5.2, where

$$\Delta\phi_M \equiv (\Phi_{MR} - \Phi_{M\infty}) \quad .$$

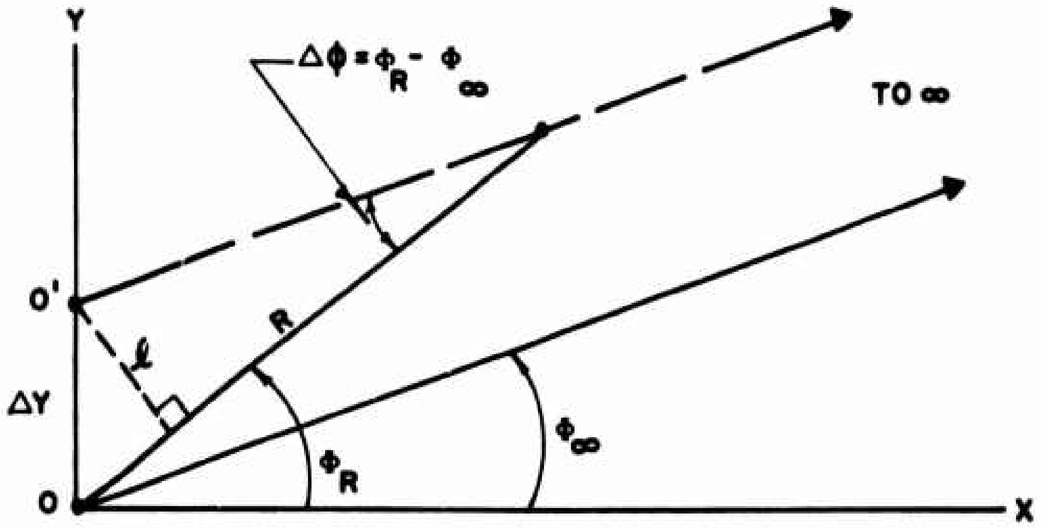

Figure 44. Geometry Defining Center of Parallax

5.1.3 Center of Phase

The center of phase of an antenna can be defined as the location of the center of a sphere of radius R' which is coincident with and of the same radius as the phase front produced by an antenna at a point in space $p(R, \phi, \theta)$. The location of the center of phase is of specific importance in measuring the boresight direction of phase-monopulse or amplitude-monopulse radars[35] because such radars operate by sensing the direction of arrival of a wave as the direction of the normal to the approaching phase front.

Morita[35] has shown that a unique center of phase does not generally exist for the practical antenna. In analogy with the location of the center of curvature of a planar curve, the radius and the location of the center of phase of an antenna are not fixed, but vary with the location in space of the field point. Although the radius of curvature of the wavefront of a beam in space is not

---

[35] Tetsu Morita, Determination of Phase Centers and Amplitude Characteristics of Radiating Structures, Tech. Report No. 1, SR 1, Project 898, Stanford Res. Inst., Menlo Park, California, Contract DA 04-200-ORD-273, AD68240; March 1955.

generally constant with rotation of a plane of exploration about the axis of the beam, the axial location of the center of phase is usually not of great importance in practical applications; therefore our concentration of attention will be directed toward the transverse location of the center of phase.

In the following investigations antennas will be considered which are symmetrical in θ but asymmetrical in ϕ. Considering only the transverse location of the center of phase, a coordinate system X"Y"Z" (see Figure 45) will be defined which is parallel with a coordinate system XYZ in which a narrow-beam antenna radiates with its beam axis nearly parallel with the X axis.

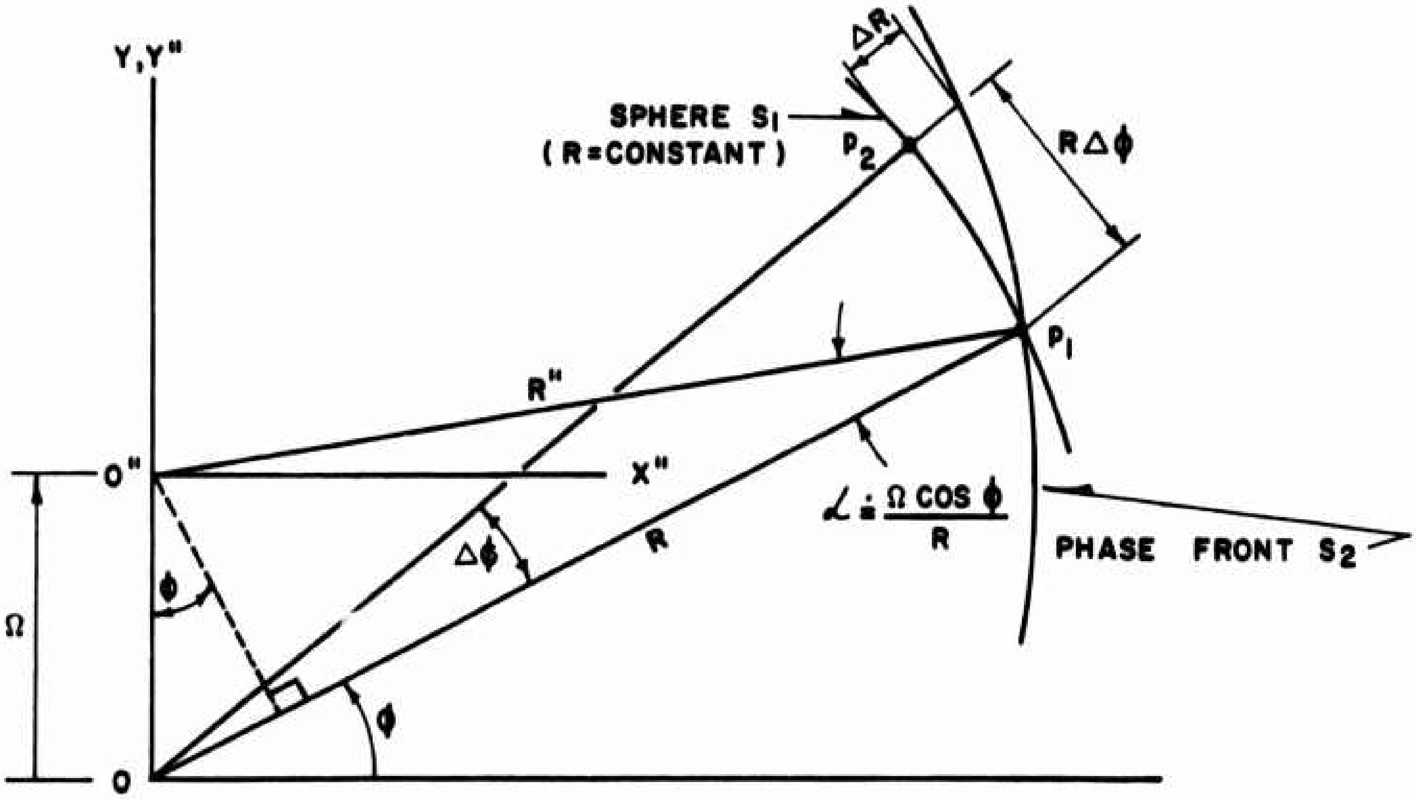

Figure 45. Geometry Defining Center of Phase

Consider the sphere S_1 centered at o, and the phase front S_2 which intersects S_1 at p_1. Let the phase of the field at p_1 be ψ_1. Now call ψ_2 the phase at p_2 a distance $R\Delta\phi$ from p_1 in the ϕ direction.

From the geometry, for $\Delta R \ll R$,

$$\frac{\Delta R}{R\Delta\phi} \doteq \alpha \quad , \tag{72}$$

where α is defined as the angle at p_1 between S_1 and S_2 in the XY plane.

Also,

$$\alpha \doteq \frac{\Omega \cos\phi}{R} \quad \text{for } R >> \Omega \quad , \tag{73}$$

and

$$\Delta R \doteq \frac{\lambda}{2\pi}(\psi_2 - \psi_1) \equiv \frac{\lambda}{2\pi} \Delta\psi \quad . \tag{74}$$

From (72), (73), and (74),

$$\Omega \doteq \frac{\lambda \Delta\psi}{2\pi \Delta\phi \cos\phi} \doteq \frac{\lambda}{2\pi} \frac{\Delta\psi}{\Delta\phi} \quad \text{(for small } \phi) \quad . \tag{75}$$

Calculations were made in this study of $\Omega(R)$ for certain assumed antenna asymmetries using p_2 and p_1 as the half-power points of the main lobe in the XY plane.*

5.1.4 Boresight Deviation

A practical application involving the effect of parallax occurs in testing antennas for amplitude-monopulse, direction-of-arrival sensors. Antennas of this type sense the direction of arrival of a wave as that direction for which

$$\Sigma \cdot \overline{\Delta} = o \ ,$$

where Σ is the phasor representing the sum-channel signal from the monopulse network, and $\overline{\Delta}$ is the phasor representing the difference channel signal. This is tantamount to the condition that

$$|A| = |B| \quad ,$$

where A and B are the magnitudes of the signals produced by the opposite lobes of the monopulse pattern for the crossover direction ϕ_o. A problem of specific concern is that of the behavior of the directions ϕ_o with the separation between the source antenna and the antenna under test.

---

*The values of Ω thus calculated were checked for several cases which are considered to be extreme by defining a third point p' as the peak of the beam and solving equation (75) for values of ϕ and ψ related to the point pairs p_1, p' and p_2, p'. The average values of Ω calculated in this manner were in close agreement with those presented here.

Plots of ϕ_o versus R are calculated and presented for representative asymmetrical cases in Section 5.3.

5.2 Radiation Pattern Calculations

5.2.1 Theoretical Development

Radiation patterns were calculated for a number of simulated antenna configurations by the aperture-field method, assuming the total radiated energy to be contained in a single polarization. For this case the contribution by direct radiation from the aperture to the field at p is described by equation (15) where S_i is the active aperture of the antenna, which we will henceforth call simply S, and which is assumed to be a planar surface lying in the YZ plane of Figure 46. This integral does not give the total field at p, but only the contribution from the aperture; however we will assume that almost all of the energy from the antenna passes through the aperture and that the contribution to the field at p of sources other than the field over S can be neglected.

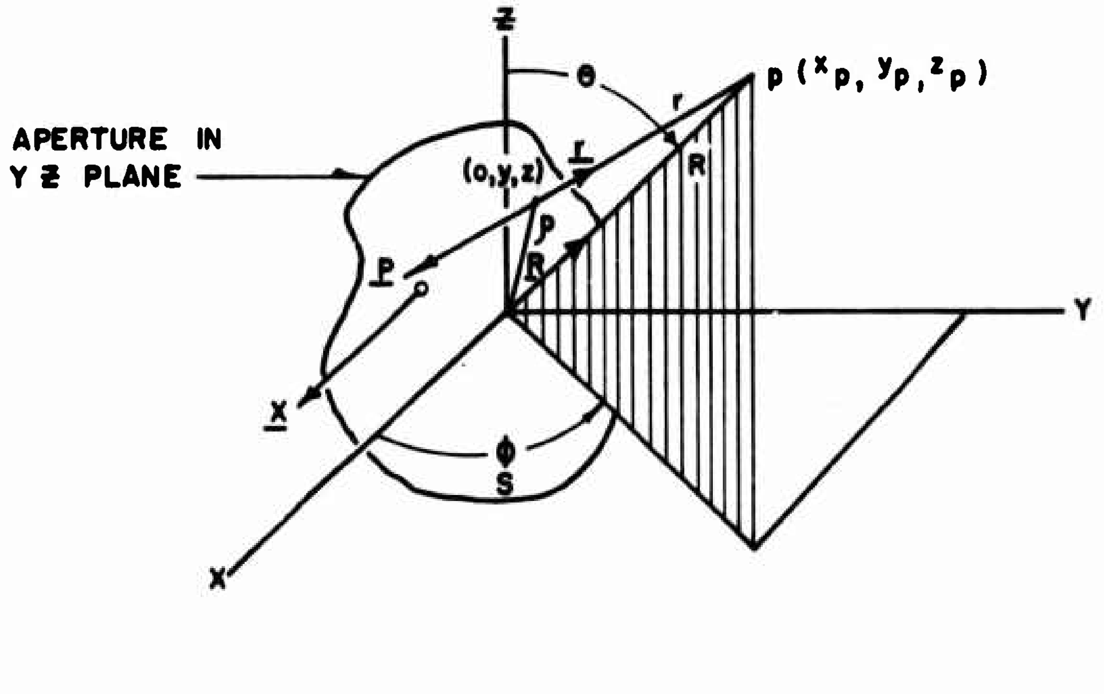

Figure 46. Aperture Geometry for Theoretical Development of Aperture Field Method

Equation (15) leads to the scalar diffraction integral[36] under the assumptions which have been made:*

$$\bar{E}_p \doteq K \int_s F(o,y,z) e^{j\psi(o,y,z)} \frac{e^{-jkr}}{r}\left[\left(jk+\frac{1}{r}\right)\underline{x}\cdot\underline{r} + jk\underline{x}\cdot\underline{P}\right] ds, \tag{76}$$

where, with reference to Figure 46,

K is a constant of proportionality
F(o, y, z) is the amplitude of the field distribution over S
$\psi(o, y, z)$ is the phase of the field distribution over S
r is the distance from a source point (o, y, z) to a field point $p(x_p, y_p, z_p)$
k is the wave number $2\pi/\lambda$, λ being the wavelength
$\underline{P}$, $\underline{x}$, $\underline{R}$ and $\underline{r}$ are unit vectors, and
$\underline{P}$ denotes the direction of power flow through the aperture.

For the problem at hand we can restrict p to the Fresnel and Fraunhofer regions, which are sufficiently removed from the aperture that

1. $1/r$ is negligible compared with k,
2. $\underline{x}\cdot\underline{r} \doteq \underline{x}\cdot\underline{R} = \sin\theta\cos\phi$,
3. $r = R$ except in the phase term e^{-jkr}.

In addition we will postulate that the direction of power flow through the aperture is nearly enough parallel with the x-axis that $\underline{x}\cdot\underline{P} = 1$ with negligible error.

If we designate the rectangular coordinates of p by (x_p, y_p, z_p), the distance r from p to the point (o, y, z) in the aperture is given by

$$r = \left[x_p^2 + (y_p - y)^2 + (z_p - z)^2\right]^{\frac{1}{2}} . \tag{77}$$

The transformation,

$$\begin{aligned} x_p &= R\sin\theta\cos\phi, \\ y_p &= R\sin\theta\sin\phi, \text{ and} \\ z_p &= R\cos\theta \end{aligned} \tag{78}$$

---

[36] Silver Samuel, op. cit. (see reference 11), p. 170.

*In this section the exponential form e^{-jkr} will be employed rather than the form e^{jkr} as in Section 3. The choice is optional and has no bearing on the outcome of the argument. (See J. A. Stratton, Electromagnetic Theory, McGraw-Hill, 1941, page viii.)

allows writing

$$r = [(R \sin\theta \cos\phi)^2 + (R \sin\theta \sin\phi - y)^2 + (R \cos\theta - z)^2]^{\frac{1}{2}} , \tag{79}$$

which through routine reduction gives

$$r = [R^2 - 2R(y \sin\theta \sin\phi + z \cos\theta) + (y^2 + z^2)]^{\frac{1}{2}} . \tag{80}$$

For our application symmetry will be postulated about the X-axis in θ, so we will require p to move only in ϕ in the XY plane. Further the region of exploration in ϕ will be near the X-axis, and sin θ will be equal to unity and cos θ equal to zero. Under these conditions equation (80) becomes

$$r = [R^2 - (2R\, y \sin\phi - y^2 - z^2)]^{\frac{1}{2}} \tag{81}$$

and r can be approximated by the first two terms of the binomial expansion, giving

$$r \doteq R - y \sin\phi + \frac{y^2 + z^2}{2R} . \tag{82}$$

These approximations allow (76) to be written, since we are interested only in relative phases and magnitudes at specific values of R,

$$\overline{A}_p \doteq \int_s F(o, y, z)\, e^{j[\psi(o, y, z) + k(y \sin\phi - \frac{y^2 + z^2}{2R})]}\, ds \tag{83}$$

where

$\overline{A}_p = \overline{C}\, \overline{E}_p$, and

$\overline{C}$ is an appropriate phasor.

The aperture S which was assumed for the simulated antenna configurations employed is shown in Figure 47. The aperture is circular in shape, of radius a and is assumed to be illuminated by fields which are described by the functions,

$$F(o, y, z) = [K_1 + \cos\tfrac{\pi}{2}\rho][1 + K_2 y] \tag{84}$$

and

$$\psi(o, y, z) = K_3 y + K_4 y^3 + K_5 \rho^2 . \tag{85}$$

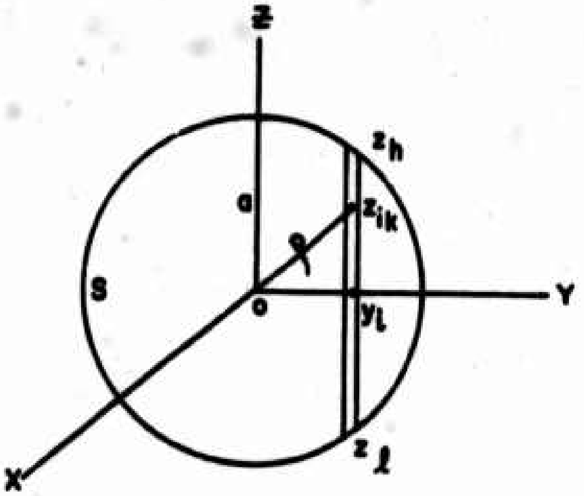

Figure 47. Aperture Geometry Employed in Antenna Pattern Calculations

Equation (83) is accordingly written

$$\overline{A}_p \doteq \int_{-a}^{a} \left[\int_{z_\ell}^{z_h} F(y, z)\, e^{j(K_5 - \frac{k}{2R}) z^2} dz \right] e^{j[K_3 y + K_4 y^3 + (K_5 - \frac{k}{2R}) y^2 + ky \sin \phi]} dy \qquad (86)$$

Since the integral within the brackets is not a function of ϕ, the calculations can be made by the equivalent slit method.[37]. In programming the computer for achieving an approximation to (86) by a process of finite summation, F and ψ were approximated by 41 sample points along each axis.

5.3 Presentation of Data

In the computer calculations determining center of parallax and center-of-phase the following sets of input data were employed to represent typical asymmetries of F and ψ of equation (83).

---

[37] L. Clayton and J. S. Hollis, "Antenna Polarization Analysis by Amplitude Measurement of Multiple Components," Microwave Journal, Volume 8, No. 1, January 1965.

$K_1 = (0.462)$

$K_2 = (0),\ (0.5),\ (1.0)$

$K_3, K_4 = (0, 0),\ (1.4,\ 0),\ (0,\ 1.57),\ (1,\ 1)$

$K_5 = (0),\ (\pi/2),\ (-\pi/2)$

$\frac{R\lambda}{D^2} = (0.5),\ (1),\ (2),\ (4),\ (\infty)$.

Graphs of the functions F(o, y, z) employed in the calculations are shown in Figure 48, showing rotational symmetry of F about the x-axis for K_2 equal to zero and increasing asymmetry in the y direction for increasing values of K_2.

5.3.1 Center-of-Parallax and Center-of-Phase Calculations

In Figures 49 through 57 values of ΔY, $\Delta\phi$, $\Delta\phi_M$ and Ω, as defined in paragraphs 5.1.2 and 5.1.3, are presented as functions of $R\lambda/D^2$ for the indicated values of the parameters listed above. For completeness certain graphs are included for cases for which the values of ΔY, $\Delta\phi$, $\Delta\phi_M$ and Ω are zero by symmetry.

For convenience, all curves are plotted upward, regardless of algebraic sign. Where a curve is actually a plot of negative values, a minus sign precedes the curve designator. In cases where the graphs become congested, some curves are dashed in order to make them more readable.

5.3.2 Boresight Deviation Calculations

Calculations were made of boresight directions ϕ_o (section 5.1.4), as functions of range for simulated amplitude-monopulse radar antennas. The aperture illumination functions employed were

$$F_L(o, y, z) = [K_{1L} + \cos\tfrac{\pi}{2}\rho]\ [1 + K_{2L}y] \quad , \tag{87}$$

$$F_R(o, y, z) = [K_{1R} + \cos\tfrac{\pi}{2}\rho]\ [1 + K_{2R}y] \quad , \tag{88}$$

$$\psi_L(o, y, z) = K_{3L}y + K_{4L}y^3 + K_5\rho^2 \quad , \text{ and} \tag{89}$$

$$\psi_R(o, y, z) = K_{3R}y + K_{4R}y^3 + K_5\rho^2 \quad , \tag{90}$$

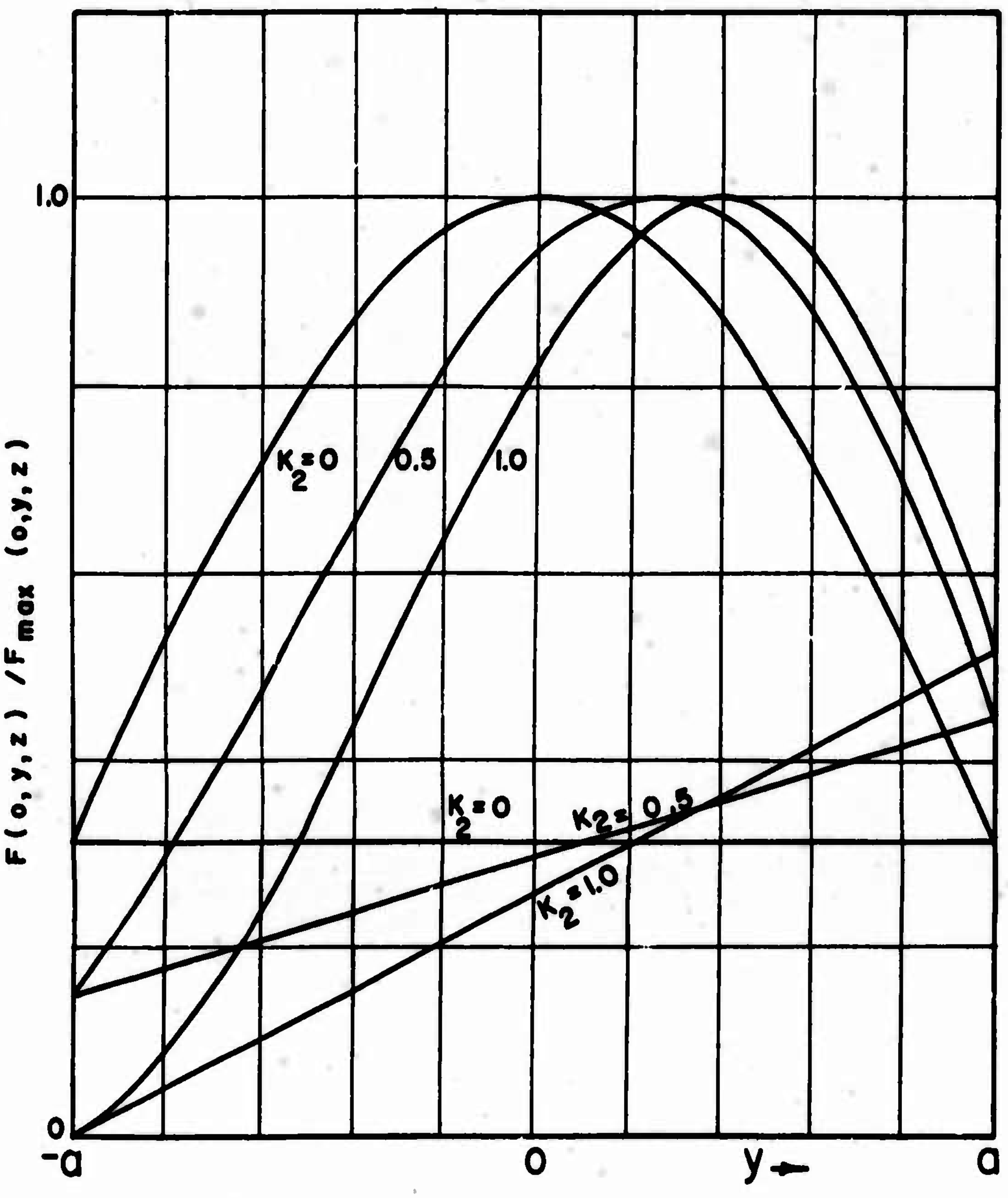

Figure 48. Functions F(o, y, z) Employed in Computer Calculations. Upper curves are cuts through aperture at z = o [F(o, y, o)]. Lower curves (straight lines) show fields at periphery of aperture [F(o, y, z)/ρ = a].

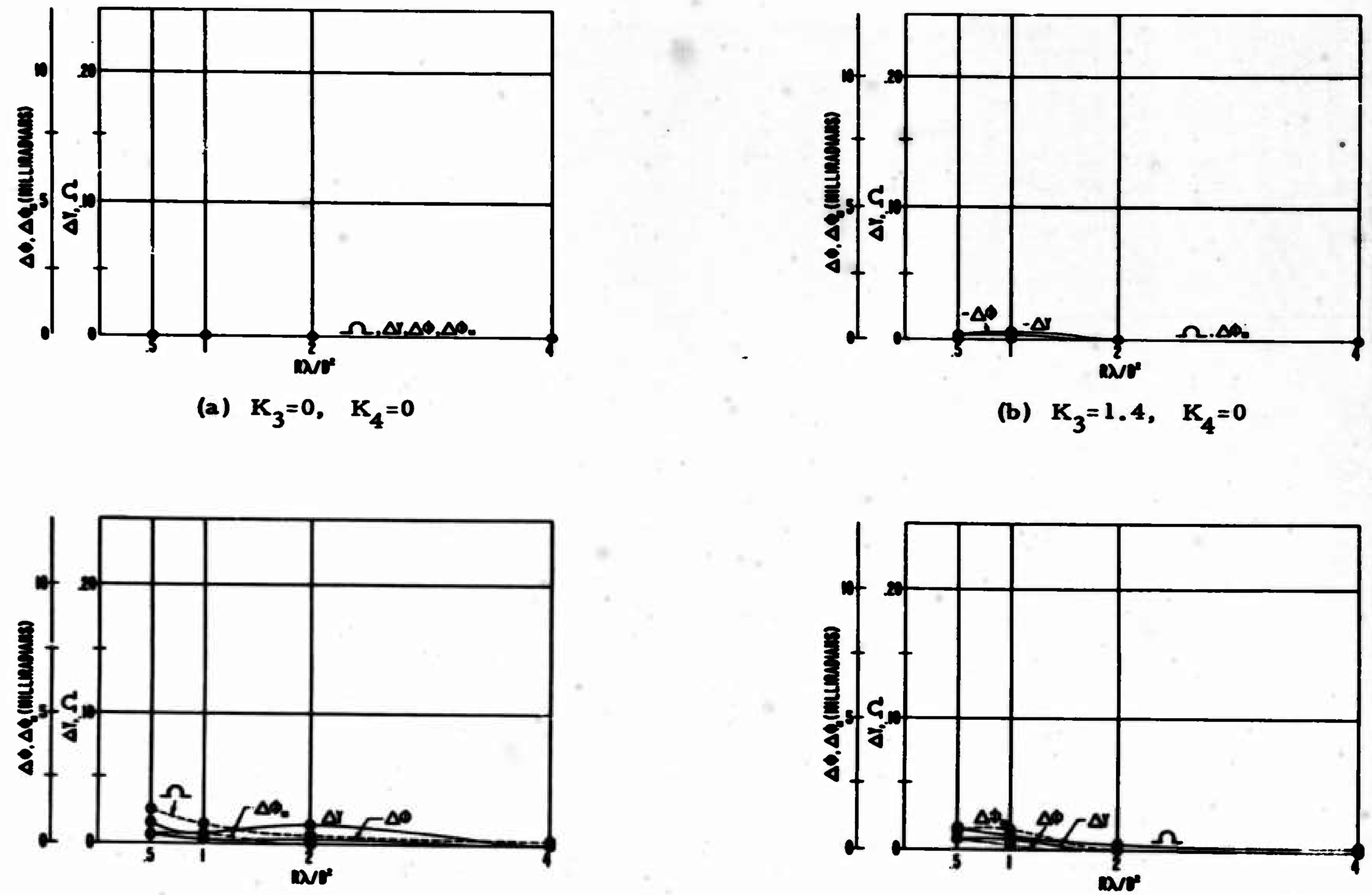

(a) $K_3=0$, $K_4=0$

(b) $K_3=1.4$, $K_4=0$

(c) $K_3=0$, $K_5=1.57$

(d) $K_3=1.0$, $K_4=1.0$

Figure 49. Results of Parallax and Center-of-Phase Calculations, $K_2=0$, $K_5=0$

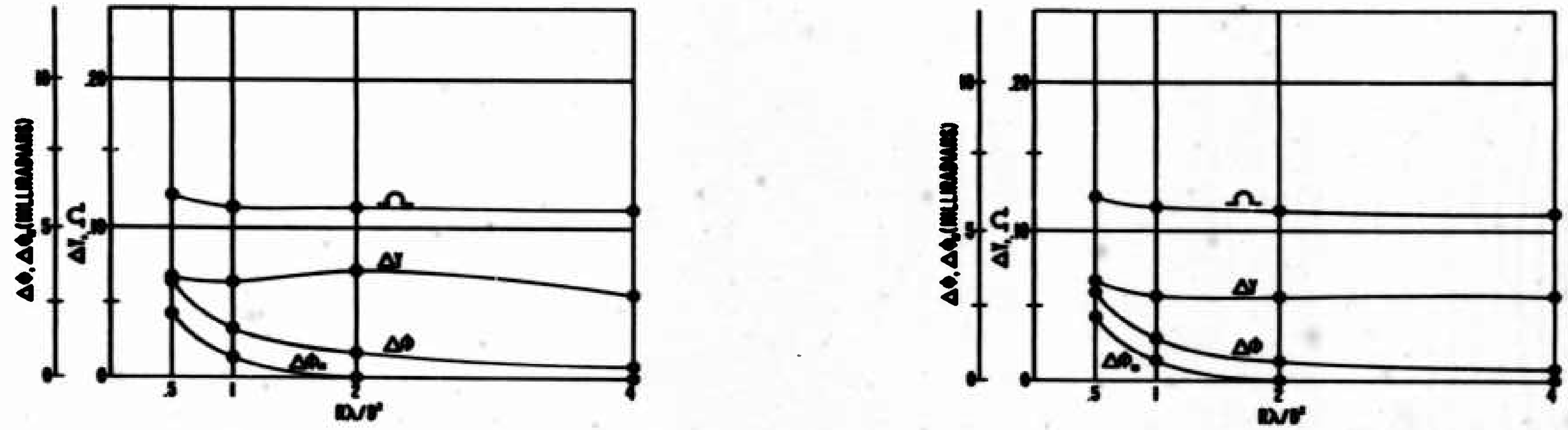

(a) $K_3=0$, $K_4=0$

(b) $K_3=1.4$, $K_4=0$

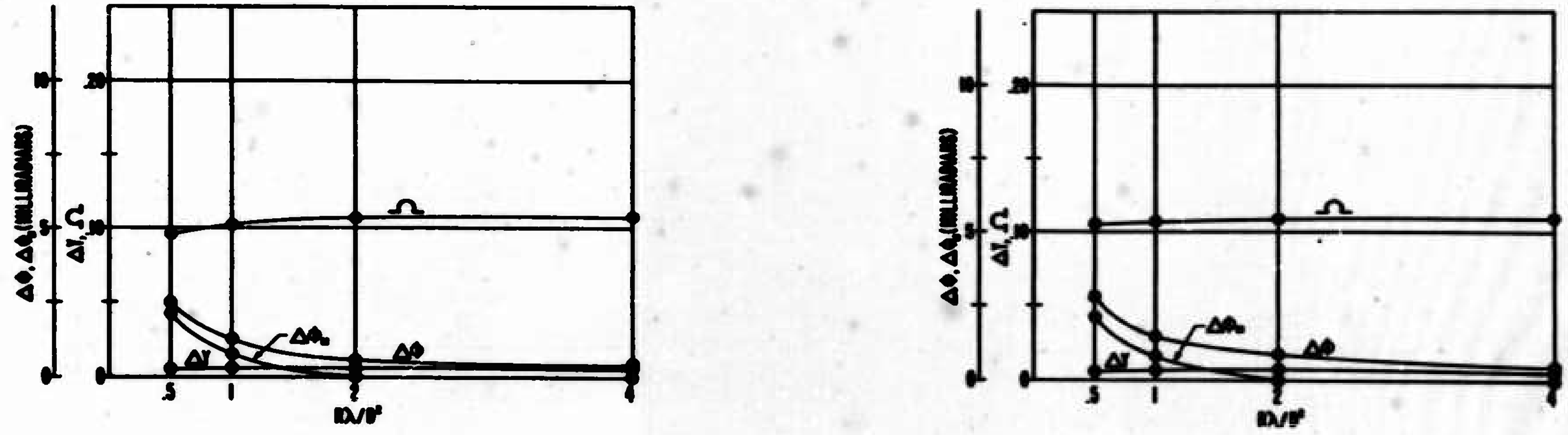

(c) $K_3=0$, $K_5=1.57$

(d) $K_3=1.0$, $K_4=1.0$

Figure 50. Results of Parallax and Center-of-Phase Calculations, $K_2=0.5$, $K_5=0$

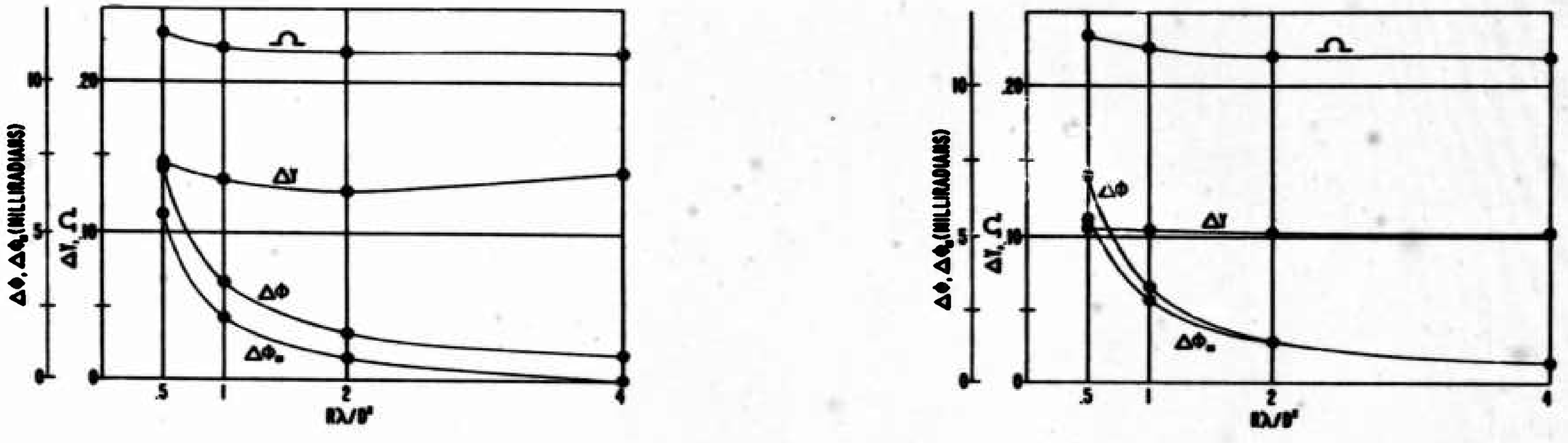

(a) $K_3=0, \ K_4=0$ (b) $K_3=1.4, \ K_4=0$

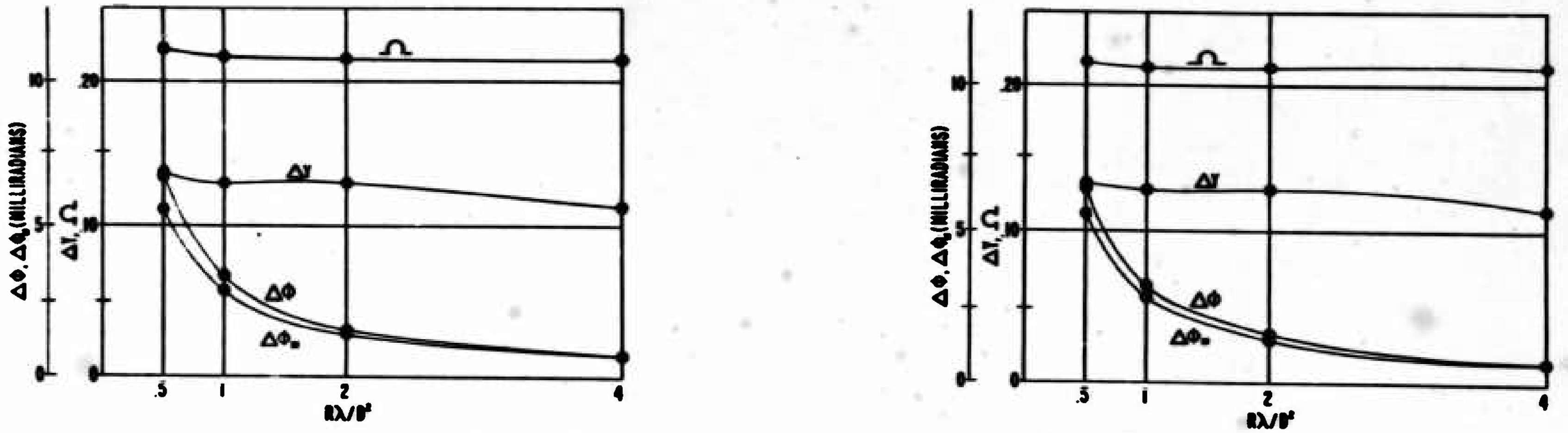

(c) $K_3=0, \ K_5=1.57$ (d) $K_3=1.0, \ K_4=1.0$

Figure 51. Results of Parallax and Center-of-Phase Calculations, $K_2=1.0$, $K_5=0$

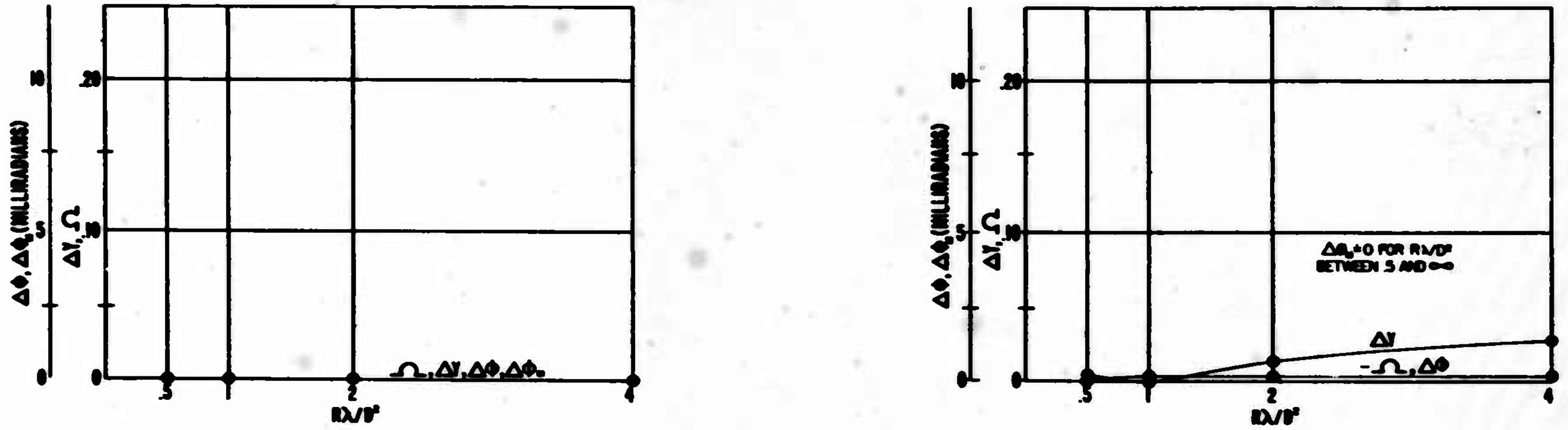

(a) $K_3=0$, $K_4=0$

(b) $K_3=1.4$, $K_4=0$

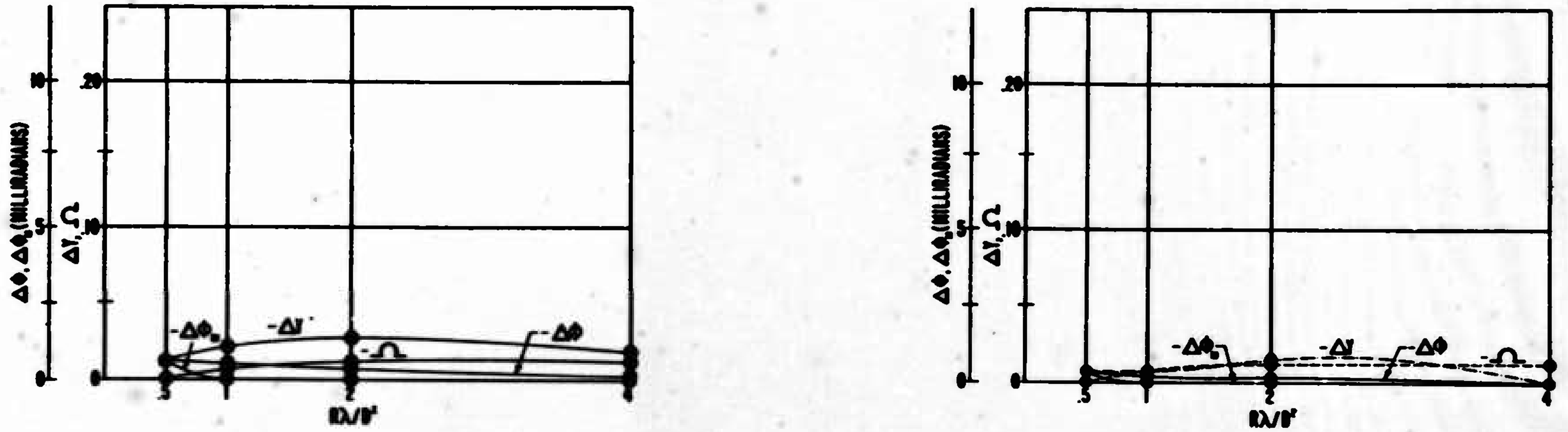

(c) $K_3=0$, $K_5=1.57$

(d) $K_3=1.0$, $K_4=1.0$

Figure 52. Results of Parallax and Center-of-Phase Calculations, $K_2=0$, $K_5=\pi/2$

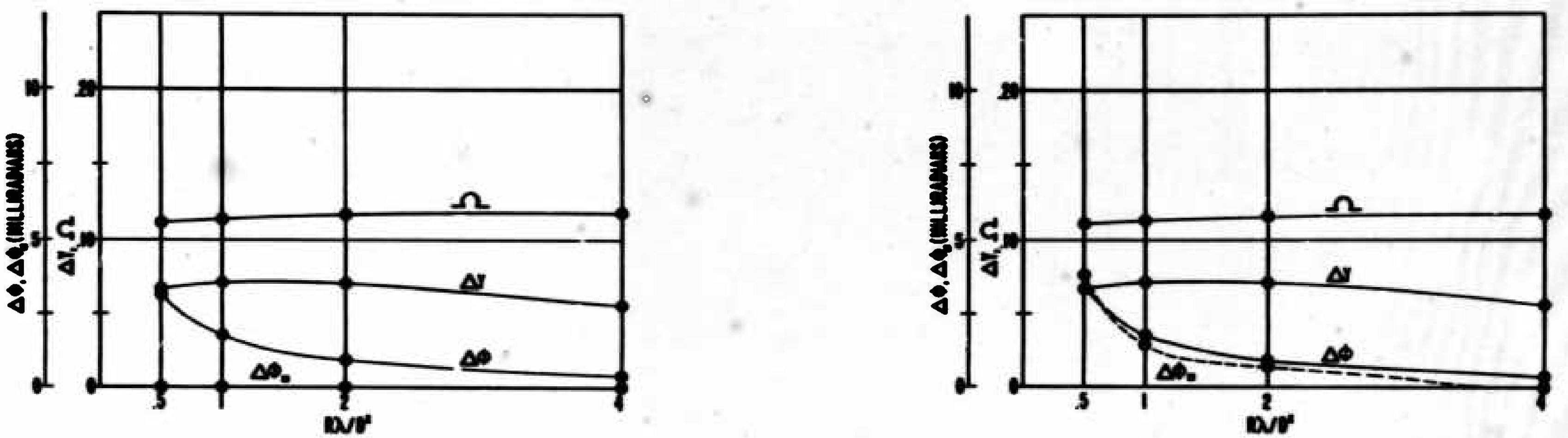

(a) $K_3=0$, $K_4=0$

(b) $K_3=1.4$, $K_4=0$

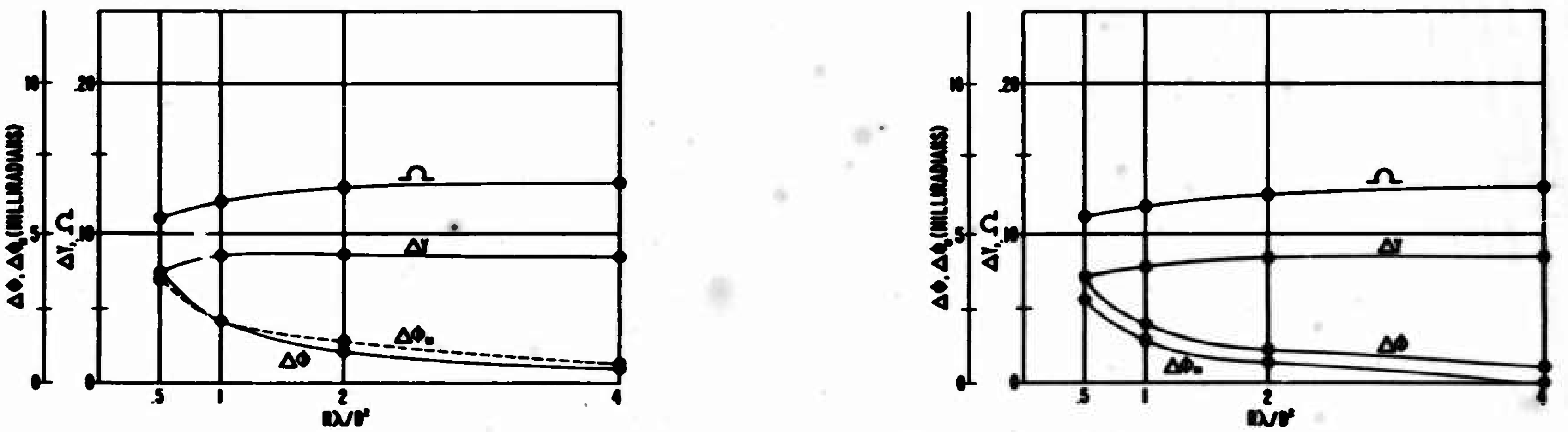

(c) $K_3=0$, $K_5=1.57$

(d) $K_3=1.0$, $K_4=1.0$

Figure 53. Results of Parallax and Center-of-Phase Calculations, $K_2=0.5$, $K_5=\pi/2$

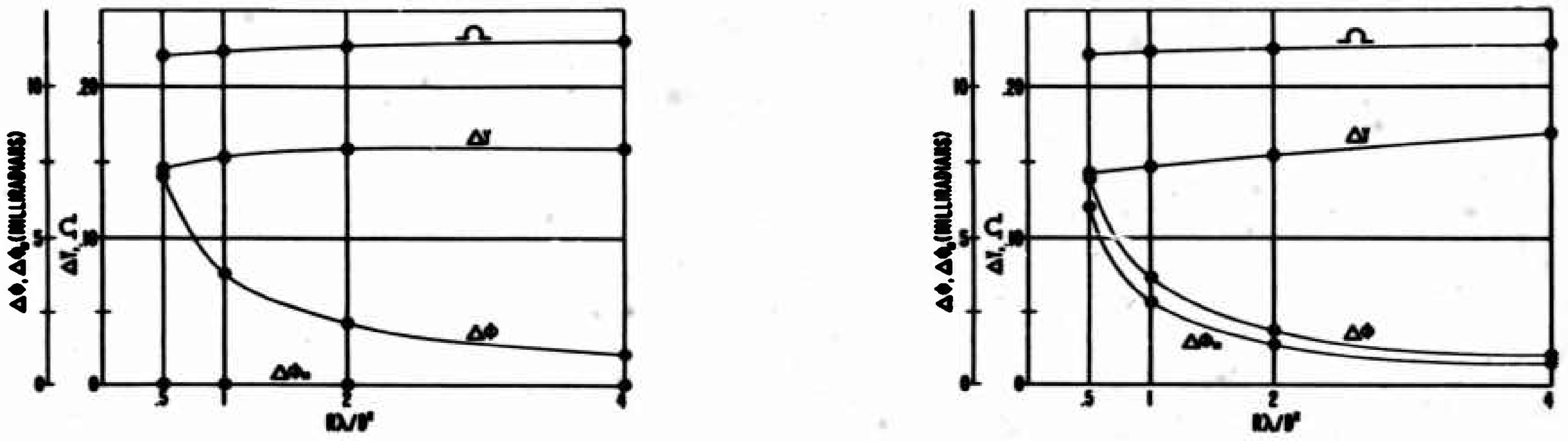

(a) $K_3=0$, $K_4=0$

(b) $K_3=1.4$, $K_4=0$

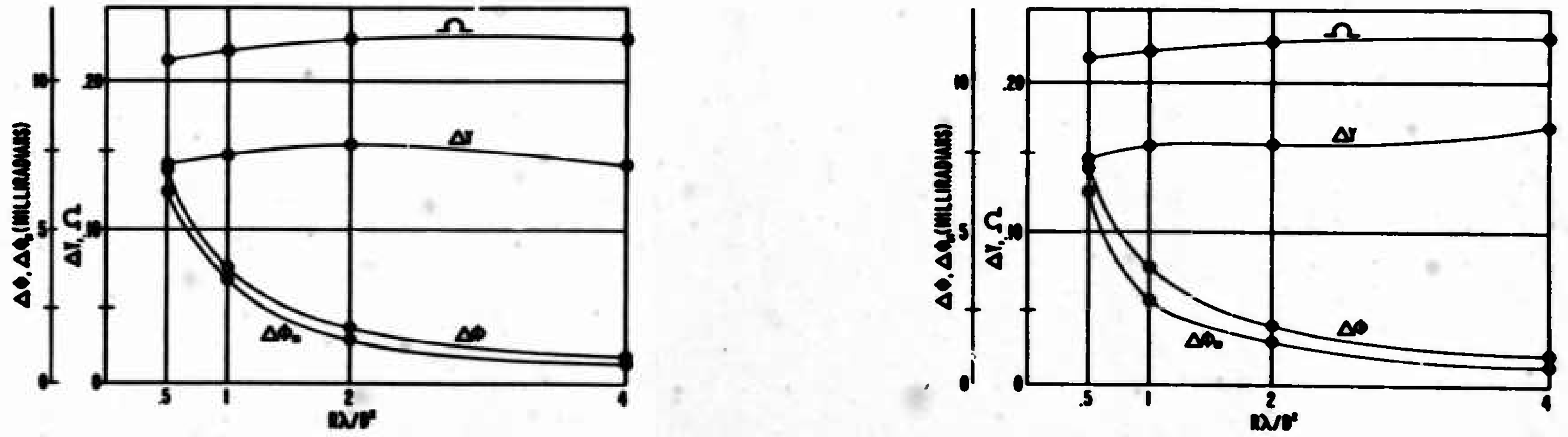

(c) $K_3=0$, $K_5=1.57$

(d) $K_3=1.0$, $K_4=1.0$

Figure 54. Results of Parallax and Center-of-Phase Calculations, $K_2=1.0$, $K_5=\pi/2$

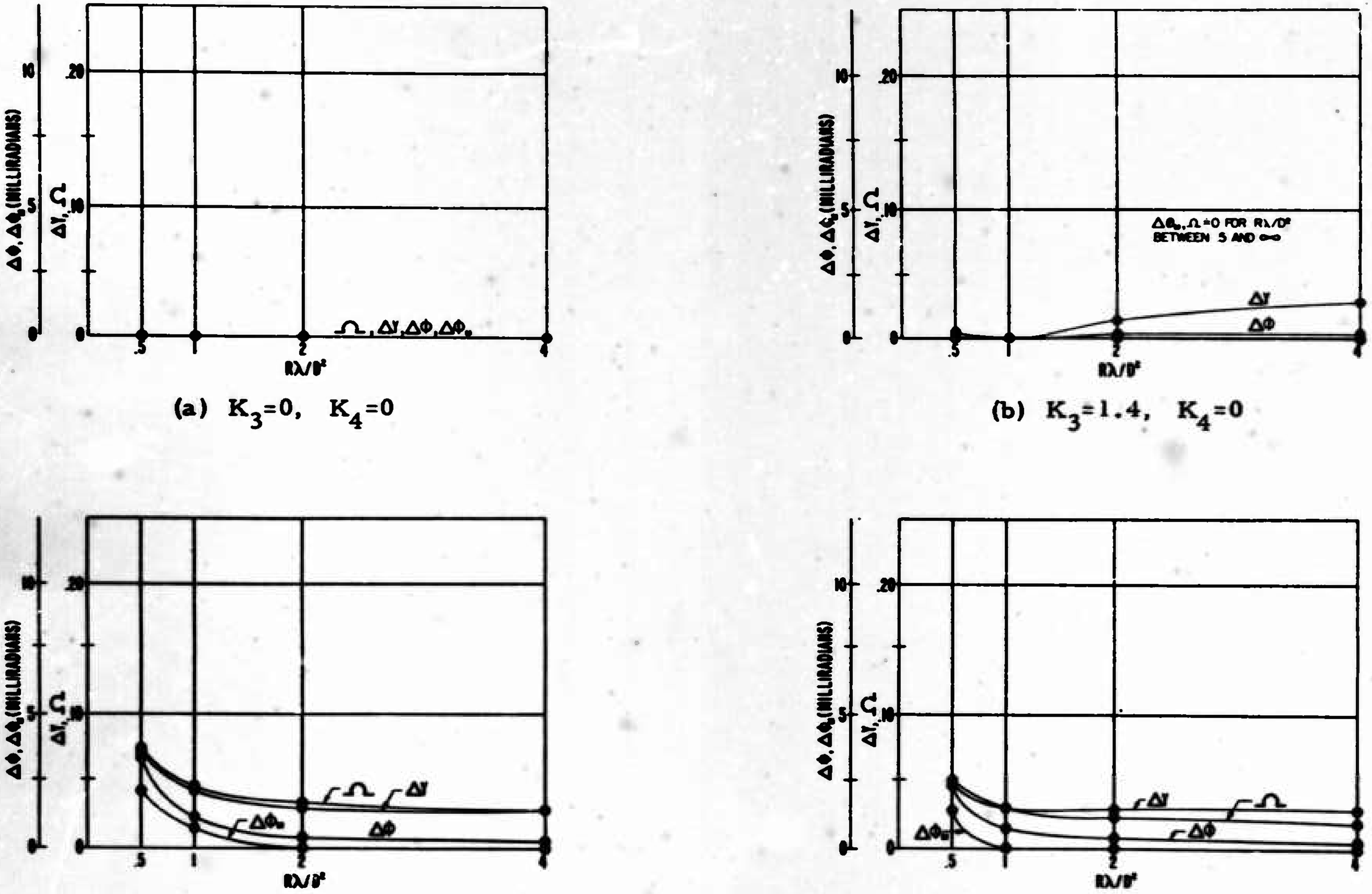

(a) $K_3=0$, $K_4=0$

(b) $K_3=1.4$, $K_4=0$

(c) $K_3=0$, $K_5=1.57$

(d) $K_3=1.0$, $K_4=1.0$

Figure 55. Results of Parallax and Center-of-Phase Calculations, $K_2=0$, $K_5=-\pi/2$

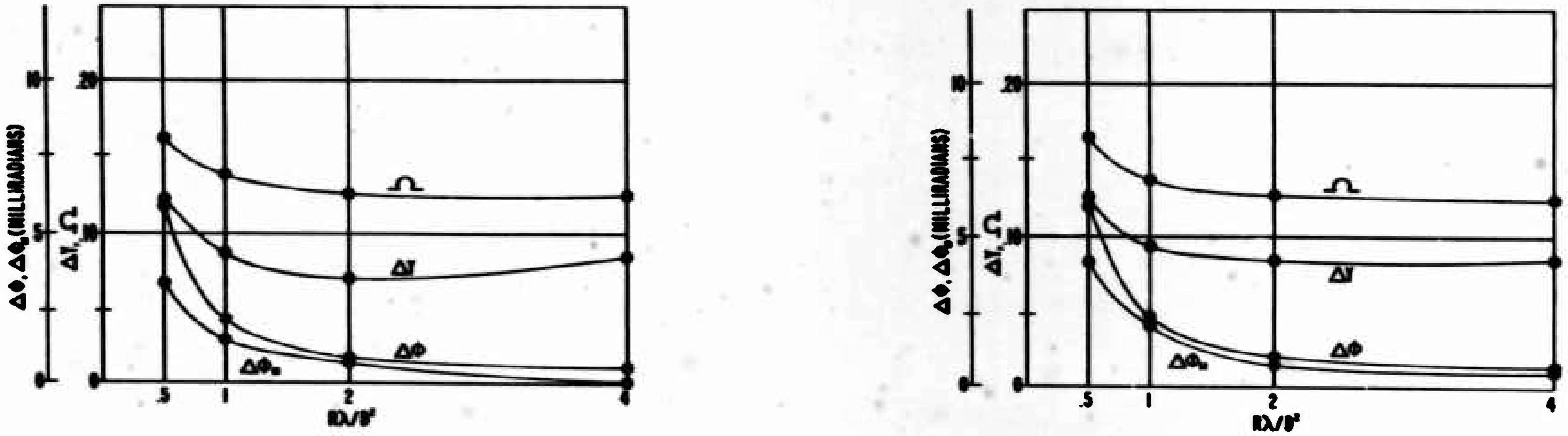

(a) $K_3=0$, $K_4=0$

(b) $K_3=1.4$, $K_4=0$

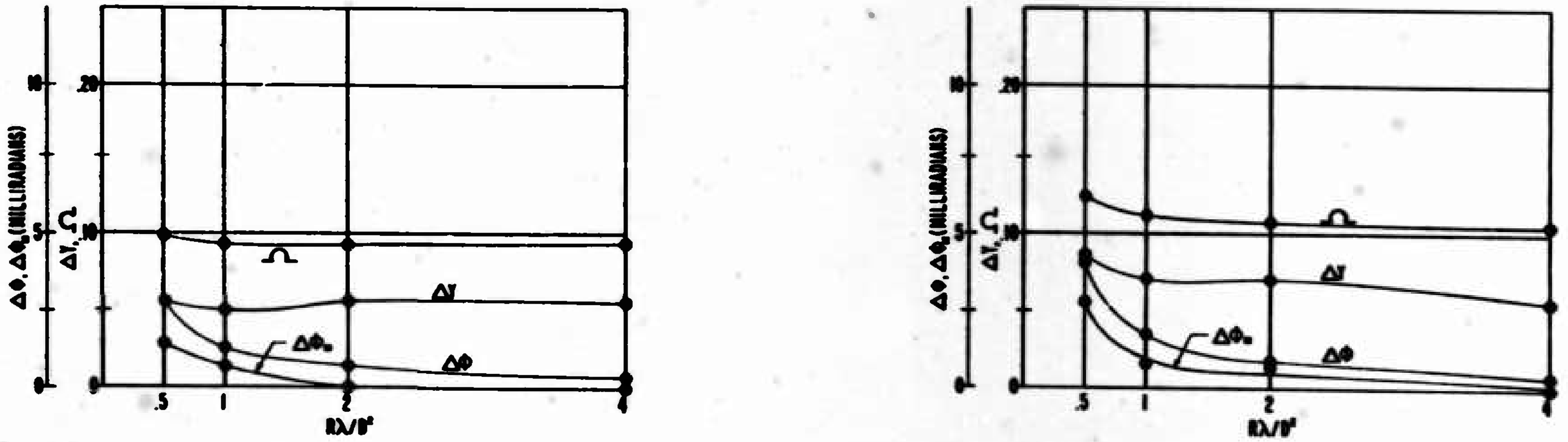

(c) $K_3=0$, $K_5=1.57$

(d) $K_3=1.0$, $K_4=1.0$

Figure 56. Results of Parallax and Center-of-Phase Calculations, $K_2=0.5$, $K_5=-\pi/2$

(a) $K_3=0$, $K_4=0$

(b) $K_3=1.4$, $K_4=0$

(c) $K_3=0$, $K_5=1.57$

(d) $K_3=1.0$, $K_4=1.0$

Figure 57. Results of Parallax and Center-of-Phase Calculations, $K_2=1.0$, $K_5=-\pi/2$

where the subscripts L and R indicate left ($+\phi$) and right ($-\phi$) lobe illumination functions. The following parameters were employed:

$K_{1L} = (0.462)$

$K_{1R} = (0.462)$

$K_{2L} = (0)$

$K_{2R} = (0), (0.5), (1)$

$K_{3L}, K_{4L} = (-1.4, 0), (0, -1.57), (-1, -1)$

$K_{3R}, K_{4R} = (1.4, 0), (0, 1.57), (1, 1)$

$K_5 = (0), (\pi/2), (-\pi/2)$

$\frac{R\lambda}{D^2} = (0.5), (1), (2), (4), (\infty)$

Calculated values of ϕ_o versus $R\lambda/D^2$ are plotted in Figures 58 through 60. The ordinates for these plots are given in terms of the parameter,

$$u = \frac{2\pi}{\lambda} a \sin\phi = \frac{2\pi}{\lambda} a \phi \quad (\text{for } \phi << 1) \ . \tag{91}$$

For the particular cases calculated, the aperture was very nearly 20 wavelengths in diameter, so that $\phi_o = u/20\pi$. To use these curves for a general aperture of diameter $= n\lambda$, the corresponding crossover point is

$$\phi_{on} = \frac{20\ \phi_o}{n} \quad . \tag{92}$$

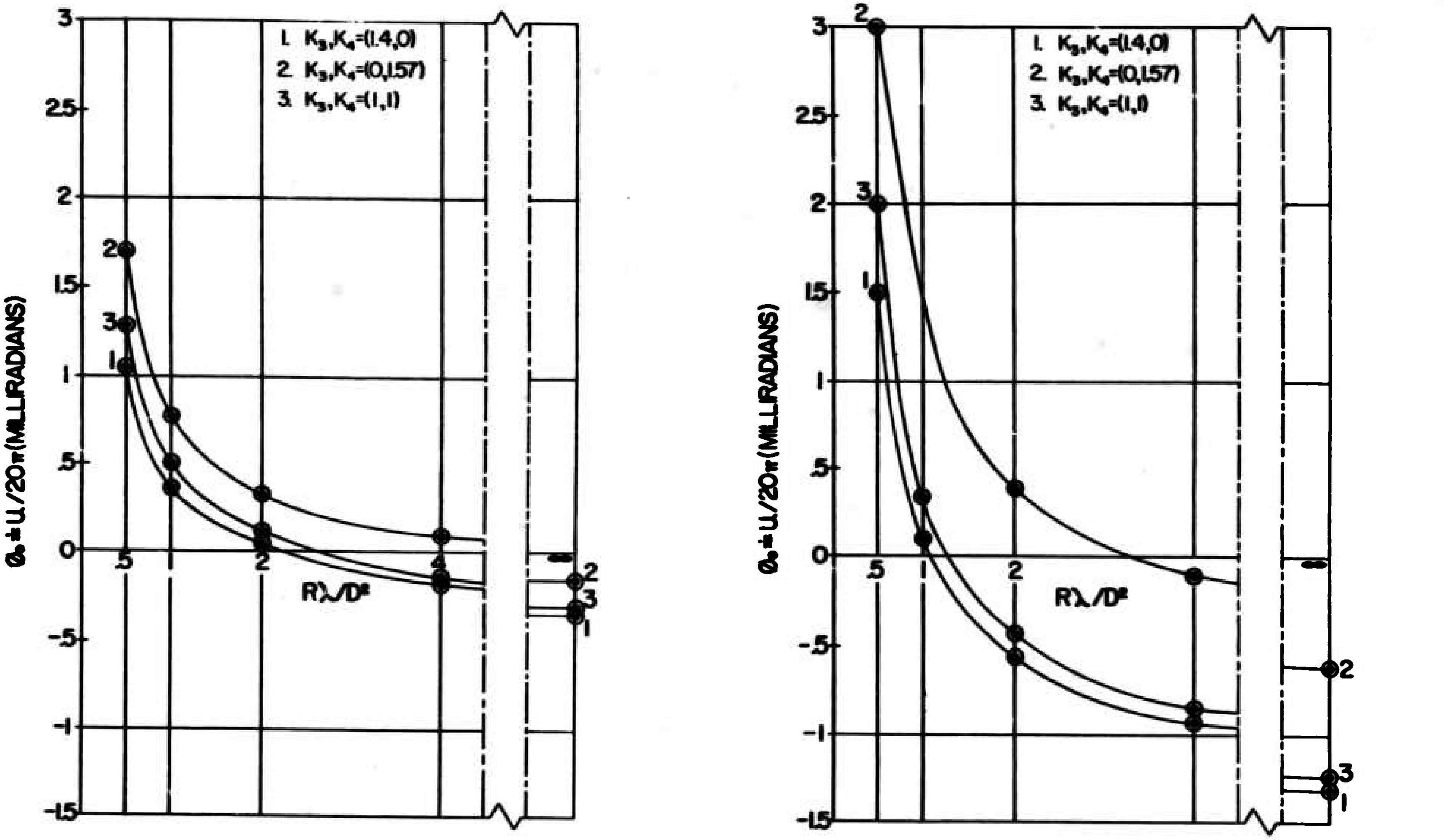

(a) $K_{2L} = 0$, $K_{2R} = 0.5$

(b) $K_{2L} = 0$, $K_{2R} = 1.0$

Figure 58. Calculated Boresight Direction, $K_5 = 0$

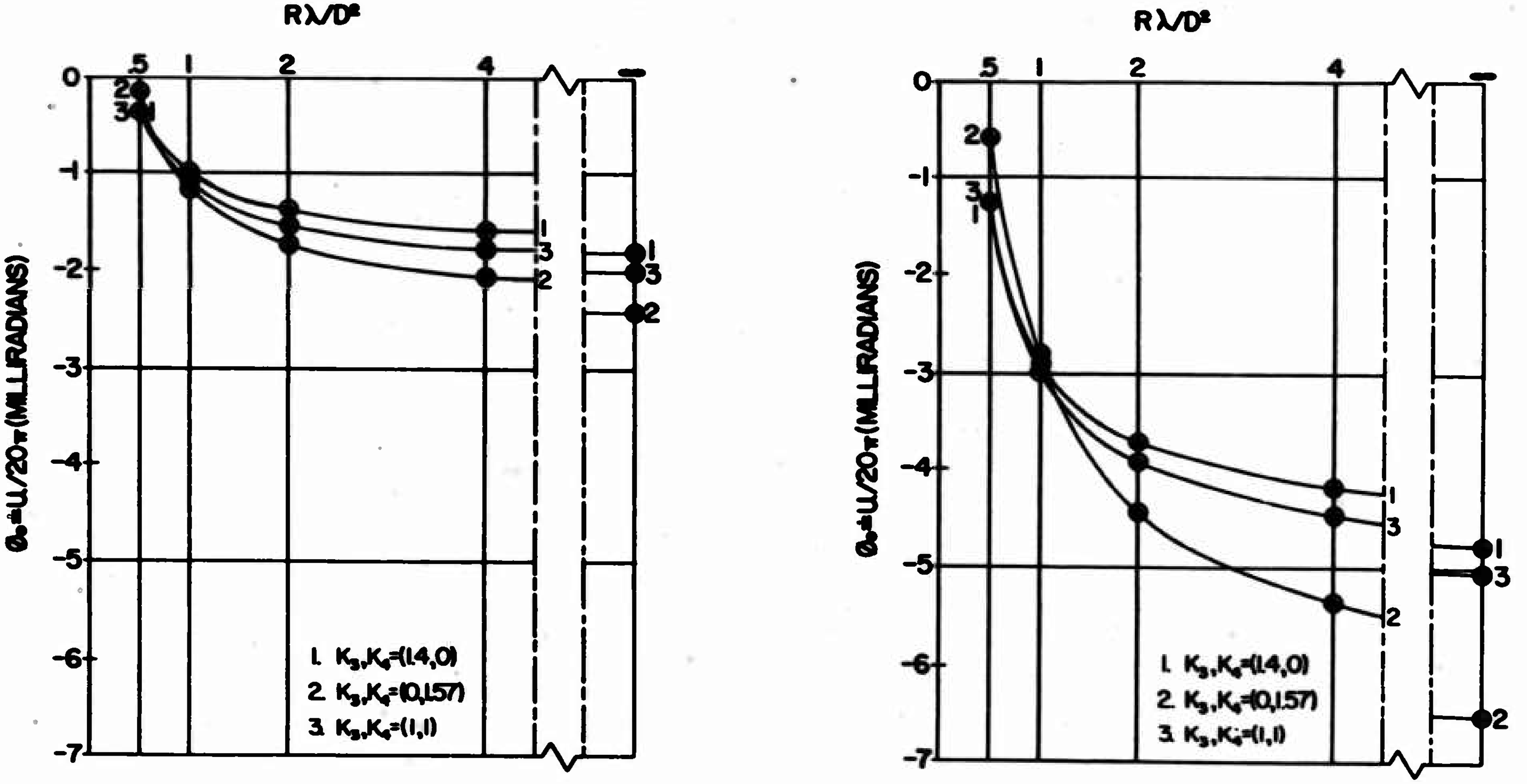

(a) $K_{2L} = 0$, $K_{2R} = 0.5$

(b) $K_{2L} = 0$, $K_{2R} = 1.0$

Figure 59. Calculated Boresight Direction, $K_5 = \pi/2$

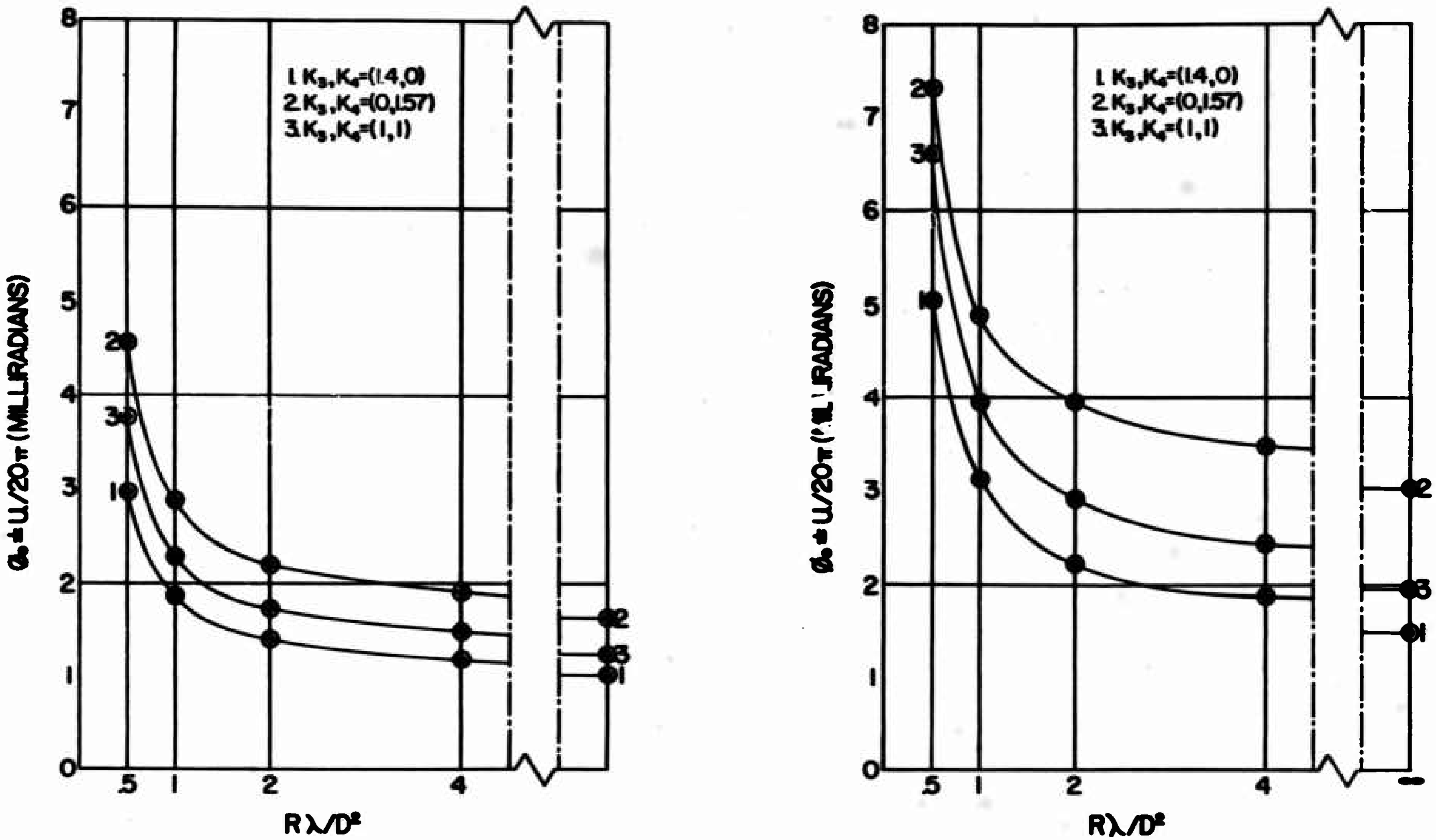

(a) $K_{2L} = 0$, $K_{2R} = 0.5$

(b) $K_{2L} = 0$, $K_{2R} = 1.0$

Figure 60. Calculated Boresight Direction, $K_5 = -\pi/2$

6. CONCLUSIONS AND RECOMMENDATIONS

6.1 Three-Dimensional Antenna Pattern Recorder and Display System

Experiments were conducted to determine the feasibility and evaluate the major design problems of the high-speed radiation distribution recorder proposed under the study program of Phase I. These experiments verified that the proposed recording system is feasible, and that recording rates in excess of 100 data points per second are practical. Experience with a breadboard model and further studies of methods of implementing the recorder have revealed areas in which improvements can be made to the basic recording method proposed. A description of a proposed format and recording techniques is given in Section 2.4. It is recommended that a program be undertaken to develop an experimental model of the proposed high-speed radiation distribution recorder. Furthermore, it is recommended that a further study of high-speed antenna-pattern recording techniques and magnetic-tape systems be conducted concurrently in order to define in detail additional equipment required to meet the goals of the RADC high-speed, precision antenna measurement program.

6.2 Investigation of Environmental Effects on Accuracy of Antenna Measurements

A study of the USAF Antenna Proving Range at Newport, New York, has been made to determine the effects of antenna test range environment on measurement accuracy. The object of the investigation was to evaluate the possible errors which might result from environmental factors on the new range (identified as transmission path #2 in Figure 22) and to recommend techniques which might minimize these errors.

Preliminary investigation indicated that the most serious source of environmental error would be extraneous signals caused by reflections from the range surface. The problem of reflections from arbitrary surfaces was investigated, and the general theory is included in Section 3.2. The theory is applied to the specific case of transmission path #2 at the RADC Antenna Proving Range in Section 3.4.

It is concluded that at very high frequencies (of the order of 10 Gc) errors due to reflected energy should be low for narrow-beam antennas, if proper measurement procedures are observed. On the other hand, the extraneous signal due t reflections can be quite severe at low frequencies; the analysis of Section 3.3 indicates that large errors in sidelobe measurement can result at these frequencies from reflections.

The problem of reflections from rough surfaces is far from being solved exactly. Any useful solution, including the one discussed in Section 3.2, is based on approximations which, to a greater or lesser degree, impair the accuracy of the results. The analysis presented in this report yields results which are in agreement with experimental data which have been recorded in the literature. In order to more accurately determine the effects of reflections on measurement accuracy, it is recommended that a program of experimental measurement of the reflected energy be conducted for the Newport range. Such a program would be directed toward determining the extent of extraneous reflections and the corresponding effect on measurement accuracies over the frequency region of 200 Mc to 10 Gc. A study of this type would supplement the analysis presented in this report and evaluate the measurement capability of the RADC Antenna Proving Range.

6.3 Antenna Positioning

The spherical coordinate system is employed for virtually all antenna pattern measurements since the radiation pattern of an antenna is defined in terms of the field over a sphere which is centered on the antenna under test. This coordinate system may be oriented with respect to the antenna in any manner that is most convenient to the antenna under consideration; the particular orientation usually is determined by the requirements of the using system.

To permit making antenna measurements as functions of ϕ and θ in a spherical coordinate system, it is necessary for the antenna positioner to have two axes of rotation which are orthogonal. Two positioner configurations, commonly referred to as azimuth-over-elevation and elevation-over-azimuth, are employed for this purpose. Both accomplish the same function but differ in the physical orientation of the coordinate system and in the practical limits of rotation in ϕ and θ. In addition to the two axes of the basic configurations, one or more axes are often employed to provide versatility in making antenna measurements. A convenient four-axis positioner arrangement consists of an azimuth-over-elevation positioner mounted over a second azimuth axis, with the complete positioner mounted on a "tilt-axis" which has a travel of a few degrees.

When the four-axis positioner described above is operated in a conventional azimuth-over-elevation configuration, an improved capability is provided by an additional motor driven axis attached to the upper-azimuth turntable. The extra axis, which is normal to the upper-azimuth axis, provides a means for rotating the test antenna 180 degrees about its axis. This permits exploration of the sidelobe region which is normally above the beam axis without the necessity of directing the beam maximum toward the range surface.

It is recommended that the heavy-duty three-axis positioner which will be installed at the Newport antenna range in early 1966 be modified to provide a tilt-axis and an additional removable axis above the upper-azimuth turntable.

When a high order of angular accuracy is to be attained, careful attention to the coordinate system and positioning system is required. Excessive errors can be introduced in the measurements if the coordinate system of the antenna is not properly aligned with the coordinate system of the antenna range. Additional errors are caused by misalignment of the mechanical axes of the positioning equipment. The equations developed in Section 4.4 can be utilized to determine the antenna positioning errors caused by (1) coordinate axis misalignment, (2) orthogonality error, and (3) collimation error.

Remote indicating electronic levels are recommended for improving the angle measurement accuracy of the positioner installation at the Newport antenna range. Overall performance of the system will also be considerably improved if solar radiation shielding is employed.

At the presently available maximum positioner speed of 0.6 degree per second, the proposed high-speed radiation distribution recorder would not be utilized at its maximum capability. It is recommended that the drive system of both the upper-azimuth and the lower-azimuth turntables of the three-axis positioner be modified to permit higher rotation rates.

6.4 Investigation of Parallax in Testing Asymmetrical Antennas

Studies of the effects of parallax in testing asymmetrical antennas were conducted utilizing digital-computer calculations for assumed degrees of asymmetry. The calculations indicate that while centers-of-parallax and centers-of-phase, as defined in Section 5 of this report, are not generally coincident, they lie on the same side of the antenna axis for all asymmetrical cases tested. For relatively extreme aperture distributions, the deviation of either the center-of-parallax or the center-of-phase from the geometrical center of the aperture was found to be less than approximately 0.2 times the radius of the aperture. Parallax corrections are usually applied on an original assumption that the center-of-parallax and center-of-phase are coincident at the center of the aperture. Using the 0.2 radius figure above, it can be shown that the error in the parallax correction which is applied in determining the direction of the beam maximum of an asymmetrical antenna tested at a range of KD^2/λ will be no greater than about 1/10K times the half-power beamwidth of the antenna under test, but may be of this order. Thus, for tests conducted at ranges greater than $2D^2/\lambda$, the resulting error should be no greater than 1/20 times the half-power beamwidth, but may approach this value.

Error in antenna boresight measurements due to asymmetry of the source antenna can be seen from the following example. Consider the case where the center-of-phase of an asymmetrical antenna is assumed to lie at the geometrical center of the aperture, while the actual location is approximately 0.1 times the radius from its center. If this antenna is employed as a source antenna in a boresight measurement application, the corresponding error component ϵ in the measured boresight direction will be approximately 0.05 times the ratio d/R, where d is diameter of the source antenna and R is the test separation. In terms of the diameter D of the antenna under test, $\epsilon = 0.05KD/R$, where $K = d/D$. At a separation $R = 2D^2/\lambda$ the resulting boresight error would be of the order of 1.5 percent of the half-power beamwidth of the antenna under test for $K = 0.8$, a typical value which provides an illumination taper of about 1/4 decibel over the test aperture. While a deviation of 0.1 times the radius is likely to be extreme, boresight measurement errors of 1.5 percent of the half-power beamwidth of the antenna under test cannot be tolerated in many problems. Thus the axial symmetry of the source antenna can be of concern in measuring the boresight directions of precision antennas. On the other hand, if the source antenna is designed to be symmetrical and is fabricated so that it is in fact essentially symmetrical, the center of phase is likely to be very close to the axis of the antenna. If the measurements are made at a separation, $R \geq 2D^2/\lambda$, with amplitude taper over the test aperture not exceeding 1/4 decibel, the resulting deviation should represent an error which can be neglected except in problems requiring precision of the highest order in boresight measurements.

The effect of parallax in testing asymmetrical amplitude-monopulse antennas was investigated. Calculations indicate that for the assumed degree of asymmetries employed, boresight errors result which may be non-negligible especially in tests of asymmetrical antennas at separations of $R \leq D^2/\lambda$. For theoretically symmetrical antennas the measured boresight is independent of range within the Fresnel and Fraunhofer regions. For practical cases of antennas which are designed to be and are fabricated essentially symmetrical, the boresight error caused by parallax resulting from residual asymmetry of the antenna is likely to be negligible, except in cases requiring extreme precision, if the measurements are made at separations, $R \geq 2D^2/\lambda$.

APPENDIX A
SPHERICAL COORDINATE TRANSFORMATION BY EULER ANGLES

The relative orientation of two three-dimensional, orthogonal coordinate systems can be described by the three Euler angles α, β and γ. In the general case any relative orientation of the two coordinate systems can be achieved by three successive rotations about the coordinate axes. The rotations from a coordinate system $\bar{X}\bar{Y}\bar{Z}$ to a system XYZ are (Figure 61):

1. Rotation about the $\bar{Z}$-axis through an angle α to X"Y"Z".
2. Rotation about the Y"-axis through an angle β to X'Y'Z'.
3. Rotation about the Z'-axis through an angle γ to XYZ.

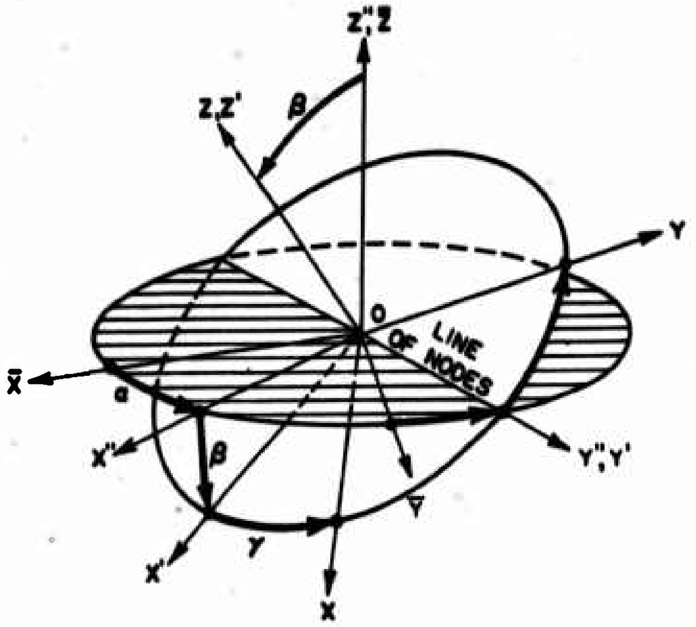

Figure 61. Coordinate Axes Rotated Through the Euler Angles α, β, γ

Let the spherical coordinates ϕ, θ designate a direction OP in the coordinate system XYZ of Figure 62, and let the spherical coordinates $\bar{\phi}, \bar{\theta}$ designate the direction OP in the coordinate system $\bar{X}\bar{Y}\bar{Z}$. The direction ϕ, θ may then be described in terms of $\bar{\phi}, \bar{\theta}$ and the Euler angles α, β and γ.

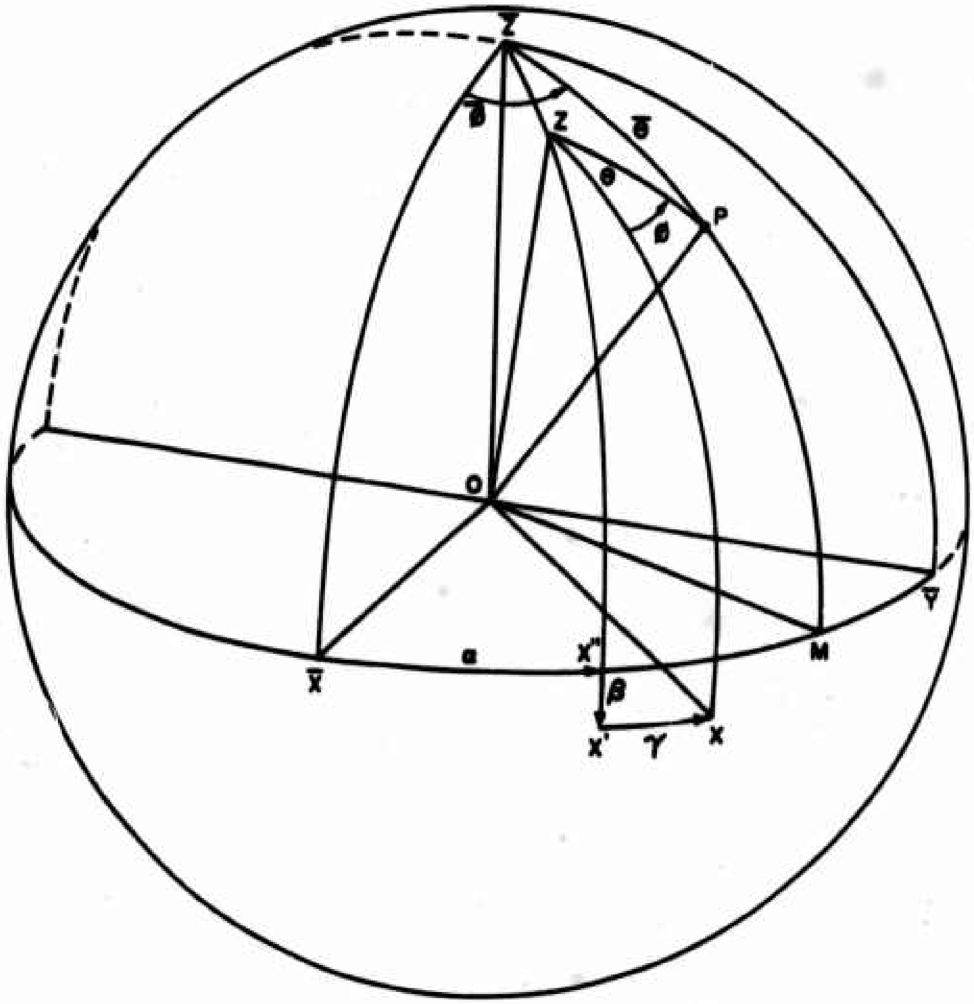

Figure 62. A Direction Described in Two Coordinate Systems

Figure 63 shows the spherical triangles which are used in the solution of

$$\phi, \theta = f(\bar{\phi}, \bar{\theta}, \alpha, \beta, \gamma) .$$

From the spherical triangle $Z\bar{Z}P$ and the law of cosines,

$$\cos\theta = \cos\bar{\theta}\cos\beta + \sin\bar{\theta}\sin\beta\cos(\bar{\phi} - \alpha) , \tag{93}$$

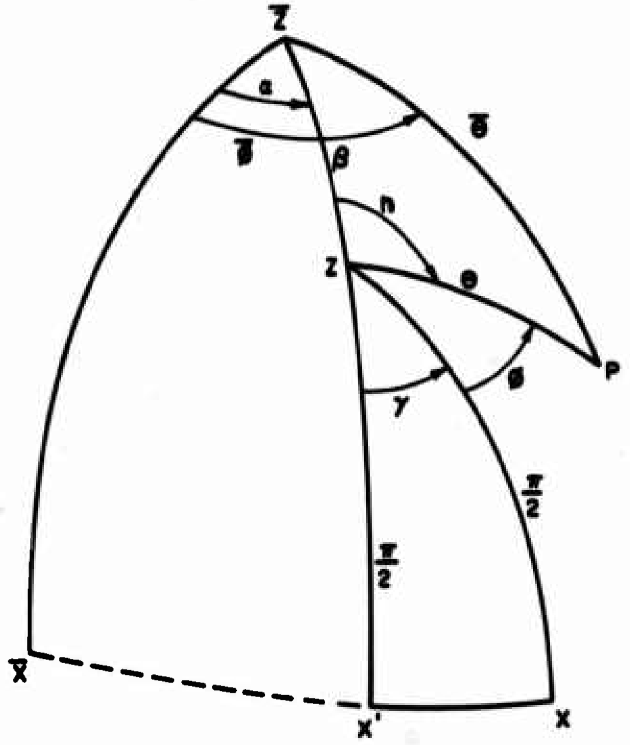

Figure 63. Spherical Triangles From Figure 62

or

$$\theta = \cos^{-1}[\cos\bar{\theta}\cos\beta + \sin\bar{\theta}\sin\beta\cos(\bar{\phi}-\alpha)] . \tag{94}$$

And also by the law of cosines

$$\cos\bar{\theta} = \cos\theta\cos\beta + \sin\theta\sin\beta\cos n \quad . \tag{95}$$

It can be seen that

$$n = \pi - (\phi+\gamma) \quad ,$$

and

$$\cos n = \cos[\pi - (\phi+\gamma)] \quad ,$$

or

$$\cos n = -\cos(\phi+\gamma) \quad , \tag{96}$$

and

$$\sin n = \sin(\phi+\gamma) \quad . \tag{97}$$

Equation (96) may be substituted into (95) to give

$$\cos\bar{\theta} = \cos\theta\cos\beta - \sin\theta\sin\beta\cos(\phi+\gamma) \quad ,$$

or

$$\sin\theta \cos(\phi + \gamma) = \frac{\cos\theta \cos\beta - \cos\bar{\theta}}{\sin\beta} \quad . \tag{98}$$

From the spherical triangle $Z\bar{Z}P$ and the law of sines,

$$\frac{\sin(\bar{\phi} - \alpha)}{\sin\theta} = \frac{\sin n}{\sin\bar{\theta}} \quad .$$

Substituting from (97) and rearranging gives

$$\sin\theta \sin(\phi + \gamma) = \sin\bar{\theta} \sin(\bar{\phi} - \alpha) \quad . \tag{99}$$

Dividing (99) by (98) gives

$$\tan(\phi + \gamma) = \frac{\sin\bar{\theta} \sin\beta \sin(\bar{\phi} - \alpha)}{\cos\theta \cos\beta - \cos\bar{\theta}} \quad . \tag{100}$$

Substituting (93) into (100) and rearranging gives

$$\phi = \tan^{-1}\left[\frac{\sin\bar{\theta} \sin\beta \sin(\bar{\phi} - \alpha)}{\cos\beta\,[\cos\bar{\theta} \cos\beta + \sin\bar{\theta} \sin\beta \cos(\bar{\phi} - \alpha)] - \cos\bar{\theta}}\right] - \gamma \quad ,$$

which may be simplified to

$$\phi = \tan^{-1}\left[\frac{\sin\bar{\theta} \sin(\bar{\phi} - \alpha)}{\sin\bar{\theta} \cos\beta \cos(\bar{\phi} - \alpha) - \cos\bar{\theta} \sin\beta}\right] - \gamma \quad . \tag{101}$$

APPENDIX B
PARALLAX EQUATIONS

With reference to Figure 43, the general expression for the magnitude of the radius vector in a Cartesian coordinate system is

$$r_i^2 = x_i^2 + y_i^2 + z_i^2 \quad . \tag{102}$$

Translation from a system whose origin is (x=0, y=0, z=0) to a system whose origin is at the point (x_o, y_o, z_o) defines

$$r_o^2 = x_o^2 + y_o^2 + z_o^2 \quad . \tag{103}$$

If the point defined by (103) is to be the origin of a primed coordinate system (x', y', z'), then

$$\begin{aligned} x' &= x - x_o \\ y' &= y - y_o \\ z' &= z - z_o \quad . \end{aligned} \tag{104}$$

The general transformation equations for the changes of variable in going from Cartesian to spherical coordinate systems are (see Figure 43)

$$x_i = r_i \sin\theta_i \operatorname{cor} \phi_i \tag{105a}$$

$$y_i = r_i \sin\theta_i \sin\phi_i \tag{105b}$$

$$z_i = r_i \cos\theta_i \quad . \tag{105c}$$

From (105a) and (105b), we have $r_i^2 \sin^2\theta_i = x_i^2 + y_i^2$, and from (105c), $\cos\theta_i = z_i/r_i$. The transcendental equations for θ' are seen to be

$$\sin\theta' = \frac{1}{r'}\left[(r \sin\theta \cos\phi - r_o \sin\theta_o \cos\phi_o)^2 + (r \sin\theta \sin\phi - r_o \sin\theta_o \sin\phi_o)^2\right]^{\frac{1}{2}} \tag{106}$$

and

$$\cos\theta' = \frac{(r \cos\theta - r_o \cos\theta_o)}{r'} \tag{107}$$

where

$$r' = [(r \sin\theta \cos\phi - r_o \sin\theta_o \cos\phi_o)^2 + (r \sin\theta \sin\phi - r_o \sin\theta_o \sin\phi_o)^2 + (r \cos\theta - r_o \cos\theta_o)^2]^{\frac{1}{2}} \tag{108}$$

Using (106) in (105b) gives

$$\sin\phi' = \frac{(r \sin\theta_o \sin\phi - r_o \sin\theta_o \sin\phi_o)}{[(r \sin\theta \cos\phi - r_o \sin\theta_o \cos\phi_o)^2 + (r \sin\theta \sin\phi - r_o \sin\theta_o \sin\phi_o)^2]^{\frac{1}{2}}} \tag{109}$$

Using (107) in (105a) gives

$$\cos\phi' = \frac{(r \sin\theta \cos\phi - r_o \sin\theta_o \cos\phi_o)}{[(r \sin\theta \cos\phi - r_o \sin\theta_o \cos\phi_o)^2 + (r \sin\theta \sin\phi - r_o \sin\theta_o \sin\phi_o)^2]^{\frac{1}{2}}} \tag{110}$$

Equations (106) and (107) yield

$$\theta' = \cot^{-1} \left\{ \frac{[r \cos\theta - r_o \cos\theta_o]^2}{[r \sin\theta \cos\phi - r_o \sin\theta_o \cos\phi_o]^2 + [r \sin\theta \sin\phi - r_o \sin\theta_o \sin\phi_o]^2} \right\}^{\frac{1}{2}} \tag{111}$$

and equations (109) and (110) yield

$$\phi' = \cot^{-1} \frac{r \sin\theta \cos\phi - r_o \sin\theta_o \cos\phi_o}{r \sin\theta \sin\phi - r_o \sin\theta_o \sin\phi_o} \tag{112}$$

for the primed angular parameters. The unprimed angular parameters are

$$\theta = \cot^{-1} \left[\frac{z^2}{r^2 - z^2} \right]^{\frac{1}{2}} \tag{113}$$

and

$$\phi = \cot^{-1} \frac{x}{y} \quad . \tag{114}$$

The parallax angles are given by

$$\theta_p = \theta' - \theta \tag{115}$$

and

$$\phi_p = \phi' - \phi \quad . \tag{116}$$

BIBLIOGRAPHY

1. Investigation of Precision Antenna Pattern Recording and Display Techniques, First Quarterly Report, 1 April 1962 to 30 June 1962, RADC-TDR-62-365.

2. Investigation of Precision Antenna Pattern Recording and Display Techniques, Second Quarterly Report, 1 July 1962 to 30 September 1962, RADC-TDR-62-560.

3. Investigation of Precision Antenna Pattern Recording and Display Techniques, Third Quarterly Report, 1 October 1962 to 31 December 1962, RADC-TDR-63-53.

4. Investigation of Precision Antenna Pattern Recording and Display Techniques, Final Report, 1 April 1962 to 29 March 1963, AD 415-912.

5. Precision Antenna Pattern Recording Techniques, Phase II, First Quarterly Report, 1 June 1964 to 28 August 1964, RADC-TDR-64-420.

6. Precision Antenna Pattern Recording Techniques, Phase II, Second Quarterly Report, 31 August 1964 to 6 November 1964, RADC-TR-64-541.

7. Precision Antenna Pattern Recording Techniques, Phase II, Third Quarterly Report, 9 November 1964 to 29 January 1965, RADC-TR-65-85.

8. Baker, B. B., and E. T. Copson, The Mathematic Theory of Huygen's Principle, Oxford University Press, London, 1950.

9. Beckmann, Petr, and Andre Spizzichino, The Scattering of Electro-Magnetic Waves from Rough Surfaces, The MacMillan Company, 1963.

10. Beckmann, Petr, "Shadowing of Random Rough Surfaces," IEEE Transactions on Antennas and Propagation, Volume AP-13, No. 3, May 1965.

11. Clarke, R. H., and G. O. Hendry, "Prediction and Measurement of the Coherent and Incoherent Power Reflected from a Rough Surface," IEEE Transactions on Antennas and Propagation, Volume AP-12, No. 3, May 1964.

12. Clayton, L., and J. S. Hollis, "Antenna Polarization Analysis by Amplitude Measurement of Multiple Components," Microwave Journal, Volume 8, No. 1, January 1965.

13. IRIG Standard Coordinate System and Data Format for Antenna Patterns, Inter-Range Instrumentation Group, IRIG Document No. 102-61, AD 266697, September 1961.

14. Jordan, E. C., Electromagnetic Waves and Radiating Systems, Prentice-Hall, Englewood Cliffs, New Jersey, 1950.

15. Kerr, D. E., Propagation of Short Radio Waves, Radiation Laboratory Series, Volume 13, McGraw-Hill Co., 1951.

16. Loewe, R. T., R. L. Sisson, and P. Horowitz, "Computer Generated Displays," Proc. IRE, January 1961.

17. National Micro News, No. 66, October 1963.

18. Redman, J. H., "Advanced Display Techniques Through the CHARACTRON Shaped Beam Tube," Presented at the First National Symposium of the Society for Information Display, March 14, 1963.

19. A Short Annotated Bibliography on Rapid Processing, The Department of Information Services, Research Laboratories, Eastman Kodak Company, Rochester 4, New York, October 1960.

20. Silver, S., Microwave Antenna Theory and Design, Radiation Laboratory Series, Volume 13, McGraw-Hill Co., 1949.

21. Stratton, J. A., Electromagnetic Theory, McGraw-Hill, 1941.

22. Morita, Tetsu, Determination of Phase Centers and Amplitude Characteristics of Radiating Structures, Tech. Report No. 1, SR 1, Project 898, Stanford Research Inst., Menlo Park, California, Contract DA 04-200-ORD-273, AD 68240; March 1955.

23. Twersky, Victor, "On Scattering and Reflection of Electromagnetic Waves by Rough Surfaces," IRE Transactions on Antennas and Propagation, January 1957.

24. Twersky, Victor, "Signals, Scatterers, and Statistics," IEEE Transactions on Antennas and Propagation, November 1963.

Unclassified
Security Classification

DOCUMENT CONTROL DATA - R&D

(Security classification of title, body of abstract and indexing annotation must be entered when the overall report is classified)

1. ORIGINATING ACTIVITY (Corporate author) Scientific-Atlanta, Inc. Atlanta, Georgia 30324	2a. REPORT SECURITY CLASSIFICATION Unclassified 2b. GROUP

3. REPORT TITLE
INVESTIGATION OF PRECISION ANTENNA PATTERN RECORDING AND DISPLAY TECHNIQUES, PHASE II

4. DESCRIPTIVE NOTES (Type of report and inclusive dates)
Final - Volume I

5. AUTHOR(S) (Last name, first name, initial)
Hollis, J. Searcy; Hutchins, Samuel F.; Lyon, T. J.; Pidgeon, Rezin E. Jr.; Young, C. S.

6. REPORT DATE February 1966	7a. TOTAL NO. OF PAGES 162	7b. NO. OF REFS 24
8a. CONTRACT OR GRANT NO. AF30(602)3425 b. PROJECT NO. 4506 c. Task No. 450604 d.	9a. ORIGINATOR'S REPORT NUMBER(S) 9b. OTHER REPORT NO(S) (Any other numbers that may be assigned this report) RADC-TR-65-534, Vol I	

10. AVAILABILITY/LIMITATION NOTICES
Distribution of this document is unlimited

11. SUPPLEMENTARY NOTES	12. SPONSORING MILITARY ACTIVITY Rome Air Development Center (EMATA) Griffiss AFB, New York 13440

13. ABSTRACT

Volume I of the Final Report of theoretical work accomplished by Scientific-Atlanta, Inc., for Rome Air Development Center under Contract AF30(602)3425 is presented. The contract is for development of equipment to enhance the antenna measurement capability of ground-based antenna test ranges, and for continuation of theoretical studies initiated under Contract AF30(602)2737. The theoretical studies reported herein include an investigation of environmental effects and an analysis of parallex errors as related to high-accuracy antenna measurements; an investigation of antenna-positioning techniques and angle-measuring equipment; and a determination of optimum techniques for a high-speed precision recording system. Volume II will describe an amplitude- and frequency-stabilized signal source for the frequency range of 2 Gc to 4 Gc and a precision, high data rate receiver with logarithmic readout of data in digital and analog form.

DD FORM 1 JAN 64 1473

Unclassified
Security Classification

14. KEY WORDS	LINK A		LINK B		LINK C	
	ROLE	WT	ROLE	WT	ROLE	WT
Measuring Devices (Electrical & Electronic)						
Electronic Recording Systems						
Ranges (Establishments)						

INSTRUCTIONS

1. **ORIGINATING ACTIVITY:** Enter the name and address of the contractor, subcontractor, grantee, Department of Defense activity or other organization *(corporate author)* issuing the report.

2*a*. **REPORT SECURITY CLASSIFICATION:** Enter the overall security classification of the report. Indicate whether "Restricted Data" is included. Marking is to be in accordance with appropriate security regulations.

2*b*. **GROUP:** Automatic downgrading is specified in DoD Directive 5200.10 and Armed Forces Industrial Manual. Enter the group number. Also, when applicable, show that optional markings have been used for Group 3 and Group 4 as authorized.

3. **REPORT TITLE:** Enter the complete report title in all capital letters. Titles in all cases should be unclassified. If a meaningful title cannot be selected without classification, show title classification in all capitals in parenthesis immediately following the title.

4. **DESCRIPTIVE NOTES:** If appropriate, enter the type of report, e.g., interim, progress, summary, annual, or final. Give the inclusive dates when a specific reporting period is covered.

5. **AUTHOR(S):** Enter the name(s) of author(s) as shown on or in the report. Enter last name, first name, middle initial. If military, show rank and branch of service. The name of the principal author is an absolute minimum requirement.

6. **REPORT DATE:** Enter the date of the report as day, month, year; or month, year. If more than one date appears on the report, use date of publication.

7*a*. **TOTAL NUMBER OF PAGES:** The total page count should follow normal pagination procedures, i.e., enter the number of pages containing information.

7*b*. **NUMBER OF REFERENCES:** Enter the total number of references cited in the report.

8*a*. **CONTRACT OR GRANT NUMBER:** If appropriate, enter the applicable number of the contract or grant under which the report was written.

8*b*, 8*c*, & 8*d*. **PROJECT NUMBER:** Enter the appropriate military department identification, such as project number, subproject number, system numbers, task number, etc.

9*a*. **ORIGINATOR'S REPORT NUMBER(S):** Enter the official report number by which the document will be identified and controlled by the originating activity. This number must be unique to this report.

9*b*. **OTHER REPORT NUMBER(S):** If the report has been assigned any other report numbers *(either by the originator or by the sponsor)*, also enter this number(s).

10. **AVAILABILITY/LIMITATION NOTICES:** Enter any limitations on further dissemination of the report, other than those imposed by security classification, using standard statements such as:

(1) "Qualified requesters may obtain copies of this report from DDC."

(2) "Foreign announcement and dissemination of this report by DDC is not authorized."

(3) "U. S. Government agencies may obtain copies of this report directly from DDC. Other qualified DDC users shall request through
____."

(4) "U. S. military agencies may obtain copies of this report directly from DDC. Other qualified users shall request through
____."

(5) "All distribution of this report is controlled. Qualified DDC users shall request through
____."

If the report has been furnished to the Office of Technical Services, Department of Commerce, for sale to the public, indicate this fact and enter the price, if known.

11. **SUPPLEMENTARY NOTES:** Use for additional explanatory notes.

12. **SPONSORING MILITARY ACTIVITY:** Enter the name of the departmental project office or laboratory sponsoring *(paying for)* the research and development. Include address.

13. **ABSTRACT:** Enter an abstract giving a brief and factual summary of the document indicative of the report, even though it may also appear elsewhere in the body of the technical report. If additional space is required, a continuation sheet shall be attached.

It is highly desirable that the abstract of classified reports be unclassified. Each paragraph of the abstract shall end with an indication of the military security classification of the information in the paragraph, represented as *(TS)*, *(S)*, *(C)*, or *(U)*.

There is no limitation on the length of the abstract. However, the suggested length is from 150 to 225 words.

14. **KEY WORDS:** Key words are technically meaningful terms or short phrases that characterize a report and may be used as index entries for cataloging the report. Key words must be selected so that no security classification is required. Identifiers, such as equipment model designation, trade name, military project code name, geographic location, may be used as key words but will be followed by an indication of technical context. The assignment of links, rules, and weights is optional.